A Study of Multi-Speed Discrete-Velocity Gases

Thesis by

Balasubramanya T. Nadiga

In Partial Fulfillment of the Requirements

for the Degree of

Doctor of Philosophy

California Institute of Technology

Pasadena, California

1992

(Defended February 28, 1992)

Acknowledgements

I would like to thank my advisors, Prof. Bradford Sturtevant and Dr. James E. Broadwell, for their advice and constant support. I have learnt a lot about doing research from them. Thanks also for letting me the fullest freedom in shaping the research; it was a very enjoyable experience. Some of Prof. Dale I. Pullin's ideas were instrumental to the latter part of the work. Discussions with Prof. Gerald B. Whitham were always as insightful as enjoyable. My thanks to GALCIT for introducing me into the world of fluid flows, and to Prof. Roddam Narasimha for pointing to me certain interesting areas.

There is no adequate way to thank my parents for all that they have done for me. And I am grateful to the various institutions and people that have contributed to my education.

The CS dept. and the CCSF have been generous in extending their computer resources and technical support towards this project; thanks to them. Special thanks to Dr. Wen King Su for his forthcoming programming tips. Prof. Paul Dimotakis's $\alpha - TEX$ greatly simplified the preparation of this manuscript.

This work was supported in part by the NSF under Cooperative Agreement No. CCR-8809615.

Abstract

The applicability of multi-speed discrete-velocity gases to compressible flow situations is considered. First, the equation of state, the anisotropies and the advection velocities for any multi-speed model on the square and triangular lattices are derived. The dependence on the model of any of these to leading order in the flow velocity is shown to be only through a fourth moment of the stationary equilibrium speed distribution. Next, a computation scheme is introduced, wherein adjacent cells in a cell network interact through an exchange of particles, commensurate with the equilibrium fluxes of mass, momentum, and energy. This corresponds to the infinite collision rate limit of the model gas, resulting in very low viscosities. Finally, a simple multi-speed model, the nine-velocity model is studied in detail: Solving the shock tube flow with the model yields almost all phenomenology associated with a perfect gas. An exact shock profile is computed for the model and is compared to a Navier-Stokes shock profile. An adiabatic channel flow is simulated with the model and the results compared to an integral solution of the Navier-Stokes equation. The comparisons in both the cases are excellent. It is also shown that the nine-velocity gas does not permit steady supersonic flow.

Contents

CHAPTER 1

Introduction

A discrete-velocity model of a fluid was considered as early as 1890 by Maxwell in the context of kinetic theory of gases. Subsequent investigators (Broadwell 1964a, 1964b; Hardy & Pomeau 1972; Hardy *et al.* 1976; Gatignol 1975; *etc.*) have advanced the understanding of these models considerably. The large scale utilization of these models as a simulation strategy for fluids, however, had to await the work of Wolfram (1986), in which the computer-scientific idea of a cellular automaton (CA), Neumann (1949), was unified with the idea of a discrete-velocity gas to give rise to, what has been called, a lattice gas. While this has been the main reason for the recent surge of activity in this area, Doolen (1989, 1991), as with most pioneering works, some of the shortcomings of this methodology have since been recognized (McNamara & Zanetti 1988, Zanetti 1989). From the point of view of fluid dynamics, however, some of the *qualitatively* unphysical assumptions that go into a lattice gas, contribute to making the simulation strategy unsatisfactory and a good simulation technique for discrete-velocity gases would be more desirable. Implementation aspects aside, it is also felt that, in the context of fluid dynamics, other than for a few specialized studies, a lattice gas has little advantage over a discrete-velocity gas, *i.e.*, most of the useful aspects of a lattice gas comes from it being a discrete-velocity gas. Quite apart from the simulation strategies, most work in discrete-velocity gases has dealt with single-speed models. Investigation of the physics of *multi-speed* discrete-velocity gases, with compressible flow situations* in mind, and the developement of a good simulation strategy for discrete-velocity gases is the motivation for the present work.

---

* Compressible dynamics of single-speed models have been studied quite extensively (Broadwell 1964a, 1964b; Gatignol 1975, Caflisch 1979).

1.1 Lattice Gas Techniques

Since the recent revival of activity in the area of discrete models for fluids has been mainly due to the popularization of lattice gas techinques, the idea behind these techniques is briefly considered here. Dynamical systems which are discrete in space and time and whose sites take on only a finite set of values are termed lattice gases because of their close analogy to the kinetic constitution of gases. Consequent to their complete discreteness, they can be very effectively simulated as cellular automata. Further, the high degree of parallelism achieved by limiting interactions to short ranges, renders them ideal for the parallel processing computing architectures that are being evolved. These highly desirable features of lattice gas methods make it very attractive to be able to use them as a simulation strategy for complex physical phenomena. Equivalently, these models can be seen as solution techniques for the partial differential equations describing the phenomenology of the original physical processes, Doolen (1989,1991). Sometimes, the reference to the physical situation is entirely by-passed and one tries to find a lattice gas representation of a particular partial differential equation. This approach, though very attractive, has not met with much success. The more usual procedure consists of isolating the essential physics of the situation involved into a simple lattice gas model, and studying the model. The model itself is then used as a direct simulation strategy or, strange as it may seem, partial differential equations describing approximately the lattice gas model are developed and these are compared and contrasted to the original partial differential equations. Such an exercise has a twofold usefulness:

1. In trying to make the model partial differential equations resemble the original equations, the necessary physics of the original situation will have to be extracted and no more, often leading to large but good simplifications. Once it is ensured that the equations are of the required form, the models can be employed with confidence in a study of the original phenomenon, Frisch *et al.*(1987).

2. It is hoped that with the two sets of partial differential equations now being very

similar, the lattice gas model, with its simplicity may throw more light on understanding why the solutions of the original partial differential equations behave the way they do.

Add to all these, the ease of handling difficult geometries and complicated boundaries in using these models as direct simulation methods, we may have a good tool to probe the workings of some nontrivial phenomena. In the context of fluid flow, the general purpose of this technique is then to determine how much the properties of the microscopic elements of fluids can be simplified while still retaining the characterisitic macroscopic behavior.

1.2 Discrete Models for Fluids

The phenomenon of interest here is fluid flow, and so the discrete models used are based on the dynamics of real gases. The motivation for using this method is the *universality* of the dynamics** of fluids under a wide variety of molecular structure and interactions: the macroscopic behavior of a fluid near equilibrium is expected to be nearly independent of the *details* of the motion of the molecules that constitute it. For example, low Mach number flow of a gas and of a liquid are described by the same equations. The aim of this approach is then, as mentioned above, to maximally simplify the molecular dynamics while retaining the essential physics. This simplification of the molecular dynamics involves a discretization of the phase space, either full or partial. While a discretization of the physical space alone is one of the most common instances of such a partial discretization and gives rise to the familiar Monte Carlo formulations, a discretization of the velocity space of the molecules gives rise to the notion of a discrete-velocity gas. A full discretization of the phase space *i.e.*, both velocity and physical space, gives rise to a lattice gas. Thus, lattice gases, in the context of fluid dynamics, can in some sense be thought of as a subset of discrete-velocity gases. For purposes of describing these models, some aspects are more easily understood in

** The universality class of interest here is the Navier-Stokes like dynamics

terms of lattice gas models, and for other aspects, discrete-velocity gases are adequate: we freely use both models in describing the various features.

At this point, it may be appropriate to point out that if the process being dealt with was a system of partial differential equations rather than molecular dynamics, then a discretization of the independent variables of the system (space, time) alone would give rise to a finite difference scheme. However, a discretization of the dependent variables, if only of a primary set of them, can in some sense be thought of as representing the behavior of discrete-velocity gases.

In all the models considered, once the velocity space has been discretized, the particles are identified with their velocities, *i.e.*, the particles are otherwise indistinguishable. Discretization of both velocity and position in a lattice gas gives rise to the notion of discrete time, the unit of time being that taken by the slowest moving particle to travel the smallest unit of distance in the direction of its velocity. All other particles move an integer number of link lengths in the direction of their velocities in the same time. The evolution of the system is then reduced to a set of discrete move and collide phases. At each instant, each lattice site collects the relevant information from it's nearest neighbors and performs a simple transformation on it. In the move phase, particles hop over to an adjacent lattice site commensurate with their velocities and the particles at every lattice site scatters according to a predefined set of rules in the collide phase. All instances of collisions considered in the present work conserve mass, momentum and energy individually. The above evolution at the microscopic level ensures the conservation of mass, momentum and energy at the macroscopic level. In the case of a discrete-velocity gas, space and time are continuous and so the evolution can be thought of as continuous rather than in discrete time steps. An additional difference between a discrete-velocity gas and the corresponding lattice gas arises from the *exclusion* principle. The *exclusion* principle is that no lattice site may have more than one particle of a particular type. This is adopted in the implementation of lattice gases for no reason other than to keep the computation per time step small.

1.2.1 The Square and Triangular Geometries

In two dimensions, the only regular polygons which can tile the plane are the triangle (or equivalently the hexagon) and the square. These two different geometries give rise to inherently different macroscopic dynamics and therefore have to be separately considered.

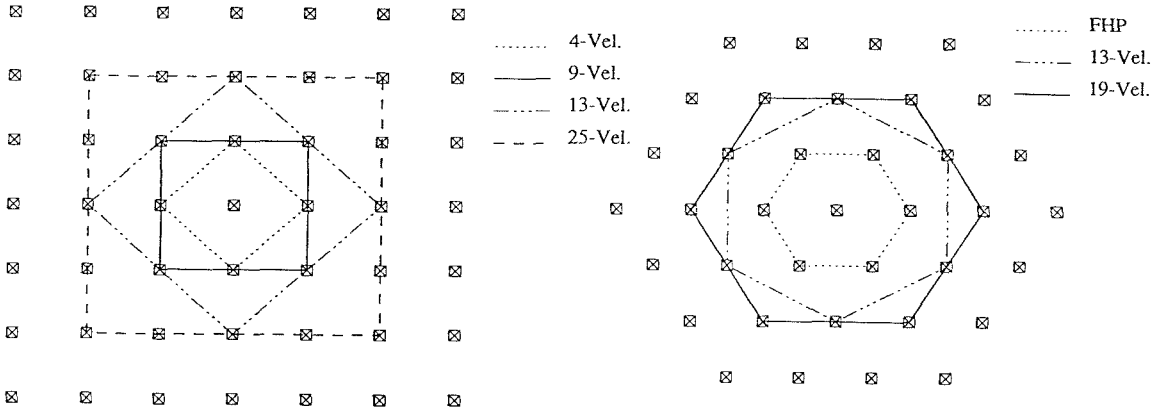

FIG. 1.2.1 Velocity space discretization: square (left) and triangular (right) geometry.

Fig. 1.2.1 shows the discretization of the velocity space with a square and a triangular geometry. The symbols indicate the discretized velocities and the enclosing polygons correspond to the different models.

Fig. 1.2.2 shows a snapshot of a region of space occupied by a lattice gas. The lattice here has a square geometry. The small enclosures are the lattice sites, and the particles, which are identified by their velocities, are indicated by the arrows. The arrows scale with the velocities of the particles, and all of them point to a lattice site. The full set of lattice sites to which the arrows at any lattice site can point to constitute the neighborhood of the lattice site. The simplest model on this lattice is the Hardy-Pomeau-Pazzias (HPP)

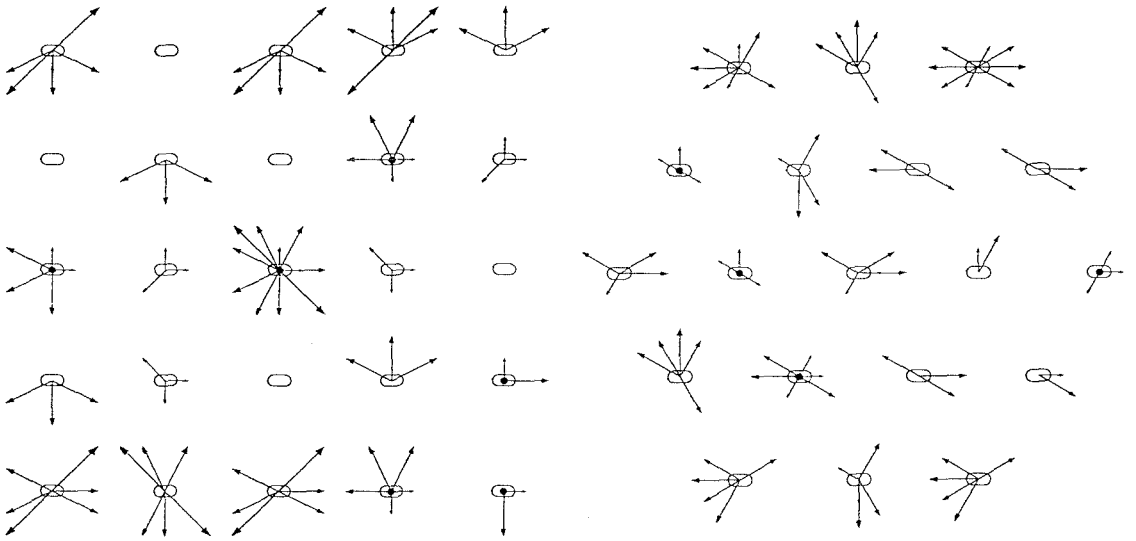

FIG. 1.2.2 Phase space discretization: square (left) and triangular (right) geometry. The small enclosures are the lattice sites and the particles are indicated by arrows, which scale with their velocities. All the arrows point to a lattice site. The full set of lattice sites to which arrows at any lattice site can point to constitute the neighborhood of that lattice site.

model. This model allows only four velocities, directed oppositely along a pair of mutually perpendicular axes; they are all of the same speed. See Fig. 1.2.1. A family of multi-speed models are obtained by considering full square neighborhoods of an increasing size† — the n^{th} multi-speed model has $(2n+1)^2$ allowed velocities and a physical lattice point in the model can affect any of the $(2n+1)^2$ lattice points in its neighborhood. Fig. 1.2.2 also shows the corresponding picture with a triangular geometry. The simplest model on this lattice is the Frisch-Hasslacher-Pomeau (FHP) model with six velocities, all the same speed but directed toward the vertices of a hexagon. A family of multi-speed models are obtained on the triangular lattice by a procedure similar to that on the square lattice.

---

† Models like the different 13-velocity models on the square lattice and the triangular lattices (see Fig. 1.2.1) are not considered to keep the number of models considered small. Moreover, since the geometry of the models which are not considered is the same as the ones which are considered, but with different numbers of velocities, the behavior of the models which are not considered is clear.

Much work has been done in the past few years in trying to recover incompressible fluid dynamic behavior as governed by the Navier-Stokes equations from the above class of lattice gases, Frisch *et al.*(1987). But most such previous lattice gas models consist of particles with a single speed, thus not allowing an independent specification of temperature or energy. Consequently, the exercise of recovering the Navier-Stokes equations is done in the so called incompressible limit. From their constitution, discrete-velocity models are seen to be inherently compressible. Therefore, it is only natural to investigate their applicability to compressible flow situations. A description of compressible flow necessarily requires thermodynamics and so multiple speeds become necessary.

1.2.2 The Nine-Velocity Model

To better illustrate a multi-speed model, the simplest of them with a square geometry, the nine-velocity model (d'Humieres *et al.* 1986; Nadiga *et al.* 1989; Chen *et al.* 1989) is discussed here in more detail.

Fig. 1.2.3 shows the allowable velocities in the nine-velocity model, and the lattice on which the particles move. The slow particles, which have unit speed, say q, are restricted to move on the horizontal and vertical links, whereas the fast particles, which have a speed of $\sqrt{2}q$, move on the diagonal links. The zero speed particles exist only to take part in collisions, to allow interactions between the other two speeds. Each lattice site has nine neighbors, itself, four at a distance δ away and four others at a distance $\sqrt{2}\delta$ away, where δ is the distance traveled by a speed q particle in unit time. After the move phase, all the possible collisions, each conserving mass, momentum and energy, of the types shown in Fig. 1.2.4 take place, subject to the exclusion condition.

Since only one particle of a given velocity is allowable at a site, the site may not be able to accommodate some of the particles resulting from some collisions; hence, those collisions are excluded. The pre-collision velocities are indicated in solid lines, the

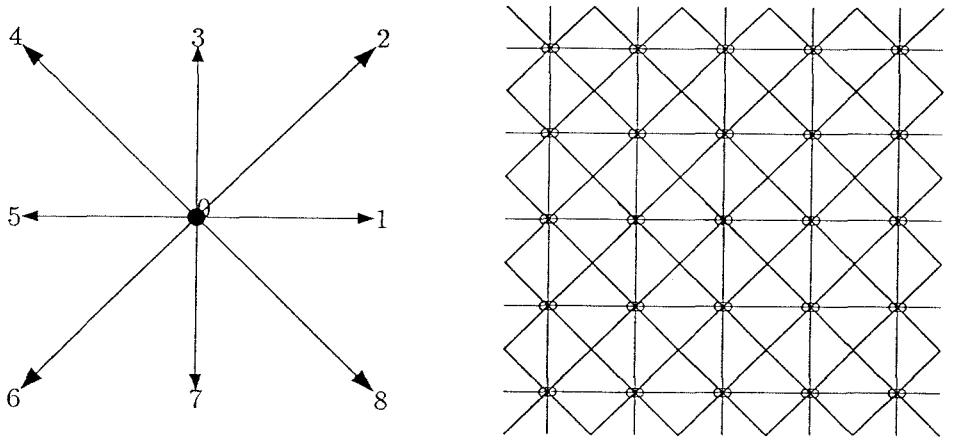

The allowed velocities

The physical lattice

FIG. 1.2.3 The nine velocities allowed in the model comprising three different speeds and the physical lattice on which the particles move.

post-collision velocities in dotted. Collision type 3 is important and unique in that the post-collision speeds are different from the pre-collision speeds. This provides a process of dynamic equilibration between the particles of different speeds. The rest of the collision types involve only an exchange of speeds between the partners.

1.2.3 Implementation

The implementation of a lattice gas on a digital computer is simple, elegant, and highly efficient. In the present work, a lattice site is represented by a computer word. The computational domain is then an array of words. A particle of a particular type (*i.e.*, a particle with a certain velocity) is identified with a particular bit in the word. A word therefore has to have at least as many bits as there are velocities in the model. The presence or absence of a type of particle at a lattice site is indicated by the presence or absence (on or off) of the corresponding bit in the word representing the lattice site. When only a

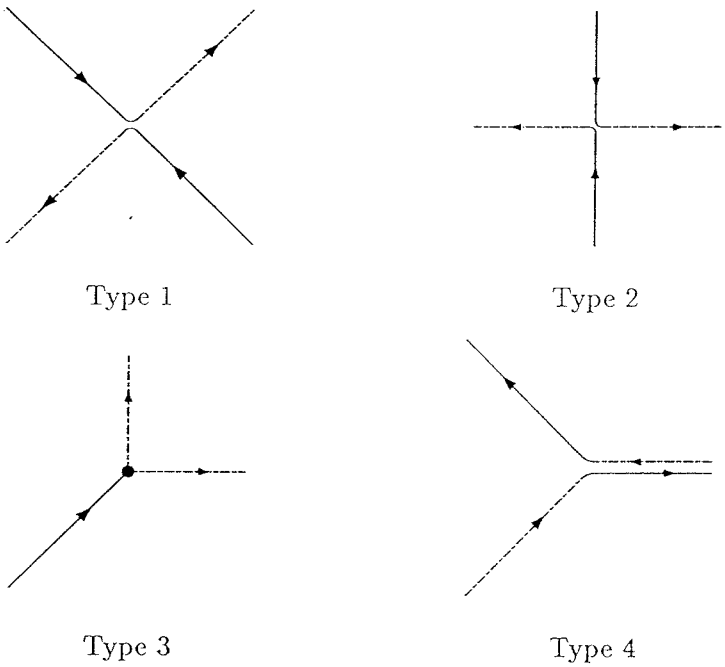

FIG. 1.2.4 The four types of collisions in the nine-velocity model. Only in collision type 3 are the pair of pre-collision speeds different from the pair of post-collision speeds.

few velocities are present in the model (as in FHP, HPP, nine-velocity, *etc*....), the move phase is accomplished by a small number of simple binary operations on the array of words representing the computational domain, while the collide phase is reduced to a table lookup. With more velocities, the move phase requires more binary operations, and the lookup table becomes bulky, necessitating a functional implementation of the collisions. In a variant of the preceding implementation, not used in the present work, the presence or absence of a particle of a particular type at a group of lattice sites is compacted into a word. A set of words, as many as the number of different velocities, then represent several lattice sites, as many as the size of the word. In this scheme, the move phase amounts to shifting words bitwise in the appropriate direction and the collision phase to the evaluation of Boolean functions representing the collisions. In either case, the simplicity of the move and collide steps makes it possible to simulate huge numbers of particles, in comparison to other direct simulation methods. Furthermore, since only nearest neighbors interact, the evolution is

highly localized and hence is ideally suited for parallel computation. The overhead due to communication between the nodes of the parallel processor is proportional to the ratio of the perimeter of the physical space represented by a node to its area, *i.e.*, to the inverse of the aspect ratio of the computational domain. The complete synchrony between the various parts of the computational domain obviate the need for balancing the load between the various processors dynamically.

1.2.4 Macro-Irreversibility of Deterministic Lattice Gases

The completely deterministic nature of the above evolution is exploited in Nadiga *et al.* (1989), where numerical simulations are presented which show that the solutions describing the macroscopic history of the nine-velocity gas is stable in one direction and highly unstable in the reversed direction. This was used as an illustration of the existence of a preferred direction in the evolution of macroscopic systems, *i.e.*, how macroscopic irreversibility comes about in microscopically reversible systems.

1.2.5 The Model Boltzmann Equations

The evolution of the spatial averages of the populations in the model is given by the Boltzmann equations. They are simply a statement of the conservation of the number of particles of each type under the streaming and collision processes. Symbolically, they can be written as

$$L_i n_i = Q_i(n_j, n_j) \qquad i, j = 1, \ldots, b\,, \tag{1.2.1}$$

where $L_i = \partial/\partial t + \mathbf{c_i}.\partial/\partial \mathbf{x}$ is the linear streaming operator of the particle type i, and Q_i is the collision operator of particle type i. As an example, the full equations for the nine-velocity model are shown in Table 1. Implicit in writing these are the assumptions that the gas is dilute and that molecular chaos prevails. The gain and the loss terms that appear on the right-hand sides of the equations for the 10 different collisions are indicated

Model Boltzmann Equations
9 Velocity Gas

c_r	=	$\sqrt{2}q$				$2q$	$2\sqrt{2}q$	$\sqrt{5}q$			
		n_1n_3- n_0n_2	n_3n_5- n_0n_4	n_3n_7- n_0n_6	n_7n_1- n_0n_8	n_3n_7- n_1n_5	n_4n_8- n_2n_6	n_5n_2- n_1n_4	n_5n_8- n_1n_6	n_3n_8- n_7n_2	n_3n_6- n_7n_4
$\frac{\partial n_0}{\partial t}$	=	+	+	+	+						
$\frac{\partial n_1}{\partial t}+q\frac{\partial n_1}{\partial x}$	=	−			−	+		+	+		
$\frac{\partial n_2}{\partial t}+q\frac{\partial n_2}{\partial x}+q\frac{\partial n_2}{\partial y}$	=	+					+	−		+	
$\frac{\partial n_3}{\partial t}+q\frac{\partial n_3}{\partial y}$	=	−	−			−				−	−
$\frac{\partial n_4}{\partial t}-q\frac{\partial n_4}{\partial x}+q\frac{\partial n_4}{\partial y}$	=		+				−	+			+
$\frac{\partial n_5}{\partial t}-q\frac{\partial n_5}{\partial x}$	=		−	−		+		+	+		
$\frac{\partial n_6}{\partial t}-q\frac{\partial n_6}{\partial x}-q\frac{\partial n_6}{\partial y}$	=			+			+		+		−
$\frac{\partial n_7}{\partial t}+q\frac{\partial n_7}{\partial y}$	=			−	−	−				+	+
$\frac{\partial n_8}{\partial t}+q\frac{\partial n_8}{\partial x}-q\frac{\partial n_8}{\partial y}$	=				+		−		−	−	

Table 1

in the second row, and the relative velocity c_r for each of the collision is indicated in the first row. The left-hand sides of each of the nine equations for the nine classes of particles are indicated in the first column. The entries in the matrix give the sign with which the gain/loss terms appear in the corresponding equation. These equations are exact in fact for the dilute discrete-velocity gas limit rather than the lattice gas limit. To the extent of representing the discrete processes in a lattice gas continuously, the error involved in using these equations to represent lattice gas evolution is that these equations do not reflect the effects of the *exclusion* principle. The justification however in using them to describe the lattice gas evolution is that the effects of *exclusion* are negligible in the dilute gas limit, only in which limit these equations are of any validity.

1.3 A Clarification about the terminology

Since the present study concerns with the application of discrete-velocity models only to fluid flows, no special care is taken to distinguish lattice gases from discrete-velocity gases. The justification for this is

- Lattice gases are a subset of discrete-velocity gases, in that the velocities of particles in a lattice gas are discrete. The primary effect on the hydrodynamics of these models is due to the velocity discretization and occupies most of our attention in the course of this thesis. The effects of a *discretization of space*, as reflected by the *exclusion* principle and conservation of *staggered momenta* are secondary and are not studied here.
- At low densities, the behavior of a lattice gas is the same as that of a discrete-velocity gas. This follows from, as seen in the next chapter, the reduction of the equilibrium Fermi-Dirac velocity distribution of lattice gases to the Boltzmann velocity distribution of discrete-velocity gases at low densities.

1.4 Outline

The organization of this thesis is as follows: While chapters 2, 3, and 4 deal with equilibrium situations, chapters 5 and 6 deal with non-equilibrium. In chapter 2, an attempt is made to present a comprehensive picture of the various effects of discretization of the velocity space in a gas of hard sphere particles at equilibrium. The effects of discretization of the physical space on the velocity distribution, is mainly through the exclusion principle of lattice gas automata (Wolfram 1986; Frisch *et al.* 1987). A simple transformation of variables in the equilibrium equation of discrete-velocity gases, discussed in Sec. 2.2, is all that is required to capture these effects. The effects themselves are not considered in any detail; the justification being that the exclusion principle has little physical basis to it: It is used mainly for its computational advantages. By combining analytical and computational tools, the velocity distribution functions are studied to arrive at a few results which throw light on some of the interesting, perhaps bothersome, aspects of these models. The most important of these results is the equation of state for any model with a square or triangular geometry. In this context, some comments are made about the interpretation of pressure in lattice gases. It is also shown that the deviation of the equilibrium distributions of discrete-velocity gases from the Maxwell-Boltzmann distribution can be identified as due to two different causes, one arising out of the finiteness of the velocity unit called the *discretization error* and the other due to finiteness of the velocity space, called the *truncation error.*

In chapter 3, a new paradigm of lattice gas computation is introduced. This is based on Equilibrium Flux Method of Pullin (1980) and enables an elegant and efficient computation of *nearly* inviscid and non-heat conducting lattice gas flows. The elegance of the method comes out of a clear physical interpretation of each of the steps involved. The method is first developed as a simple first order scheme. It is then refined into a second order scheme using a popular limiting strategy, the *min-mod* limiter (Yee 1989). From the point of view of partial differential equations, this new method computes the solutions of the Euler equations of a lattice gas. In this frame work, some of the adjectives that may be

used to describe the scheme include flux-splitting, high order Total Variation Diminishing, shock-capturing, *etc.* While this new paradigm of lattice gas computation retains all the features which make lattice gases interesting and easy to use, it is shown how some of the shortcomings of the presently used methods are circumvented.

In chapter 4, the Euler equations of lattice gas models are developed formally by linking the equilibrium distributions studied in chapter 2 to a flow situation. The equations are then studied in some detail for the nine-velocity model. The study includes looking at the characteristics and other important one-dimensional unsteady phenomena. The latter is mostly done *via* the paradigm introduced in chapter 3. It should be pointed out that the nature of this study is more to understand lattice gases in their own right rather than investigate quantitative concurrence or deviations thereof from perfect gas results.

In chapter 5, the exact structure of a shock in the nine-velocity gas is obtained numerically. The approach here is on the lines of Gilbarg & Paolucci (1953), more dynamical than fluid mechanical in nature. Most phenomena observed in the context of a monatomic gas are seen in this structure: A comparison to the structure as obtained by a solution of the Navier-Stokes equations reveals the similarity. A comparison is then made between the exact shock profiles and those obtained using the method of computation introduced in chapter 3. It is found that the error[‡] in the computation is physically in the right direction. It is conjectured that that method of computation approximates the solutions of the (model) Euler equations as a regular low viscosity limit of the (model) Navier-Stokes solutions.

In chapter 6, the two dimensional, adiabatic, compressible, viscous channel flow is investigated. First, the flow is simulated using the nine-velocity model in a lattice gas automata computation. The simulation being computationally intensive, is carried out on a message-passing multi-computer, the Intel iPSC/860 GAMMA. In the second part, the integral solution method of Broadwell (1952), is developed on exactly the same lines

---

‡ In the sense of deviation from the exact solutions of the model Euler equations.

here, only the resulting nonlinear ordinary differential equations are numerically solved[♯]. Important features of the flow are discussed thereafter and some qualitative comparisons of the two methods are made. The flow field in the vicinity of the sonic region in such an adiabatic flow is expected to be of considerable interest, and has not been previously investigated. Both the methods presently used, however, are seen to be insufficient in correctly modeling the flow in this regime. Using a model with more number of speeds may help study the flow in the vicinity of the sonic region better, but a conclusive study of the problem would require either a full computation of the compressible Navier-Stokes equation or a simulation of the problem using the Monte-Carlo technique.

♯ The ordinary differential equations were not solved originally because of scarce computer resources.

CHAPTER 2

A Study of Equilibrium in Discrete Fluids

In this chapter, an attempt is made to present a comprehensive picture of the various effects of discretization of the velocity space in a gas of hard sphere particles at equilibrium. The effects of exclusion, which become relevant for a lattice gas in view of the discretization of space, are captured by a transformation of variables indicated in Sec. 2.2; for brevity, results are presented only for cases with no spatial discretization. The effects of conservation of staggered momenta (Zanetti 1989), which are again a consequence of the discretization of the physical space in lattice gases, are not considered either, since

1. these conserved quantities in most multi-speed models are expected to be associated with some sort of very detailed encryption procedure*.

2. these conservations are effectively removed by the presence of walls and/or any sort of external interactions.

The effects of a change in the number of speeds allowed on the two different geometries, the square and the triangle are also studied.

---

* In the simplest of the multi-speed models, the nine-velocity model, the staggered momenta are easily identified to be $(-1)^t(G_{xe} - G_{xo})$ and $(-1)^t(G_{ye} - G_{yo})$, where G_{xe} denotes the summation of $g_x(j)$, the x-component of the momentum of a column, j, of physical lattice sites, the summation being carried over all the even numbered columns, j: $G_{xe}(t) = \sum_{j \text{ even}} g_x(j,t)$, G_{yo} denotes the summation of $g_y(i)$, the y-component of the momentum of a row, i, of physical lattice sites, the summation being carried over all the odd numbered rows: $G_{yo}(t) = \sum_{i \text{ odd}} g_y(i,t)$, *etc...* . This is because of the fact that the even though the nine-velocity model is a multi-speed model, the influence of any lattice site in the two coordinate directions is restricted to the nearest one in that direction. See Fig.1.2.3. Thus for example, the x-momentum of a column j of sites at the present instant, no matter what, will be distributed between columns $j-1$ and $j+1$ the next time step. This holds for all j, and if j is even, $j-1$ and $j+1$ are odd and *vice versa*(d'Humieres 1989).

Discretization of the velocity space of the particles constituting a fluid, even though done at the microscopic level, manifests itself in the macroscopic behavior of the fluid. This is best described by the lack of certain symmetries of the partial differential equations describing the macroscopic behavior. Thus while the form of the Navier-Stokes and Euler equations are left unchanged under rotations or Galilean transformations of the reference frame, such rotational invariance or Galilean invariance of the partial differential equations describing the macroscopic dynamics of discrete-velocity gases is not always guaranteed (Hardy *et al.*1976, Wolfram 1986, Frisch *et al.*1987, *etc.*). Most of these symmetries, or lack thereof, are reflected in the equilibrium distributions of these models, and thus the equilibrium studies in this chapter also help understand these features of discrete-velocity gases. A lack of fundamental invariances, as under Galilean transformations and rotational transformations, of the partial differential equations governing the macroscopic phenomena, may make the usage of these models highly suspect. While these concerns are valid, studies of discrete-velocity models, as in this chapter, show that there are regimes in a given model, where the symmetries are restored to a large extent. It is in these regimes that the models are to be operated, if they are to be used in studying physical phenomena.

While it has been known that three body collisions are necessary for thermodynamic equilibrium in the FHP model, there has been no systematic way of telling what collisions — whether binary, ternary or higher order and which of these — are necessary in any given model to reach thermodynamic equilibrium. A simple procedure** to do this is given in Sec. 2.2. Some new results, which help in choosing a velocity discretization for a given problem are presented in Sec. 2.3. While the idea of four tensors of the model characterizing its directional behavior is well known, most such usages, to the authors knowledge, are embedded in thick notation and extraneous details†. The aim in Sec. 2.4, therefore, is comprehensibility and accessibility of these concepts to the non-physicist and minimality of

** The resulting algebra is best handled by a symbolic manipulator.

† An exception is Wolfram 1986.

the situation considered. Notwithstanding that, the expressions for the equations of state for any model on the square and triangular lattices arrived at there is new.

2.1 Definition of Some Macroscopic Properties

Since a discrete-velocity gas has only a finite number of velocities, say b, the velocity distribution function is a summation of delta functions at the allowed velocities.

$$f_d(\mathbf{c}) = \sum_{i=1}^{b} F_d(\mathbf{c})\delta(\mathbf{c} - \mathbf{c}_i)\,. \tag{2.1.1}$$

The ratio of the probabilities of occurance of allowed velocities $\mathbf{c}_i$ and $\mathbf{c}_j$ is $F_d(\mathbf{c}_i)/F_d(\mathbf{c}_j)$. The fact that a particle has to have one of the allowed velocities is expressed by the condition

$$\int_{-\infty}^{\infty} f_d(\mathbf{c})d\mathbf{c} = 1 \Rightarrow \sum_i F_d(\mathbf{c}_i) = 1\,, \tag{2.1.2}$$

where the integration is over the number of velocity dimensions considered. The *average* number of particles with velocity $\mathbf{c}_i$ at the given point in physical space, denoted by n_i is given by $n_i = nF_d(\mathbf{c}_i)$, where n is the number density of particles at that point.

1. Density, ρ, is defined as the zeroth moment of the velocity distribution:

$$\rho = \sum_{i=1}^{b} n_i$$

2. Flow velocity $\mathbf{u}$, the first moment:

$$\mathbf{u} = \frac{1}{\rho}\sum_{i=1}^{b} \mathbf{c}_i n_i \tag{2.1.3}$$

3. The specific energy e, the second moment:

$$e = \frac{1}{\rho}\sum_{i=1}^{b} |\mathbf{c}_i'|^2 n_i \qquad where\ \mathbf{c}_i' = \mathbf{c}_i - \mathbf{u}$$

4. The specific total energy $e_t = e + \frac{1}{2}|\mathbf{u}|^2$

The definition of other thermodynamic quantities is not as straightforward and requires more care. The primary reason for this is the finiteness of the phase space. In fact, temperature in discrete-velocity gases is most often wrongly defined, owing mainly to using the same definitions as for a perfect gas in classical kinetic theory. The problem with such definitions is that they are then inconsistent with thermodynamics. A discussion of other thermodynamic quantities is deferred to a later chapter since for the present purpose, the above definitions are sufficient.

2.2 Equilibrium Equations and Collisions

The problem considered is this: Suppose the discretization of the velocity set is decided upon, say based on considerations of symmetry. The model is then complete if the set of collisions among particles of the various velocities is specified. The question is how can one determine the set of necessary collisions to fully define the model? For example, are binary collisions enough or are tertiary and/or higher order collisions necessary? The following procedure enables us to get a *a priori* set of appropriate collisions, and this can be done given any discrete velocity set, in any number of dimensions and any geometry. It only assumes, as we require, that there is a unique distribution of velocities at a thermodynamic equilibrium specified by the macroscopic variables mass, momentum, and energy. In fact, even the requirements of conservation of mass, momentum, and energy in each of the collisions comes out of the analysis. This discussion is carried out for discrete-velocity gases. The procedure can easily be repeated for lattice gases, by tagging on the effects of exclusion. In fact, even that is unnecessary, because the required collisions in a given lattice gas turn out to be same as that for the corresponding discrete-velocity gas.

Thermodynamic equilibrium at a given given value of mass, momentum, and energy can be defined as that state in which the set of variables N_a[‡] assume values such that they

‡ the velocity distribution function integrated over a large enough uniform region of space so that the numbers N_a

satisfy the mass, momentum, and energy requirements while also maximizing the number of possible permutations among the particles which leave the macroscopic state unchanged. In other words, it corresponds to a maximization of the number of number of microstates for a given macrostate. Since we are interested in a unique distribution function, it is assumed that every macrostate specified by a mass, momentum, and energy corresponds to a unique set of numbers N_a, the number of particles of the various types allowed. The function representing the number of microstates corresponding to any given set of numbers N_a is easily seen to be

$$Z(N_a) = \frac{N!}{\Pi_{a=1}^{b} N_a!} \tag{2.2.1}$$

with the N_a satisfying the mass, momentum and energy specifications:

$$\sum_{a=1}^{b} N_a = N; \qquad \sum_{a=1}^{b} \mathbf{c}_a N_a = N\bar{\mathbf{c}} = N\mathbf{u}; \qquad \sum_{a=1}^{b} \frac{|\mathbf{c}_a - \mathbf{u}|^2}{2} N_a = Ne \tag{2.2.2}$$

The correct set of numbers N_a is that which maximizes $Z(N_a)$ under the above $D+2$ constraints (D being the number of dimensions), *i.e.*, the correct N_a satisfies the equations

$$\frac{\partial Z}{\partial N_a}(N_c) = 0 \qquad c = 1, \ldots, b \qquad a = 1, \ldots, b - D - 2 \tag{2.2.3}$$

Or incorporating the constraints,

$$\frac{\partial Z}{\partial N_a}(N_1, N_2, ..., N_{b-D-2}, \rho, \mathbf{u}, e) = 0 \qquad a = 1, \ldots, b - D - 2 \tag{2.2.4}$$

After carrying out the differentiation, $\rho, \mathbf{u}, e$ may be eliminated from the above equations to get $b - D - 2$ equations in b variables and these are the equilibrium equations for the model. Any of these equations can be put in the form

$$\sum \pm\psi_0(1 + N_a) = 0 \tag{2.2.5}$$

The sum always has an even number of terms and ψ_0 is the digamma function which is the first derivative of the log of the gamma function

$$\psi_0(x) = \frac{d}{dx}\log\Gamma(x), \qquad \text{where } \psi_0(n) = -\gamma + \sum_{k=1}^{n-1} \frac{1}{k} \quad \text{for } n \text{ integral}, \quad \gamma = 0.577\ldots \tag{2.2.6}$$

---

are *large*.

The numbers N_a are very large in the thermodynamic limit and the behavior of the digamma function for large arguments is logarithmic. Therefore the equilibrium equations Eq. 2.2.5 can be rewritten as

$$\log N_i + \log N_j \ldots = \log N_p + \log N_q \ldots \Rightarrow N_i N_j \ldots = N_p N_q \ldots \tag{2.2.7}$$

These can now be looked at from a collision point of view: the equilibrium equations dictate that there be detailed balancing of a set of collisions. On inspection, it is also seen that the collisions dictated by the equations are such that each one of them conserves mass, momentum, and energy.

No assumptions have yet been made regarding either the geometry or the dimensions of the model. Restricting to 2-D for simplicity and carrying out the above procedure for the square lattice, irrespective of the number of speeds involved, the equilibrium equations Eq. 2.2.7 are all seen to be of the form $N_a N_b = N_p N_q$, *i.e.*, two body collisions are sufficient for a unique thermodynamic equilibrium. Repeating the procedure for a triangular lattice, it is seen that while some of the equilibrium equations Eq. 2.2.7 are of the form $N_a N_b = N_p N_q$, others are of the form $N_a N_b N_c = N_p N_q N_r$. That is, in addition to two body collisions, three body collisions[♯] are necessary for a unique thermodynamic equilibrium on a triangular lattice, *irrespective of the number of speeds allowed.*

From now on, it is more convenient to work with a probabilistic formulation of the fractional velocity distribution function. The macroscopic flow velocity and the specific energy definitions are reproduced here:

$$\mathbf{u} = \bar{\mathbf{c}} = \sum_{i=1}^{b} \mathbf{c}_i F_d(\mathbf{c}_i); \qquad e = \sum_{i=1}^{b} \frac{(\mathbf{c}_i - \bar{\mathbf{c}})^2}{2} F_d(\mathbf{c}_i) \tag{2.2.8}$$

The equilibrium equations Eq. 2.2.7 are similarly rewritten as

$$F_d(\mathbf{c}_i) F_d(\mathbf{c}_j) \ldots = F_d(\mathbf{c}_p) F_d(\mathbf{c}_q) \ldots; \quad \cdots \tag{2.2.9}$$

♯ For a substantial number of three body collisions to occur, the density must be higher than when only binary collisions are enough. Thus on a triangular lattice, the density should be higher than on the square lattice. This requirement may question the propriety of using the model Boltzmann equations to describe the dynamics.

The equilibrium velocity distribution is thus fully determined by the $D+2$ Eq. 2.1.2 and Eq. 2.2.8 and the $b-D-2$ equilibrium equations Eq. 2.2.9, which may in general be solved numerically to obtain the velocity distribution function. However some analysis, gives useful insight and also helps interpret the numerical results. To refer to the equilibrium velocity distribution without knowing it explicitly as the solution of the aforementioned set of equations, the set of b equations, Eq. 2.1.2, Eq. 2.2.8 and Eq. 2.2.9, is termed the *implicit* discrete Maxwell-Boltzmann distribution.

At this point, the effects of exclusion, as they arise in a lattice gas due to discretization of space, can be included by simply rewriting Eq. 2.2.9 in terms of $\hat{F}_d$. The equilibrium equations in a lattice gas are therefore of the form

$$\hat{F}_d(\mathbf{c}_i)\hat{F}_d(\mathbf{c}_j)\ldots = \hat{F}_d(\mathbf{c}_p)\hat{F}_d(\mathbf{c}_q)\ldots; \quad \cdots \quad \text{where} \quad \hat{F}_d(\mathbf{c}_i) = \frac{F_d(\mathbf{c}_i)}{1-F_d(\mathbf{c}_i)} \tag{2.2.10}$$

All the calculations in this thesis, done in the context of *velocity discretization only*, can be repeated with the *hat*-variables in the equilibrium equations, as in Eq. 2.2.10 to include the effects of exclusion in a lattice gas.

2.3 Stationary Equilibrium

From the form of Eq. 2.2.9, $\log(F_d(\mathbf{c}_a))$ is a collisional invariant, and since the only conserved quantities in a collision are mass, momentum, and energy, $\log(F_d(\mathbf{c}_a))$ has to be a linear combination of mass, momentum and energy, or

$$F_d(\mathbf{c}_a)F_a = \exp(\alpha + \mathbf{b}.\mathbf{c}_a + \beta {\mathbf{c}_a}^2)\,. \tag{2.3.1}$$

When the macroscopic flow velocity is zero, $\mathbf{b}=0$ *i.e.*, all the directions are equally preferred. Then substituting Eq. 2.3.1 in Eq. 2.1.2 and Eq. 2.2.8,

$$\exp(\alpha)\sum_a \exp(\beta {\mathbf{c}_a}^2) = 1; \qquad \exp(\alpha)\sum_a \mathbf{c}_a^2 \exp(\beta \mathbf{c}_a^2) = 2e\,. \tag{2.3.2}$$

At this point, it is useful to introduce a dimensionless parameter characterizing the discretization of velocity* in the model. A natural choice for this is $\tilde{q} = q/\sqrt{e}$, where q is the unit of speed in the model. Consequently, it is convenient to non-dimensionalize β by e, $\tilde{\beta} = \beta e$. The discretization parameter $\tilde{q} = q/\sqrt{e}$ measures how far away the model is from the continuous velocity case ($\tilde{q} = 0$ implies a continuous velocity gas). Define

$$G = \sum_a \exp(\tilde{\beta}\tilde{q}^2\tilde{\mathbf{c}}_a^2)\,, \tag{2.3.3}$$

with $\tilde{\mathbf{c}}_a$ a non-dimensional vector coinciding with the particle velocity vector $\mathbf{c}_a$. Using the definition of G in Eq. 2.3.2 gives

$$\sum_a \tilde{\mathbf{c}}_a^2 \exp(\tilde{\beta}\tilde{q}^2\tilde{\mathbf{c}}_a^2) = \frac{2G}{\tilde{q}^2}\,. \tag{2.3.4}$$

Equivalently,

$$\frac{d\log G}{d(\tilde{\beta}\tilde{q}^2)} = \frac{2}{\tilde{q}^2}\,, \tag{2.3.5}$$

where now $\tilde{\beta}$, $\tilde{q}$ and G are all non-dimensional, and the dependence of the distribution function on the model is reduced to the dependence of G on the model. In two dimensions on the square lattice $\tilde{\mathbf{c}}_a^2 = {c_{ax}}^2 + {c_{ay}}^2$ and on the triangular lattice, $\tilde{\mathbf{c}}_a^2 = \tilde{c}_{a\xi}^2 + \tilde{c}_{a\eta}^2 + \tilde{c}_{a\xi}\tilde{c}_{a\eta}$, with $\tilde{c}_{ax}$, $\tilde{c}_{ay}$ or $\tilde{c}_{a\xi}$, $\tilde{c}_{a\eta} = \ldots -2, -1, 0, 1, 2, \ldots$ In the limit of having an infinite number of velocities in each direction, with each velocity being an integral multiple of the unit velocity q, G is the sum of a (multidimensional) infinite series. This series is highly convergent. Incidentally these infinite sums can be expressed in terms of theta functions** at $z = 0$ for the various geometries and dimensions. For example on the square lattice in two dimensions,

$$G = {\Theta^2}_3(0; e^{\tilde{\beta}\tilde{q}^2})\,, \tag{2.3.6}$$

and on the triangular lattice,

$$G = \Theta_3(0; e^{\tilde{\beta}\tilde{q}^2/4})\Theta_3(0; e^{3\tilde{\beta}\tilde{q}^2/4})\,. \tag{2.3.7}$$

---

* more precisely the speed.

** since the complex variable z is the argument of a theta function, with z identically 0, use of the theta function is no more than a notational convenience in the present case.

The Euler-Maclaurian series summation formula for a general function $f(j)$ can be written as

$$\sum_{0}^{n} f(j) = \int_{0}^{n} f(x)dx + R(f;n)\,, \tag{2.3.8}$$

where $R(f;n)$ is loosely called the remainder†. The above formula can be used to express the infinite series G as the sum of an integral and other terms. The integral can be evaluated exactly:

$$\int_{0}^{\infty} \exp(\tilde{\beta}\tilde{q}^2 r^2)\, 2\pi r dr = -\frac{\pi}{\tilde{\beta}\tilde{q}^2} \tag{2.3.10}$$

Consider first, the continuous velocity limit‡ of the discrete velocity gases on the square and the triangular geometry. It is seen that the terms other that the integral in the Euler-Maclaurian formula for the sum G depend multiplicatively on $\tilde{\beta}^2\tilde{q}^2$ (the log of the argument of the theta function). Therefore, when $\tilde{q}$ is let to go to 0, these terms vanish and on both the square and triangular lattices, G is given by the integral in Eq. 2.3.10, $-\frac{\pi}{\tilde{\beta}\tilde{q}^2}$. Using this value of G in Eq. 2.3.5 gives $\tilde{\beta} = -0.5$, independent of $\tilde{q}$. This corresponds exactly to the Maxwell-Boltzmann velocity distribution for the continuous velocity ideal gas: from Eq. 2.3.1,

$$F(\mathbf{c}) = \exp(\alpha)\exp(-\frac{\mathbf{c}^2}{2e}) \tag{2.3.11}$$

Thus the limiting behavior of the discrete velocity gases both on the square and triangular lattices is seen to be correct.

The error in discrete-velocity gases, still with an infinite number of velocities is tied to the finiteness of the discretization parameter $\tilde{q}$ and is given by the remainder terms of

---

† $$R(f;n) = \frac{1}{2}(f(n) + f(0)) + \sum_{r} b_{2r}(f^{2r-1}(n) - f^{2r-1}(0)) + \sum_{0}^{n-1} \int_{m}^{m+1} P_{2r+1}(x-m) f^{2r+1}(x)dx$$

$$b_r = \frac{B_r}{r!}; \qquad P_r(x) = \frac{\phi_r(x)}{r!} \tag{2.3.9}$$

$$P_r'(x) = b_{r-1} + P_{r-1}(x); \qquad P_r(0) = 0; \qquad b_r = -\int_{0}^{1} P_r(x)dx$$

where B_r are the Bernoulli numbers and ϕ_r are the Bernoulli polynomials.

‡ In the sense of $\tilde{q}$ going to 0.

Eq. 2.3.8, used in evaluating G. Since these terms are difficult to determine analytically, and since the series definition of G, given in Eq. 2.3.3, is highly convergent, G is easily evaluated numerically. These values of G when used in Eq. 2.3.5 give the variation of $\tilde{\beta}$ with the discretization parameter $\tilde{q}$.

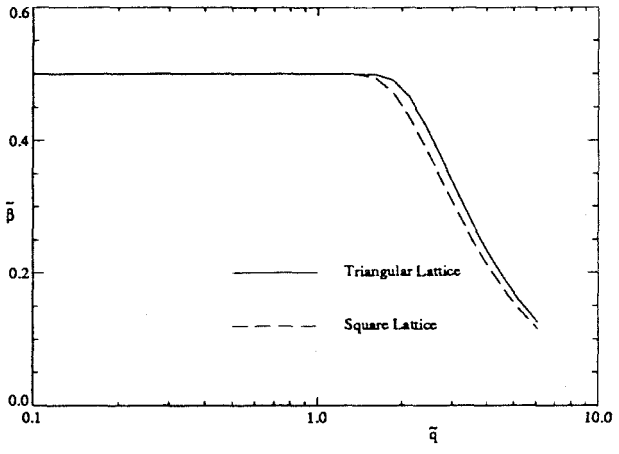

FIG. 2.3.1 The error in $\tilde{\beta}$ due to discretization on the square and triangular lattices. For a fixed unit velocity q, this error is important at low values of specific energies. Note log scale on the x-axis.

Shown in Fig. 2.3.1 is the variation of $-\tilde{\beta}$ with $\tilde{q}$ for the square and triangular lattices in two dimensions. $\tilde{\beta} = -0.5$ at $\tilde{q} = 0$ corresponds to the continuous velocity limit of $\beta = 1/2e$. The deviation of $\tilde{\beta}$ from -0.5 is due to discretization of the velocity components in terms of a non-zero unit velocity and can therefore be thought of as a **discretization error**. A couple of noteworthy features of the discretization error as seen in Fig. 2.3.1 are

1. For a fixed unit velocity q, this error is increasingly important at low values of the specific internal energy.

2. The error is very small till a $\tilde{q}$ of about 1.5. The engineering consequences of this are encouraging.

Next consider the case when the number of velocity components allowed is finite. Then, there is the additional effect of truncating the series sum G and this error can be thought

of as a **truncation error**. This effect is again dependent on $\tilde{q}$, but for a fixed unit velocity q, this effect is more important when the value of the specific energy is high[♯]. Since the series G now has only a finite (for the models to be considered, small) number of terms, it is easier to deal with the original equations. Reverting back to Eq. 2.3.2, the discrete Maxwell Boltzmann distribution for the stationary case can be written as

$$F_a = \frac{x^{\tilde{c}_a^2}}{\sum_a x^{\tilde{c}_a^2}}, \tag{2.3.12}$$

where x $(= \exp \tilde{\beta}\tilde{q}^2)$ satisfies the polynomial equation

$$\sum_a (\frac{2}{\tilde{q}^2} - \tilde{c}_a^2) x^{\tilde{c}_a^2} = 0\,. \tag{2.3.13}$$

The velocity distribution (presently the speed distribution) is fully determined if the variation of $x = \exp \tilde{\beta}\tilde{q}^2$ with $\tilde{q}$ (equivalently e) is determined. The above equation is a polynomial equation in x and the equation cannot be solved explicitly if it is of degree greater than three. The numerical solution is presented as a plot of $-\tilde{\beta}$ *v.* $\tilde{q}$ for the different models on the square and triangular lattices in Fig. 2.3.2. The number of velocities in the models considered on the square lattice are 9, 25, 49, 81, 121 and ∞ and on the triangular lattice are 19, 37, 61, 91 and ∞ (see section 1.3.1 and Fig. 1.2.2). The error on the right i.e for $\tilde{q}$ large is the discretization error previously discussed. All the curves, except the ones for ∞ go away to $\tilde{\beta} = \infty$ at $\tilde{q}_{min}$, so that only the highest speed allowed in the model occurs, and none else. As previously said, a $\tilde{\beta}$ of -0.5 corresponds to a Gaussian distribution of velocities, as in ideal gases.

♯ This is rather obvious because there is a maximum of the specific internal energy allowed in the model.

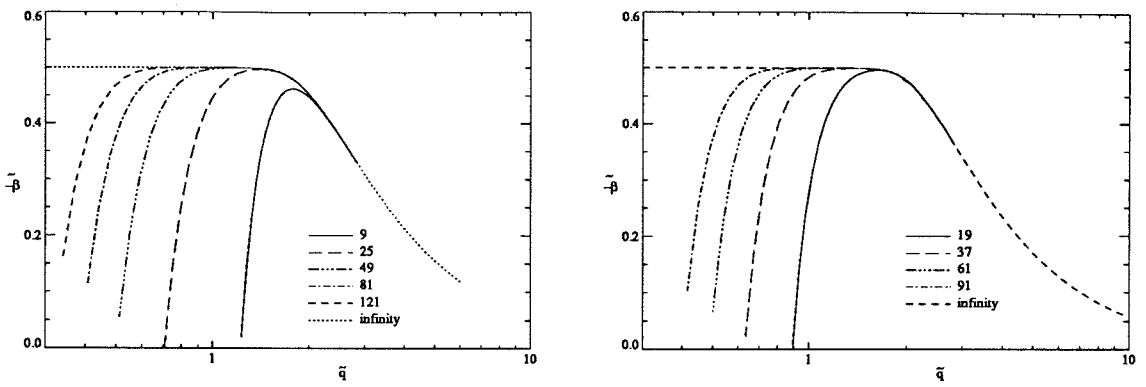

FIG. 2.3.2 The error in $\tilde{\beta}$ due to allowing only a finite number of velocity components. Note log scale on the x-axis(a)**Square lattice** (b)**Triangular lattice**

2.4 The Non-Stationary Equilibrium Distribution *via* a Perturbation Expansion

The exact Maxwell-Boltzmann distribution in the context of discrete-velocity gases, Eq. 2.3.1, is rewritten here for convenience.

$$F_a = F_d(\mathbf{c}_a) = \exp(\alpha + \mathbf{b}.\mathbf{c}_a + \beta {\mathbf{c}_a}^2) \tag{2.4.1}$$

The only vectorial dependence of the coefficients can come from **u**. Therefore, **b** can be written as $b\mathbf{u}$, where b is a scalar coefficient and not the magnitude of **b** used above. The distribution has three parameters — α, b, and β, and these are to be determined to satisfy the mass, momentum, and energy considerations. This cannot however be done exactly analytically in the context of discrete-velocity gases mainly because of the the finiteness of the velocity space, which brings in a nontrivial dependence* of the velocity distribution function on the macroscopic flow velocity. Therefore resorting to a perturbation series in u, doing it here only to $O(\mathbf{u}^2)$,

$$\begin{aligned} \alpha &= \alpha_0(e) + \alpha_1(e)\mathbf{u}^2 + O(\mathbf{u}^3) \\ b &= b_0(e) + b_1(e)\mathbf{u}^2 + O(\mathbf{u}^3) \\ \beta &= \beta_0(e) + \beta_1(e)\mathbf{u}^2 + O(\mathbf{u}^3) \end{aligned} \tag{2.4.2}$$

* for a perfect gas, b can be set identically to 0 by changing the frame of reference to one traveling with the macroscopic flow velocity.

which when used in Eq. 2.4.1 gives

$$F_a = \exp(\alpha_0 + \beta_0 \mathbf{c_a}^2)\ \exp(b_0 \mathbf{c_a}.\mathbf{u})\ \exp((\alpha_1 + \beta_1 \mathbf{c_a}^2)\mathbf{u}^2)\ \exp(O(\mathbf{u}^3)) \tag{2.4.3}$$

If $\mathbf{u}$ is small enough for $\mathbf{u}^3$ to be negligible,

$$F_a = F_{|a|}(e)\left(1 + b_0(e)\mathbf{c_a}.\mathbf{u} + \frac{1}{2}b_0^2(e)(\mathbf{c_a}.\mathbf{u})^2 + (\alpha_1(e) + \beta_1(e)\mathbf{c_a}^2)\mathbf{u}^2 + O(\mathbf{u}^3)\right) \tag{2.4.4}$$

where $F_{|a|} = \exp(\alpha_0 + \beta_0 \mathbf{c_a}^2)$ is the previously discussed stationary distribution. The mass, momentum and energy considerations reproduced here

$$\sum_a F_a = 1, \qquad \sum_a \mathbf{c_a} F_a = \mathbf{u}, \qquad \sum_a \mathbf{c_a}^2 F_a = 2e + \mathbf{u}^2 \tag{2.4.5}$$

then determine the coefficients α_1, b_0, and β_1 for any model. At this point, it is convenient to introduce a set of tensors of various orders, denoted by $\mathbf{E}^{(2)}$, $\mathbf{E}^{(4)}$, *etc...* and defined by

$$E_{\alpha\beta\gamma\delta\ldots} = \sum_{a=1}^{b} F_{|a|} c_{a\alpha} c_{a\beta} c_{a\gamma} c_{a\delta} \cdots \tag{2.4.6}$$

Note that the E tensor of a given order is simply a convenient notation to represent all possible moments of the stationary distribution function of that order. In addition to simplifying the algebra tremendously, these tensors are capable of characterizing fully the directional behavior of the models. In the rest of this chapter, the specific energy e is assumed non-dimensionalized by q^2 and any velocity by q.

2.4.1 Structure of the E Tensors

A momentary digression to take a look at the structure of these $\mathbf{E}$ tensors on the square and triangular lattices is worthwhile. The reader is referred to Wolfram (1986) for a good discussion of the subject.

- From their definition, it is seen that the $\mathbf{E}$ tensors are symmetric over all their indices.

- The symmetry of the square and triangular lattices constrain the odd order **E** tensors to be identically zero.

$$\mathbf{E}^{2n+1} = 0\,, \qquad n = 0, 1, 2, \ldots \tag{2.4.7}$$

- The second order tensors on both the geometries is again the same from symmetry considerations and is given by

$$E_{\alpha\beta} = e\delta_{\alpha\beta} \tag{2.4.8}$$

They are seen to be isotropic.

The higher (even) order tensors however have a different form on the two geometries: for two spatial dimensions, the isotropic 4-tensor, denoted by $\Delta_{\alpha\beta\gamma\delta}$ has the form $\delta_{\alpha\beta}\delta_{\gamma\delta} + \delta_{\alpha\gamma}\delta_{\beta\delta} + \delta_{\alpha\delta}\delta_{\beta\gamma}$ and can be conveniently denoted by indicating only its upper simplical** components: (3,0,1,0,3). The structure of the 4-tensors on the square and triangular geometries is discussed below:

- Square Geometry: In terms of the upper simplical components, the 4-tensor is given by $(e_{41}, 0, e_{42}, 0, e_{41})$. The expressions for one of the components e_{42}, can be derived explicitly without having to know even the stationary distribution as follows:

$$e_{42} = E_{1122} = \sum_{a} F_{|a|} c_{ax}^2 c_{ay}^2 = \sum_{ax,ay} F_{|ax|} F_{|ay|} c_{ax}^2 c_{ay}^2\,, \tag{2.4.9}$$

Since the probability of the velocity $\mathbf{c}_a$ occurring, is the joint probability of its velocity components c_{ax} and c_{ay} occurring, and since the distribution of the two components are relatively independent†, the joint probability can be replaced by

---

** the indices form a non-increasing sequence: Thus for $E_{\alpha\beta}$, (E_{11}, E_{21}, E_{22}) are indicated and so on. The upper simplical components are sufficient to describe the **E** tensors completely because of the symmetry of tensors in all its indices, as seen by the definition in Eq. 2.4.6.

† This is not true in the case of the triangular lattice and therefore this argument cannot be used to determine e_{42} there.

the product of the two probabilities. Therefore,

$$e_{42} = \left(\sum_{ax} F_{|ax|}c_{ax}^2\right)\left(\sum_{by} F_{|by|}c_{by}^2\right) = \left(\sum_{a} F_{|ax|}c_{ax}^2\right)\left(\sum_{b} F_{|by|}c_{by}^2\right) = e^2 \tag{2.4.10}$$

because $$\sum_{a} F_{|a|}c_{ax}^2 = \sum_{ax,ay} F_{|ax|}F_{|ay|}c_{ax}^2 = \sum_{ay} F_{|ay|}\sum_{ax} F_{|ax|}c_{ax}^2 = \sum_{ax} F_{|ax|}c_{ax}^2 \tag{2.4.11}$$

So that $E_{\alpha\beta\gamma\delta} = (e_{41}, 0, e^2, 0, e_{41})$. Since this is not, in general, of the isotropic form (any isotropic 4-tensor can only be a scalar multiple of *the* isotropic 4-tensor $\Delta_{\alpha\beta\gamma\delta}$, and therefore can have only one independent component), it can be decomposed into an isotropic component and an anisotropic component:

$$E_{\alpha\beta\gamma\delta} = e^2(3,0,1,0,3) + (e_{41} - 3e^2)(1,0,0,0,1) = e^2\Delta_{\alpha\beta\gamma\delta} + (e_{41} - 3e^2)\delta_{\alpha\beta\gamma\delta}\ , \tag{2.4.12}$$

- Triangular Geometry: First consider the 4-tensor generated by the velocity vectors directed towards the corners of a regular hexagon (with one of the corners on the x-axis. After considering the symmetries, it is enough to look at the ratio E_{1111}/E_{1122} to determine the form of the 4-tensor. Since, all the six velocities are of the same speed they occur with equal probability ($\frac{1}{6}$) in the stationary state. Therefore from Eq. 2.4.6,

$$\frac{E_{1111}}{E_{1122}} = \frac{4\frac{1}{6}\left(\frac{1}{2}\right)^4 + 2\frac{1}{6}1^4}{4\frac{1}{6}\left(\frac{1}{2}\right)^2\left(\frac{\sqrt{3}}{2}\right)^2} = 3 \tag{2.4.13}$$

The 4-tensor generated by a hexagon, therefore, has the isotropic form $(\ )\Delta_{\alpha\beta\gamma\delta}$. Any model on the triangular lattice can be written as a sum over regular hexagons of various sizes oriented differently with respect to a common x-axis. Then, since the 4-tensor generated by each of the hexagons is isotropic, they retain the same form on transformation to the global coordinates and thus the 4-tensor of the given model is obtained simply by scalar addition of the coefficients‡. Thus the 4-tensor

‡ This cannot be done on the square lattice because even though any model can be written as the sum over squares of different sizes, the 4-tensors cannot be simply added back because the 4-tensors of the squares are anisotropic and therefore change form on transformation to the global coordinates.

on the triangular grid is isotropic: $E_{\alpha\beta\gamma\delta} = e_{41}(e)\Delta_{\alpha\beta\gamma\delta}$

2.4.2 The Distribution Correct to O($\mathbf{u}^2$)

The three moments in Eq. 2.4.5, using the perturbation expansion Eq. 2.4.4 can be rewritten in terms of the **E** tensors as

$$\sum_a F_a = \mathbf{E}^{(0)} + b_0 E_\alpha u_\alpha + \frac{1}{2} b_0^2 E_{\alpha\beta} u_\alpha u_\beta + (\alpha_1 \mathbf{E}^{(0)} + \beta_1 E_{\alpha\alpha}) u_\beta u_\beta + O(\mathbf{u}^3) = 1$$

$$\sum_a F_a \mathbf{c}_a = E_\alpha + b_0 E_{\alpha\beta} u_\beta + \frac{1}{2} b_0^2 E_{\alpha\beta\gamma} u_\beta u_\gamma + (\alpha_1 E_\alpha + \beta_1 E_{\alpha\beta\beta}) u_\gamma u_\gamma + O(\mathbf{u}^3) = \mathbf{u} \quad (2.4.14)$$

$$\sum_a F_a \mathbf{c}_a^2 = E_\alpha \alpha + b_0 E_{\alpha\alpha\beta} u_\beta + \frac{1}{2} b_0^2 E_{\alpha\alpha\beta\gamma} u_\beta u_\gamma + (\alpha_1 E_{\alpha\alpha} + \beta_1 E_{\alpha\alpha\beta\beta}) u_\gamma u_\gamma + O(\mathbf{u}^3) = 2e + \mathbf{u}^2$$

The second of Eq. 2.4.14, along with the structure of the **E** tensors discussed in the previous subsection gives $b_0 = 1/e$. Similarly the first and the third of Eq. 2.4.14 can be used to determine α_1 and β_1. Since they involve 4-tensors which are different for the two geometries, the resulting expressions are different.

- Square Geometry:

$$\beta_1 = -\frac{1}{4e^2} \frac{e_{41} - 3e^2}{e_{41} - e^2}, \qquad \alpha_1 = -\frac{e}{e_{41} - e^2} \quad (2.4.15)$$

- Triangular Geometry:

$$\beta_1 = -\frac{1}{2e^2} \frac{e_{41} - 3e^2}{2e_{41} - 3e^2}, \qquad \alpha_1 = -\frac{3}{2} \frac{e}{2e_{41} - 3e^2} \quad (2.4.16)$$

2.4.3 The Equilibrium Momentum Flux Tensor

To get a better insight into the velocity dependence of the distribution function, further discussion is carried out in terms of the equilibrium momentum flux tensor.

$$P_{\alpha\beta} = \rho \sum F_a c_{a\alpha} c_{a\beta} \tag{2.4.17}$$

Substituting F_a correct to $O(\mathbf{u}^2)$ as given by Eq. 2.4.4 in the above definition gives the equilibrium momentum flux tensor correct to $O(\mathbf{u}^2)$. This can be written in index notation as

$$\begin{aligned} P_{\alpha\beta} = \rho \sum F_{|a|} \Big(& c_{a\alpha} c_{a\beta} + b_0 c_{a\alpha} c_{a\beta} c_{a\gamma} u_\gamma + \frac{1}{2} b_0^2 c_{a\alpha} c_{a\beta} c_{a\gamma} c_{a\delta} u_\gamma u_\delta \\ & + c_{a\alpha} c_{a\beta} (\alpha_1 + \beta_1 c_{a\gamma} c_{a\gamma}) u_\delta u_\delta \Big) \end{aligned} \tag{2.4.18}$$

Or in terms of the **E** tensors as

$$P_{\alpha\beta} = \rho \left[E_{\alpha\beta} + \frac{1}{2} b_0^2 E_{\alpha\beta\gamma\delta} u_\gamma u_\delta + (\alpha_1 E_{\alpha\beta} + \beta_1 E_{\alpha\beta\gamma\gamma}) u_\delta u_\delta + O(\mathbf{u}^3) \right] , \tag{2.4.19}$$

noting that the term $b_0 E_{\alpha\beta\gamma} u_\gamma$ has not been written because the odd order tensors are identically zero on both the square and the triangular lattices. The *scalar*$^\sharp$ coefficient of $\delta_{\alpha\beta}$ in the above expression for the equilibrium momentum flux tensor can then be identified as pressure.

Substituting the form of the tensors discussed in Sec. 2.4.1 into Eq. 2.4.19, the equilibrium momentum flux tensor takes the form

- Square Geometry*

$$\begin{aligned} P_{\alpha\beta} = \rho \left[e + \left(\frac{1}{2} + \alpha_1 e + \ \beta_1 (e_{41} + e^2) \right) \mathbf{u}^2 \right] \delta_{\alpha\beta} + \rho u_\alpha u_\beta \\ + \rho \frac{e_{41} - 3e^2}{2e^2} \delta_{\alpha\beta\gamma\delta} u_\gamma u_\delta + O(\mathbf{u}^3) \end{aligned} \tag{2.4.20}$$

$^\sharp$ coordinate independent

* $E_{\alpha\beta\gamma\gamma} = e^2 \Delta_{\alpha\beta\gamma\gamma} + (e_{41} - 3e^2)\delta_{\alpha\beta\gamma\gamma}$
$= 4e^2 \delta_{\alpha\beta} + (e_{41} - 3e^2)\delta_{\alpha\beta}$
$= (e_{41} + e^2)\delta_{\alpha\beta}$

The pressure on the square lattice is therefore identified to be

$$p = \rho \left[e + \left(\frac{1}{2} + \alpha_1 e + \beta_1 (e_{41} + e^2) \right) \mathbf{u}^2 + O(\mathbf{u}^3) \right] \tag{2.4.21}$$

Substituting for α_1 and β_1 in terms of e_{41},

$$p = \rho \left(e - \frac{e_{41} - 3e^2}{4e^2} \mathbf{u}^2 + O(\mathbf{u}^3) \right) \tag{2.4.22}$$

The simplified form of the equilibrium momentum flux tensor on the square lattice is therefore

$$P_{\alpha\beta} = \rho(e - \frac{\Psi}{4}\mathbf{u}^2)\delta_{\alpha\beta} + \rho u_\alpha u_\beta + \frac{\Psi}{2}\delta_{\alpha\beta\gamma\delta}\rho u_\gamma u_\delta + O(\mathbf{u}^3), \quad \Psi = \frac{e_{41}}{e^2} - 3 \tag{2.4.23}$$

A few features worth noting about the form of the equilibrium momentum flux tensor in Eq. 2.4.23 are:

- The kinematic dependence of pressure, given by Ψ to $O(\mathbf{u}^2)$.
- The correct advection velocity, indicated by the unity coefficient of $\rho u_\alpha u_\beta$ in Eq. 2.4.23.
- The form of the anisotropy of models on the square lattice, and the magnitude again given by Ψ to $O(\mathbf{u}^2)$
- The recovery of isotropy ($\Psi = 0$) in these models, when $e_{41} = 3e^2$. The equilibrium momentum flux tensor is then *exactly* of the form for perfect gases, correct to $O(\mathbf{u}^2)$: $\rho e \delta_{\alpha\beta} + u_\alpha u_\beta$

- Triangular Geometry: Going through as for the square lattice,

$$P_{\alpha\beta} = \rho \left(e - \frac{\Psi}{6}\mathbf{u}^2 \right) \delta_{\alpha\beta} + \frac{e_{41}}{3e^2}\rho u_\alpha u_\beta + O(\mathbf{u}^3), \quad \Psi = \frac{e_{41}}{e^2} - 3 \tag{2.4.24}$$

It may be noted that when $e_{41} = 3e^2$, the tensor is again identically that for a perfect gas.

It is heartening to see that after pages of algebra, all the deviations from the familiar equilibrium momentum flux tensor are captured by one term which characterizes the deviation of the 4-tensor of the model from the isotropic form. Comparing the momentum flux tensor on the two geometries, it is seen that the anisotropy of the square lattice has been traded for the incorrect advection velocity on the triangular lattice.

2.4.4 The Deviation Ψ for the Different Models

For the nine-velocity model, the above algebra can be carried out explicitly. The functional forms obtained are as follows:

$$F_{|0|} = (1-e)^2, \qquad F_{|1|} = \frac{1}{2}e(1-e), \qquad F_{|2|} = \frac{1}{4}e^2 \tag{2.4.25}$$

$$b_0 = \frac{1}{e}, \qquad \alpha_1 = -\frac{1}{(1-e)}, \qquad \beta_1 = -\frac{1-3e}{4e^2(1-e)} \tag{2.4.26}$$

$$E_{\alpha\beta} = e\delta_{\alpha\beta} = e(1,0,1), \qquad \text{and} \qquad E_{\alpha\beta\gamma\delta} = e^2(\frac{1}{e},0,1,0,\frac{1}{e}) \tag{2.4.27}$$

where again the upper simplical components are indicated; $e_{41} = e$. The isotropic and anisotropic components of $E_{\alpha\beta\gamma\delta}$ are therefore

$$E_{\alpha\beta\gamma\delta} = e^2(3,0,1,0,3) + e(1-3e)(1,0,0,0,1) = e^2\Delta_{\alpha\beta\gamma\delta} + e(1-3e)\delta_{\alpha\beta\gamma\delta} \tag{2.4.28}$$

The equilibrium momentum flux in the nine-velocity model therefore has the explicit form

$$P_{\alpha\beta} = \rho\left(e - \frac{1-3e}{4e}\mathbf{u}^2\right)\delta_{\alpha\beta} + \rho u_\alpha u_\beta + \frac{1-3e}{2e}\rho u_\alpha u_\beta \delta_{\alpha\beta} + O(\mathbf{u}^3) \tag{2.4.29}$$

and the pressure is given by

$$p = \rho\left(e - \frac{1-3e}{4e}\mathbf{u}^2 + O(\mathbf{u}^3)\right) \tag{2.4.30}$$

Since the stationary velocity distribution for any of the other models involves solving polynomial equations of order four or higher, they have to be obtained numerically**. Fig. 2.4.1 shows the variation of $\Psi = e_{41}/e^2 - 3$ with $\tilde{q}$ for the different models on the square and triangular lattices.

** The stationary distribution is required in order to calculate $e_{41} = E_{1111}$, the one variable on which all the deviations depend.

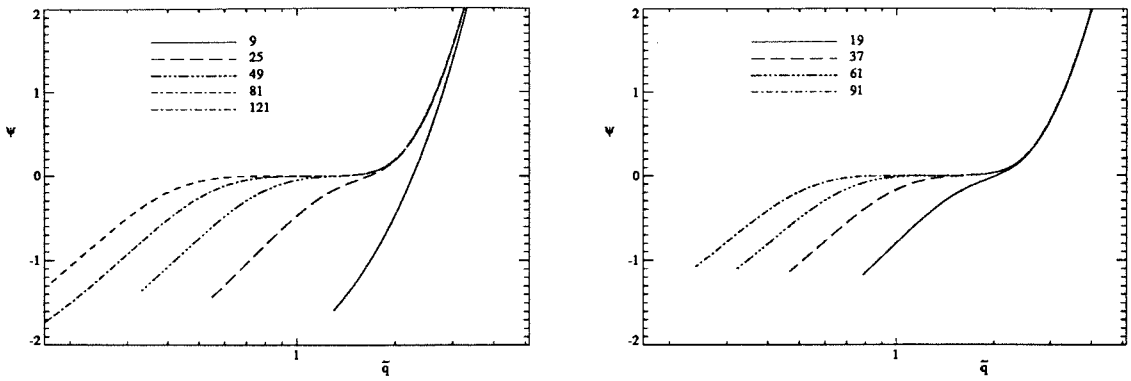

FIG. 2.4.1 The variation of $\Psi = \frac{e_{41}}{e^2} - 3$, the quantity which determines the kinematic dependence of pressure on both geometries, the anisotropy on the square geometries and the advection velocity of the triangular geometries. Shown for the different models discussed in the section on Stationary Equilibrium. (left): **Square lattice** (right): **Triangular lattice**

2.5 On Pressure in Lattice Gases

In the above discussion, since the particle velocity distribution was found analytically correct to $O(\mathbf{u}^2)$, the pressure was identified correct to $O(\mathbf{u}^2)$. It is rather interesting to note that the procedure by which pressure was identified above was purely mathematical; other definitions of pressure, as from a mechanical point of view whereby it is the average normal stress at a point when the fluid is in thermodynamic equilibrium†, or from a statistical thermodynamic point of view wherein it is the generalized force conjugate to specific volume are possible. This may suggest that the definition of pressure is not unique or that pressure itself is a poorly defined concept. This however is not true as is clear from the following simple experiment. Suppose pressure is defined by $p = p(\rho, e, u)$. Now set up an initial condition on a one-dimensional domain with a variation of say density and specific energy, the variations being such that $p(\rho, e, u)$ is constant over the domain. By following the subsequent evolution of the initial condition under the model Euler equations, the correctness of the definition of pressure‡ can be verified: if the definition was right, the

† This definition gives $p = \rho e$ identically.

‡ The definition of pressure is correct if it conforms our everyday notion of it and if it works correctly in the hydrodynamic equations.

subsequent evolution would be given by

$$\frac{D\rho}{Dt} = \frac{De}{Dt} = 0\,, \tag{2.5.1}$$

i.e., the density and specific energy profiles are simply advected with the flow velocity. If the definition was incorrect, there would be C_+ and the C_- waves generated in addition. By doing the above experiment, it was seen that at small values of the flow velocities, the definition of pressure arrived at above is much better than the $p = \rho e$ definition got from the average normal stress argument. It remains to be seen if the statistical thermodynamic definition of pressure as the generalized force conjugate to specific volume conforms to the previous definition.

Apart from all the above discussion, a question that remains is *how can one identify pressure exactly if the particle velocity distribution is known exactly but numerically?*

CHAPTER 3

A Method for Near-Equilibrium Discrete-Velocity Gas Flows

The equilibrium flux method (EFM) of Pullin (1980) is a kinetic-theory-based finite volume method for calculating the flow of a compressible ideal gas. It is shown in this chapter, how the EFM idea can be applied to a discrete-velocity gas. The EFM view of a discrete-velocity (lattice) gas allows good approximations to inviscid, non-heat conducting flows of a discrete-velocity (lattice) gas to be conveniently and efficiently calculated. To the knowledge of the author, there has not been a good way of calculating such a flow 'til now. The near-equilibrium flow techniques discussed in this chapter derive from the following EFM interpretation of an equilibrium flow:

> "the particle ensemble simulation is replaced by a scheme in which adjacent cells in a cell network interact directly through exchange of mass, momentum, and energy, the exchange in Δt being calculated using the equilibrium flux relations."*

The near-equilibrium flow techniques, therefore, use direct calculations of local kinetic transport of mass, momentum, and energy in the lattice gas with no recourse to continuum formulations in terms of partial-differential equations.

3.1 Equilibrium Fluxes

From chapter 2, thermodynamic equilibrium is defined as the state in which there is a detailed balancing of collisions. As discussed, there are a set of $b - D - 2$ relations of the form

$$n_a n_b \cdots = n_p n_q \cdots \tag{3.1.1}$$

* Pullin 1980.

which are satisfied in such an equilibrium state. The vector $\mathbf{F}$ of hydrodynamic variables comprising mass, momentum, and energy is given by

$$\mathbf{F} = (\sum_a n_a, \sum_a n_a \mathbf{c}_a, \sum_a n_a \mathbf{c}_a^2) \tag{3.1.2}$$

and $\mathbf{G}$, the flux of $\mathbf{F}$ is given by

$$\mathbf{G} = \left(\sum_a n_a \mathbf{c}_a, \sum_a n_a \mathbf{c}_a \mathbf{c}_a, \sum_a n_a \mathbf{c}_a^2 \mathbf{c}_a \right) \tag{3.1.3}$$

The definition of $\mathbf{F}$ along with the set of $b - D - 2$ thermodynamic equilibrium equations Eq. 3.1.1 (model dependent), is the *implicit* discrete Maxwell-Boltzmann distribution. Similarly, the definition of $\mathbf{G}$ used in conjunction with the equilibrium equations Eq. 3.1.1 gives the equilibrium fluxes of mass, momentum, and energy. Since the b particle populations satisfy the $b - D - 2$ equilibrium relations Eq. 3.1.1, there are $D + 2$ independent particle populations. We represent these $D+2$ independent particle populations by $\mathbf{m}$, and therefore Eq. 3.1.2 and Eq. 3.1.3 may be rewritten

$$\mathbf{F} = \mathbf{F}(\mathbf{m}), \qquad \mathbf{G} = \mathbf{G}(\mathbf{m}) \tag{3.1.4}$$

While from Eq. 3.1.2 and Eq. 3.1.3, it is clear that $\mathbf{G} = \mathbf{G}(\mathbf{F})$, the functional dependence cannot be expressed explicitly**. Finally, if the equilibrium distribution of all the b populations is denoted by $\mathbf{n}$, $\mathbf{n}$ can be calculated from $\mathbf{m}$, using Eq. 3.1.1.

** This would involve the equation of state.

3.2 Near-Equilibrium Flow in 1-D

The present near-equilibrium flow technique is best illustrated by considering it in one spatial dimension. Consider a linear array of cells tiling the one-dimensional domain. Each cell has a centroid and is bounded by two boundary elements, across which the cell interacts with its neighbors. The time evolution of the system is then reduced to a calculation at each time step of the net flux of $\mathbf{F}$ at the cell boundaries, and updating $\mathbf{F}$ using the fact that $\mathbf{F}$ is a conserved quantity. It is enough to consider the interactions of one cell at one of its boundaries because the domain is invariant under a translation by the dimension of a cell. Considering the interactions at the cell boundary at $x + \Delta x/2$, between the cells centered at x and $x + \Delta x$, the flux of $\mathbf{F}$ at $x + \Delta x/2$, $\mathbf{G}(x + \Delta x/2)$, comes from

1. the flux of $\mathbf{F}$ in the positive x-direction due to particles moving in the positive x-direction and presently in the cell $[x-\Delta x/2, x+\Delta x/2]$, called $\mathbf{G}^+(\mathbf{n}^+(x+\Delta x/2,t))$[†] where $\mathbf{n}^+$ has been used to denote the distribution of particles with a positive x-velocity, and

2. the flux of $\mathbf{F}$ in the negative x-direction due to particles moving in the negative x-direction and presently in the cell $[x+\Delta x/2, x+3\Delta x/2]$, called $\mathbf{G}^-(\mathbf{n}^-(x+\Delta x/2,t))$.

The integral form of the conservation law for $\mathbf{F}$ over the cell $[x - \Delta x/2, x + \Delta x/2]$ centered at x can then be written as

$$\frac{d}{dt}\int_{x-\frac{\Delta x}{2}}^{x+\frac{\Delta x}{2}} \mathbf{F}(\mathbf{n}(x,t))dx + \left(\mathbf{G}^+(\mathbf{n}^+(x+\frac{\Delta x}{2},t)) - \mathbf{G}^-(\mathbf{n}^-(x+\frac{\Delta x}{2},t))\right) - \left(\mathbf{G}^+(\mathbf{n}^+(x-\frac{\Delta x}{2},t)) - \mathbf{G}^-(\mathbf{n}^-(x-\frac{\Delta x}{2},t))\right) = 0 \tag{3.2.1}$$

---

† A notational clarification: The reader may observe in the coming pages that $\mathbf{G}^+$ always goes with $\mathbf{n}^+$, and $\mathbf{G}^-$ with $\mathbf{n}^-$. The notation $\mathbf{G}^+(\mathbf{n}^+)$ and $\mathbf{G}^-(\mathbf{n}^-)$ are however used to leave no room for ambiguity: $\mathbf{G}^+(\mathbf{n}^-)$ and $\mathbf{G}^-(\mathbf{n}^+)$ are meaningful quantities but never occur in the present context. $\mathbf{G}^+(\mathbf{n})$, if used is to be interpreted as $\mathbf{G}^+(\mathbf{n}^+)$ and $\mathbf{G}^-(\mathbf{n})$ as $\mathbf{G}^-(\mathbf{n}^-)$. It may also be noticed that $\mathbf{G}^+$ and $\mathbf{G}^-$ always occur with mutually opposite signs. The split fluxes $\mathbf{G}^+$ and $\mathbf{G}^-$ are so defined to help visualize them better.

This is the master equation, so to speak, of the present near-equilibrium flow method and schemes of different orders of accuracy are derived as approximations of this equation. Note that this equation embodies the important physical idea of kinetic flux-splitting, *i.e.*, it is *important* to interpret the flux terms in Eq. 3.2.1 the way they were introduced. To further congeal the important aspects of this method, a simple first order scheme is considered first. The complication arising out of the higher order accurate schemes are discussed thereafter. In that context, the behavior of the first order scheme is seen to be crucial; so while almost always higher order methods are used in computations, an understanding of the first order method is of paramount importance.

3.2.1 A First Order Scheme

To obtain a first order scheme, it is enough to assume that the velocity distribution, and therefore all other relevant quantities, are constant in the volume of a cell, and that they undergo discontinuous changes at the cell boundaries. Physically, this amounts to saying that the mean-free-path of the gas is of the order of the cell size‡. Considering cell $[x - \Delta x/2, x + \Delta x/2]$ with exchange of mass, momentum, and energy at $x - \Delta x/2$ and $x + \Delta x/2$, the resulting updating scheme for $\mathbf{F}$ in the cell is given by

$$\begin{aligned}\frac{d}{dt}\mathbf{F}(\mathbf{n}(x,t)) = -\frac{1}{\Delta x}\{&\mathbf{G}^+(\mathbf{n}^+(x,t)) - \mathbf{G}^-(\mathbf{n}^-(x+\Delta x,t)) \\ &- \mathbf{G}^+(\mathbf{n}^+(x-\Delta x,t)) + \mathbf{G}^-(\mathbf{n}^-(x,t))\}\end{aligned} \tag{3.2.2}$$

Using a first order time integrator, the forward Euler stepper, the above equation becomes

$$\begin{aligned}&\mathbf{F}(\mathbf{n}(x,t+\Delta t)) = \mathbf{F}(\mathbf{n}(x,t)) \\ &-\frac{\Delta t}{\Delta x}\left(\mathbf{G}^+(\mathbf{n}^+(x,t)) - \mathbf{G}^-(\mathbf{n}^-(x+\Delta x,t)) - \mathbf{G}^+(\mathbf{n}^+(x-\Delta x,t)) + \mathbf{G}^-(\mathbf{n}^-(x,t))\right)\end{aligned} \tag{3.2.3}$$

with Δt satisfying the Courant-Fredrich-Levy (CFL) stability criterion $v\Delta t/\Delta x \leq 1$, with v being the characteristic velocity of propagation of a small disturbance in the medium. The

‡ but the collision frequency is infinite in each of the cells.

scheme indicated in Eq. 3.2.3 has a simple physical interpretation in terms of the interactions of the centroids: The state of x at time $t + \Delta t$ is different from the state of x at time t by

1. the departure of particles from x due to a non-zero x-velocity, terms 1 and 4 in Eq. 3.2.3.
2. the arrival of particles with a positive x-velocity from $x - \Delta x$, term 3 in Eq. 3.2.3 and
3. the arrival of particles with a negative x-velocity from $x + \Delta x$, term 2 in Eq. 3.2.3.

The important difference from the usual lattice gas evolution[♯], however, is the fact that the arrival and departure of the particles is so as to simulate fluxes with purely equilibrium components (no viscous or heat conducting components). As a computational detail, since the primary dependent variables are $\mathbf{m}$, the evolution of $\mathbf{m}$ is given by

$$\mathbf{m}(x, t + \Delta t) = \mathbf{m}(x, t) - \frac{\Delta t}{\Delta x}[\mathbf{J_{Fm}}]^{-1} \left(\mathbf{G}^+(\mathbf{n}^+(x,t)) - \mathbf{G}^-(\mathbf{n}^-(x + \Delta x, t)) - \mathbf{G}^+(\mathbf{n}^+(x - \Delta x, t)) + \mathbf{G}^-(\mathbf{n}^-(x,t))\right) \tag{3.2.4}$$

where $\mathbf{J_{Fm}}$ is the Jacobian of the transformation from $\mathbf{F}$ to $\mathbf{m}$.

3.2.2 Viscosity of the First Order Scheme

It was mentioned before that the mean-free-path is of the order of the cell dimension: the method is therefore expected to have *viscosity.* Since the coefficient of viscosity is specific to each model, a qualitative procedure of how this coefficient of viscosity can be estimated is outlined here. Though the particle velocity distributions in the cells themselves are the equilibrium Maxwell-Boltzmann distributions, the distributions at the cell boundaries are not — they are a combination of the two different one-sided equilibrium distributions. At

♯ The dimension of $\mathbf{m}$, the vector of particle populations that is updated at each time step, here is $D + 2$ and not b, as for the usual lattice gas evolution.

the interface between cell j and $j+1$, indicated by $j+1/2$,

$$\mathbf{n}_a(j+\frac{1}{2}) = \mathbf{n}^+(j) \bigcup \mathbf{n}^-(j+1)\,. \tag{3.2.5}$$

The subscript a stands for actual, as opposed to equilibrium which is what is implied by no subscript. The $\mathbf{n}_a$ at $j+1/2$, defines a macroscopic state there, $\mathbf{F}(j+\frac{1}{2})$. Corresponding to that macrostate, there exists an equilibrium distribution $\mathbf{n}(j+1/2)$ and consequently an equilibrium flux $\mathbf{G}(j+\frac{1}{2})$, which can be written as

$$\mathbf{G}(j+\frac{1}{2}) = \mathbf{G}^+(\mathbf{n}^+(\mathbf{F}(j+\frac{1}{2}))) - \mathbf{G}^-(\mathbf{n}^-(\mathbf{F}(j+\frac{1}{2}))) \tag{3.2.6}$$

This is, however, not the actual flux at $j+1/2$. The actual flux at $j+1/2$, $\mathbf{G}_a(j+1/2)$ is given by

$$\mathbf{G}_a(j+\frac{1}{2}) = \mathbf{G}_a(\mathbf{n}_a(j+\frac{1}{2})) = \mathbf{G}^+(\mathbf{n}^+(j)) - \mathbf{G}^-(\mathbf{n}^-(j+1)) \tag{3.2.7}$$

where the actual (non-equilibrium) flux at $j+1/2$ has been expressed in terms of the equilibrium (one-sided) fluxes at j and $j+1$ The non-equilibrium part of the actual flux at $j+1/2$ is given by the difference of Eq. 3.2.7 and Eq. 3.2.6. After some manipulation, the non-equilibrium component of the actual flux at $j+1/2$, denoted by $\mathbf{G}_v(j+1/2)$ is given correct to first order by

$$\mathbf{G}_v(j+\frac{1}{2}) = -\frac{\Delta x}{2}\left[(\mathbf{J}_{\mathbf{G}^+\mathbf{m}} + \mathbf{J}_{\mathbf{G}^-\mathbf{m}})[\mathbf{J}_{\mathbf{Fm}}]^{-1}\frac{d\mathbf{F}}{dx}\right]_{j+\frac{1}{2}} \tag{3.2.8}$$

This non-equilibrium part of the actual flux can be written in the form

$$\mathbf{G}_v(x) = -\nu\frac{d\mathbf{F}}{dx} \qquad \text{with} \quad \nu = \frac{\Delta x}{2}\left[(\mathbf{J}_{\mathbf{G}^+\mathbf{m}} + \mathbf{J}_{\mathbf{G}^-\mathbf{m}})[\mathbf{J}_{\mathbf{Fm}}]^{-1}\right] \tag{3.2.9}$$

The *constitutive* relation above has a full 3x3 matrix of viscosity coefficients relating the flux of mass, momentum, and energy to the gradient of mass, momentum, and energy, but the important thing to note is the dependence of all the viscosity coefficients on the cell size in the first order scheme analyzed. Macrossan (1989), carries out such an argument for the special case of the flux of momentum depending on the gradient of momentum in

the context of a first order EFM applied to a perfect gas and arrives at a coefficient of viscosity which is again seen to be directly dependent on the cell size. Thus the equilibrium flow technique is expected to simulate the equilibrium flow exactly only in the limit of the coefficient of viscosity, as, *e.g.*, in Eq. 3.2.9, going to zero. This can be achieved either by letting the cell size go to zero (expensive) or by making the method increasingly higher order accurate in space, *i.e.*, make the coefficient of viscosity of the method depend only on higher powers of the cell size. The latter approach is pursued in the next section.

Before that, it is worth pointing that the equilibrium flow technique discussed here is a shock-capturing method: the coefficient of viscosity acts correctly and is appropriately modified implicitly in all situations, with no parameters to be tweaked.

3.2.3 Second Order Schemes

An extension of the above first order scheme to a higher order accuracy requires care. This is illustrated by Fig. 3.5.1, where a second order accuracy is achieved by averaging the individual flux terms in Eq. 3.2.1 symmetrically over adjacent neighbors. The pathological oscillatory behavior (seen in the Fig. 3.5.1) behind the shock is the quintessential feature of this method which renders it useless in computing flows with discontinuities (see below). It is interesting to note that the first order scheme does not develop oscillations* when steep gradients are encountered. The problem with the above second order scheme is that the second order accuracy was achieved by linear interpolation of the primary variables between the centroidal values. In so doing, the interpolated values at the cell boundaries — from the left and the right — develop spurious variations (non-monotonicites) when steep gradients are encountered and these non-physical variations grow, resulting in the typical oscillatory behavior (seen in Fig. 3.5.1). The correct way to develop a second order scheme is therefore to linearly interpolate the variables in such a manner as to preserve the

* The viscosity calculations of the previous subsection could perhaps be used to explain this.

first order monotonicities: this precludes the generation of the spurious variations at the cell boundaries when steep gradients are encountered. As discussed in the review article by Yee, 1989, this can be achieved by using some kind of a limiting procedure: imposing constraints on the gradients of the primary dependent variables gives rise to *slope limiter* schemes. Imposing constraints on the gradients of the fluxes themselves gives rise to *flux limiters*. Both, a slope limited second order scheme and a flux limited second order scheme are studied. The limiting procedure used in the two cases is the same, and is the popular *minmod* limiter.

The minmod limiter is best described as this binary operator:

$$\text{min\_mod}(p,q) = \begin{cases} 0 & \text{if } \text{sgn}(p) \neq \text{sgn}(q) \\ \min\{|p|,|q|\} & \text{if } \text{sgn}(p) = \text{sgn}(q) \end{cases} \tag{3.2.10}$$

where $\text{sgn}(p)$ is the sign of p and $|p|$ is the absolute value of p. In the present usage, p and q are the values of the slopes at the centroid of a cell — p being the backward slope and q the forward slope. The full minmod limiting procedure simply consists of applying the above binary operation to each of the cells at any given time step to obtain the slopes for any relevant quantity at each of the cell centroids.

In both the flux limiter and slope limiter schemes to be presented, the aim is to obtain second order accurate approximations for the four split-fluxes in Eq. 3.2.1. Time integration will be discussed in the next section.

- Flux Limiter: The split-fluxes are calculated at the centroids and then are linearly interpolated using the minmod limiter to estimate their values at the cell boundaries:

$$\mathbf{G}^+(x+\frac{\Delta x}{2},t) = \mathbf{G}^+(x,t) + \frac{1}{2}\text{min\_mod}\left(\Delta_{bck}\mathbf{G}^+(x,t), \Delta_{fwd}\mathbf{G}^+(x,t)\right) \tag{3.2.11}$$

$$\mathbf{G}^-(x+\frac{\Delta x}{2},t) = \mathbf{G}^-(x+\Delta x,t) - \frac{1}{2}\text{min\_mod}\left(\Delta_{bck}\mathbf{G}^-(x+\Delta x,t), \Delta_{fwd}\mathbf{G}^+(x+\Delta x,t)\right)$$

where $\mathbf{G}^+(x,t) = \mathbf{G}^+(\mathbf{n}^+(x,t))$, *etc.*, all consistent with the kinetic flux-splitting idea and $\Delta_{fwd}y(x,t) = y(x+\Delta x,t) - y(x,t)$, *etc.*

- Slope Limiter: The primary dependent variables $\mathbf{m}$ at the centroids are linearly interpolated using the minmod limiter to approximate their boundary values, at which values the split-fluxes are calculated.

$$\mathbf{m}(x+\frac{\Delta x}{2},t) = \mathbf{m}(x,t) + \frac{1}{2}\text{min\_mod}\left(\Delta_{bck}\mathbf{m}(x,t), \Delta_{fwd}\mathbf{m}(x,t)\right)$$

$$\mathbf{G}^+(x+\frac{\Delta x}{2},t) = \mathbf{G}^+(\mathbf{n}^+(x+\frac{\Delta x}{2},t)) \qquad (3.2.12)$$

$$\mathbf{G}^-(x+\frac{\Delta x}{2},t) = \mathbf{G}^-(\mathbf{n}^-(x+\frac{\Delta x}{2},t))$$

where the same notation as in Eq. 3.2.11 has been used.

3.2.4 Time Integration

If the above spatially second order schemes are to be used in an unsteady problem, it is important to make sure that the time integration is at least second order accurate, since otherwise, the time integration errors are likely to dominate the spatial errors. In fact, the time integration errors are directly coupled to the spatial errors, if the time stepping is determined by the CFL stability criterion. To simplify matters, a high degree of accuracy of the time integration is ensured by using fourth order Runge-Kutta with a time step well below the CFL stability limit. This is done for both the first order and second order spatially accurate schemes. Since the present interest lies in applying these schemes to unsteady problems, the high degree of accuracy of time integration does not go to waste: the computations can be continued *much* longer before the accumulated time errors become significant.

3.3 A Comparison of The First and Second Order Schemes

The accuracies of the first order and the two second order schemes as obtained in computations are compared by running a test problem with the nine-velocity gas. The time at which the methods are compared are such that the errors due to the time integration are negligible. The integral over the spatial domain of mass, momentum, and total energy is conserved to better than one part in a million in all the schemes. The order of accuracy of the method is estimated by looking at a global error measure E given by

$$E(t) = \int_{Domain} y(x,t;\Delta x) - \int_{Domain} y(x,t;\Delta x = 0)\,. \tag{3.3.1}$$

$y(x,t;\Delta x)$ is the solution obtained by a numerical scheme with a step size Δx for a problem, the exact solution for which is given by $y(x,t;\Delta x{=}0)$. Since the exact solution $y(x,t;\Delta x{=}0)$ is not known analytically, *Richardson's deferred approach to the limit*, Press *et al.* (1988), is used to estimate the exact value: a rational function extrapolation is used on a sequence of solutions with decreasing Δx to estimate the solution at $\Delta x{=}0$. The method is n^{th} order accurate if $E = O((\Delta x)^n)$.

The test problem is set up on a periodic domain (0,1) so that the effects of boundaries are eliminated. The initial condition on the periodic domain is a sinusoidal velocity distribution superimposed over a uniform state: $\rho(x,0) = \rho_0$, $e(x,0) = e_0$, $u(x,0) = u_0 + u_1 \sin(2\pi x)$. The time t at which the error analysis is done is chosen to be smaller than the time of formation of discontinuities, which is determined by the initial conditions. The quantity y in Eq. 3.3.1 used in the error analysis is the non-dimensional** kinetic energy $\frac{1}{2}\rho u^2$.

Fig. 3.3.1 shows the scaling of the global errors with the spatial discretization for the three different schemes discussed previously. The first order accuracy of the basic scheme and the second order accuracy of both the flux limited and slope limited schemes are clearly

** density, ρ, is non-dimensionalized by the average density over the domain and the velocity, u, by the unit speed, q in the model.

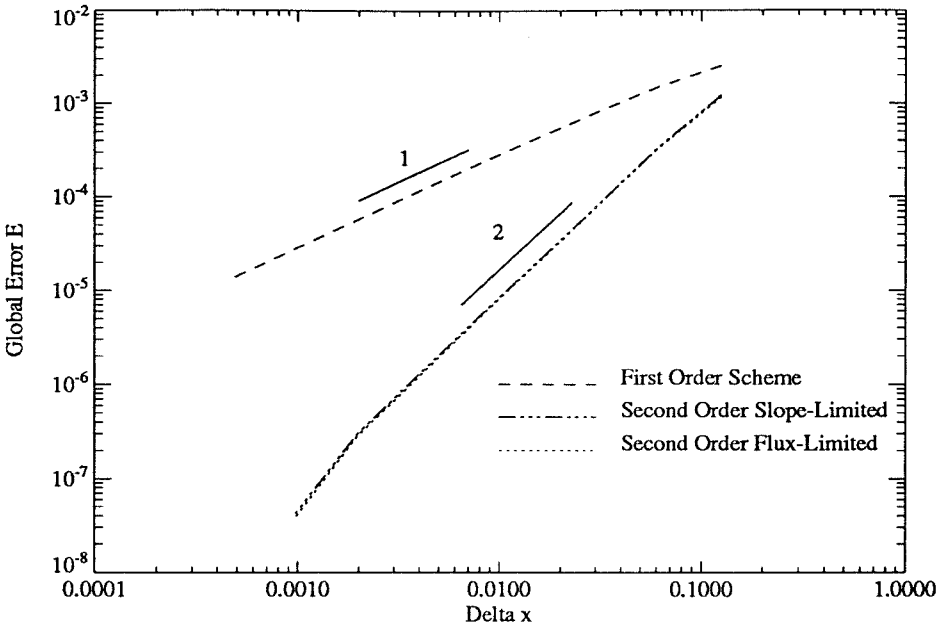

FIG. 3.3.1 Variation of the global error in kinetic energy with spatial discretization, at a particular time.

verified. The close correspondence between the flux limiter and slope limiter schemes, shows that neither of them has a clear advantage over the other.

In light of the previous discussion of the viscosity of these methods, the above test problem can be used to obtain a numerical estimate of the coefficient of viscosity.

Fig. 3.3.2 shows the decay with time of the initial kinetic energy in the problem discussed above, for both the first order method and a second order method. In this computation, an extremely coarse mesh was used — only 8 cells — to tile the domain (0,1) giving a $\Delta x = 0.125$. The important feature to note in the plot is the qualitative behavior of the kinetic energy: The oscillatory nature is a feature of the exact Euler solution and the decay of the amplitude is an effect of the viscosity of the method. The decay of the amplitude (given by the envelope) is approximated by an exponential and the rate of fall off is a measure of the viscosity of the method. The amplitude at a time t can thus be written as

$$y = y_\infty - (y_\infty - y_0)\exp(-\nu t)\,, \tag{3.3.2}$$

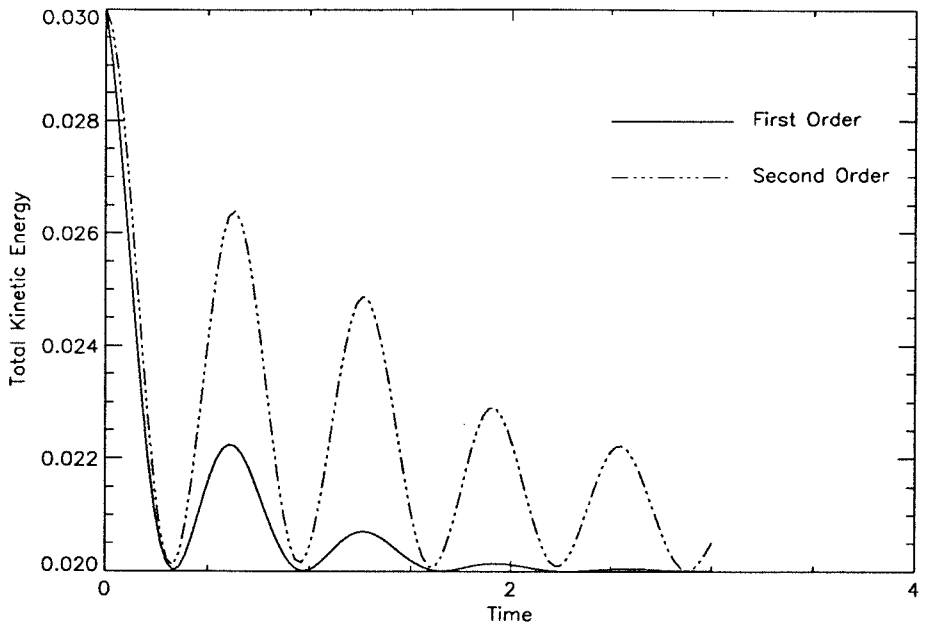

FIG. 3.3.2 The dissipation of kinetic energy as a manifestation of the viscosity of these methods

where y_0 is easily estimated by the phase at which the y is considered (corresponding to time t), y_∞ corresponds to final uniform state, after the perturbation has been dissipated, and ν is the effective viscosity coefficient.

$$\nu t = \log\left(\frac{y_0 - y_\infty}{y - y_\infty}\right) \tag{3.3.3}$$

By repeating the calculation on a finer mesh, the viscosity is seen to vary linearly with the cell size in the first order method and quadratically in the second order method. Thus the viscosity of these methods can be used to characterize the accuracy of these methods.

3.4 Comparison with Other Lattice Gas Methods

While at the outset, it may seem that the near-equilibrium flow techniques cannot be compared to the other prevalent schemes of computing lattice gas flows, it is rather clear from the discussions in this chapter and Sec. 5.5 that meaningful comparisons can in fact be made. Before that, it should be pointed out that the features of lattice gases which make them interesting and popular are preserved in the near-equilibrium flow schemes introduced:

- The interactions are local, and thus these methods are just as parallelizable as other lattice gas methods.
- Subject only to the CFL criterion, these schemes are robust with little unphysical behavior.

As compared to the full lattice gas simulations, the relative merits of the near equilibrium flow technique are

- Since it is not a stochastic process, simulations using this technique are relatively noise-free.
- The need for an exclusion principle to ease computation is obviated. Thus the classically unphysical effects of an exclusion principle are eliminated.
- Schemes to enhance collisions† (Rothman 1989) are also obviated since the technique is the *infinite* collision frequency limit of the lattice (discrete-velocity) gas flow.
- Spurious conservations, as of staggered momenta (Kadanoff, 1988) are not expected in this mode of computation.

---

† which in most cases are highly unsatisfactory in that they violate some basic conservation leading to a loss of *universality of equilibrium distributions!.*

- It is speculated that simulations of flows with a much higher Reynolds number are possible with this method, given the same computer resources. The quantitative interpretation of the flows will perhaps be complicated by the nature (Eq. 3.2.9) of the viscosity coefficient.
- If a larger number of velocites are to be included in the lattice gas model, while the full lattice gas simulations are likely to run into problems of too big a neighborhood, and/or too large a look-up table, the present method would not be affected much, but for an increased computation in each cell.
- Extension to 3-D computations poses no new problems[‡].

The disadvantages of the near-equilibrium flow technique compared to the full lattice gas simulations are, of course,

- Aspects of long-time velocity auto-correlations and many-body correlations cannot be studied, since they are all thrown away by the Boltzmann approximation.
- By using floating point numbers, it lacks a very attractive feature of CA. This may preclude implementions of this technique on the special CA computers being developed.
- One has to speak of the accuracy of the method unlike in the CA universe.

To put it in the context of the Lattice Boltzmann Equation (LBE) approach, the near-equilibrium flow technique is the infinite collision limit of the *full* LBE. Computing collisions which constitute the right hand side of the LBE is a computationally intensive task (Inamuro & Sturtevant 1990). The present method does not deal with collisions, since an infinite collision rate is implicit in the formulation. The prevalent schemes for LBE, however, use

‡ Note that only the scheme of implementing a given model is being discussed, not a scheme for arriving at new models based on the present technique.

a simplified model for the collisions. The most popular model is the single time relaxation model, Succi *et al.* (1991), like the Bhatnagar-Gross-Krook (BGK) collision model for the *actual* Boltzmann equations, but with much severe restrictions: while the deviations from equilibrium in the BGK model are deviations from the *local* equilibrium, the deviations in the LBE context are from *one global* equilibrium! This is clearly untenable in a compressible flow situation. A further price to be paid in such a simplification is not knowing when the simplified relaxation model of collision becomes insufficient. This is evidenced even in the studies of the BGK approximation of the actual Boltzmann equations (Cercignani 1988). Since the near-equilibrium flow techniques are based on the idea of local thermodynamic equilibrium, no such problems arise in their usage.

3.5 The Method from the Point of View of Euler Equations

Consider a set of conservation[♯] equations in one space dimension and time

$$\frac{\partial \mathbf{F}(\mathbf{n})}{\partial t} + \frac{\partial \mathbf{G}(\mathbf{n})}{\partial x} = 0 \,. \tag{3.5.1}$$

If $\mathbf{F}$ is the vector of mass, momentum, and energy, and if $\mathbf{G}$ is the flux of $\mathbf{F}$, then Eq. 3.5.1 are the hydrodynamic flow equations. Let $\mathbf{n}$ in Eq. 3.5.1 be the molecular velocity distribution function; if $\mathbf{n}$ is the equilibrium Maxwell-Boltzmann distribution, then Eq. 3.5.1 are the Euler equations. The structure of $\mathbf{F}(\mathbf{n})$ and $\mathbf{G}(\mathbf{n})$ are particular to the underlying molecular model. If the underlying model is that of an ideal gas — a dilute gas of hard sphere particles with a continuous velocity space extending from $-\infty$ to $+\infty$ — the resulting form of Eq. 3.5.1 is referred to as the *actual* Euler equations. If, on the other hand, a simplified molecular model is used, the resulting Eq. 3.5.1 is referred to as the *model* Euler equations. These model Euler equations (see next chapter) have the same kind of non-linearity as the actual Euler equations — non-linear convection. Consequently, a non-linear steepening of

[♯] The integral of $\mathbf{F}(\mathbf{n})$ over the domain is conserved with time, provided the domain is isolated.

initially smooth profiles of the conserved quantities $\mathbf{F(n)}$ is to be expected with the model Euler equations. Singularities are expected to appear in finite times for all but the most degenerate initial conditions. The same issues then arise in numerically solving the model Euler equations, as in solving the actual Euler equations: the ability or inability of the numerical methods to handle steep gradients and issues of artificial *vs.* numerical viscosity. This is crucial of course if the evolution is to be followed beyond the time of formation of discontinuities.

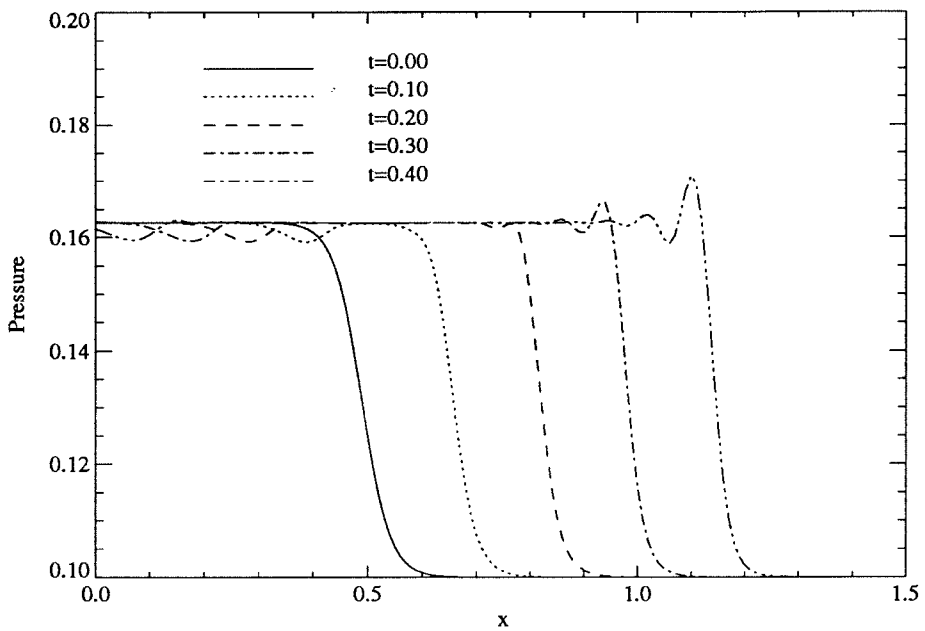

FIG. 3.5.1 Time evolution of an initial monotonic tanh pressure profile under the model Euler equations using a centered space fourth order RK algorithm. The post-shock oscillations are numerical.

Viewing Eq. 3.5.1 as a set of partial differential equations with no reference to the underlying model, a first and rather popular attempt would be to use the centered space and fourth order Runge-Kutta time stepping procedure. Fig. 3.5.1 shows the time sequence of the x-profile of pressure using such a numerical solver to solve the model Euler equations Eq. 3.5.1 of the nine-velocity model (see next chapter). The initial condition is smooth, but non-linear convection steepens the wave. This numerical procedure is best analysed by

considering a simple quasi-linear convection equation, the inviscid Burgers' equation. Lax (1986) shows that central-space differencing is equivalent to introducing a dispersive term into the original equation. This causes a transfer of energy into the higher wave-number components, the wave-number scaling with the mesh width. Fig. 3.5.1 seems to reveal the same sort of behavior in the present context, though the system now consists of three partial differential equations and of a considerably more complex form. It is perhaps interesting to note a couple of other things in this context:

- John von Neumann in his innovative efforts at constructing simplified molecular models to compute hydrodynamics, Neumann (1944), used a non-linear spring-mass chain to study shocks in an inviscid and non-heat conducting gas. Numerical solutions of this model resulted in post-shock oscillations of the same nature as seen in Fig. 3.5.1. von Neumann conjectured that these oscillations can be interpreted from the gas dynamic point of view as thermal energy produced by the irreversible nature of the shock wave.
- The centered space differencing of the inviscid Burgers' equation which introduces dispersive effects, causes the numerical solutions to look much like the solutions of the KdV equation. The post-shock oscillations in ?? seem very similar to the breakdown of the initial profile into a series of solitons in the case of the KdV equation.

The behavior of the oscillations are of no concern in the present context and need to be eliminated. Based on the particle velocities in the x-direction, the flux term in Eq. 3.5.1 may be split as

$$\frac{\partial \mathbf{F(n)}}{\partial t} + \frac{\partial \mathbf{G}^{+}(\mathbf{n}^{+})}{\partial x} - \frac{\partial \mathbf{G}^{-}(\mathbf{n}^{-})}{\partial x} = 0 \qquad (3.5.2)$$

Using the ideas of kinetic flux-splitting, it could perhaps be argued that the stable differencing for the flux terms should follow the simple rule '*backward difference the forward fluxes*

$\mathbf{G}^+$ *and forward difference the backward fluxes* $\mathbf{G}^-$.' Using the corresponding first order differences, Eq. 3.5.2 becomes

$$\frac{\partial \mathbf{F}(\mathbf{n})}{\partial t} + \frac{\mathbf{G}^+(\mathbf{n}^+(x,t)) - \mathbf{G}^+(\mathbf{n}^+(x-\Delta x,t))}{\Delta x} - \frac{\mathbf{G}^-(\mathbf{n}^-(x+\Delta x,t)) - \mathbf{G}^-(\mathbf{n}^-(x,t))}{\Delta x} = 0 \tag{3.5.3}$$

This equation is seen to be the same as Eq. 3.2.3. Eq. 3.5.3 can also be thought of as resulting from upwind differencing the (positive and negative components) of the flux, based on the particle velocites. Ideas from total variation diminition (TVD) schemes used in the context of shock-capturing techniques (Yee 1989) for Euler equations can perhaps be used to obtain higher order schemes and these would presumably look like the second order schemes of Sec. 3.2.3

CHAPTER 4

The Euler Limit of Discrete-Velocity Gas Flows

The solutions computed using the near-equilibrium flow technique, introduced in the previous chapter, are effectively approximations to the solutions of the model Euler equations (specific to the model used). In this chapter, the model Euler equations are derived, the behavior of their characteristics examined and the solutions of these equations, as obtained by the flux-limited second order near-equilibrium flow technique of chapter 3, for some typical problems analyzed. While the methodology is general, specific computations are done using the nine-velocity model.

4.1 The Model Euler Equations

An inviscid and non-heat conducting flow of a discrete-velocity gas is realized, as in any other fluid, by prescribing *local thermodynamic equilibrium* at every point in the flow. Then, such a flow is represented by the Boltzmann equations Eq. 5.2.2 in conjunction with the equations Eq. 2.2.9 which prescribe thermodynamic equilibrium and of course, the appropriate boundary conditions. Noting that with b particle velocities allowed in a model, there are $b-D-2$ equilibrium equations and at the same time $D+2$ macroscopic variables (mass, momentum, and energy), the equilibrium flow must be describable in terms of $D+2$ primary variables. To this end, consider the $D+2$ moments of the Boltzmann equations Eq. 5.2.2 corresponding to mass, momentum, and energy:

$$\begin{gathered}\sum_{i=1}^{b} f_j(\mathbf{c_i}) L_i n_i = 0, \qquad j = 1, D+2 \\ f_1(\mathbf{c_i}) = 1, \quad f_{2,D+1}(\mathbf{c_i}) = \mathbf{c_i}, \quad f_{D+2}(\mathbf{c_i}) = |\mathbf{c_i}|^2\end{gathered} \tag{4.1.1}$$

The right-hand side of Eq. 4.1.1 is identically zero because mass, momentum, and energy are collisional invariants. The above are $D+2$ partial differential equations in b dependent variables. The equilibrium equations Eq. 2.2.9 may now be used to eliminate $b-D-2$ of the variables to arrive at the $D+2$ partial differential equations, now only in $D+2$ variables, the model Euler equations, symbolically

$$E_j n_i(n_k) = 0, \qquad i = 1, b \quad j,k = 1, D+2\,. \tag{4.1.2}$$

Rewriting the above equations in conservation form,

$$\frac{\partial \boldsymbol{\Phi}}{\partial t} + \frac{\partial \mathbf{f}(\boldsymbol{\Phi})}{\partial \mathbf{x}} = 0 \tag{4.1.3}$$

where $\boldsymbol{\Phi} = (\rho, \rho\mathbf{u}, \rho e_t)$ and $\mathbf{f}(\boldsymbol{\Phi})$ is the flux of $\boldsymbol{\Phi}$. The structure of the flux vector $\mathbf{f}(\boldsymbol{\Phi})$ in the case of discrete-velocity gases is much more complicated than in a perfect gas. In fact $\mathbf{f}(\boldsymbol{\Phi})$ is usually not expressible* *exactly* in a closed form. Therefore, to circumvent this, the hydrodynamic vector $\boldsymbol{\Phi}$ is expressed in terms of $\mathbf{n}$, some $D+2$ particle populations, as $\boldsymbol{\Phi} = \mathbf{F}(\mathbf{n})$, in which case Eq. 4.1.3 becomes

$$\frac{\partial \mathbf{F}(\mathbf{n})}{\partial t} + \frac{\partial \mathbf{G}(\mathbf{n})}{\partial \mathbf{x}} = 0\,, \tag{4.1.4}$$

where $\mathbf{G}(\mathbf{n})$ is the flux $\mathbf{f}(\boldsymbol{\Phi})$ reexpressed in terms of $\mathbf{n}$. $\mathbf{F}(\mathbf{n})$ and $\mathbf{G}(\mathbf{n})$ are both explicitly known as the appropriate moments of the distribution function**, and are algebraic forms. All discussion from here on is confined to flows in one spatial dimension, and when the nine-velocity model is used, the flow is along one of the slow moving particle directions†. This makes the analysis simpler at places and since the aim of the study is to indicate the methodology, the case chosen is as good as any. Extension to multiple space dimensions or analysis of flows directed along any other one direction is straight forward. As a notational clarification, all dependent variables used in this chapter are in their non-dimensional form: densities refer to the number of particles at a point or in a cell, velocities are non-dimensionalized by q, the unit of speed in the model and energies by q^2.

---

* Related to the equation of state and Galilean non-invariance of discrete-velocity gas models.

** the full equilibrium distribution function is expressible in terms of $\mathbf{n}$.

† except in one of the subsections where the possibility of supersonic flow is investigated.

For one-dimensional unsteady flow, the model Euler equations Eq. 4.1.4 can be put into a more convenient form:

$$A_{ij}\frac{\partial n_j}{\partial t} + a_{ij}\frac{\partial n_j}{\partial x} = 0, \qquad i,j = 1,\ldots,3\,. \tag{4.1.5}$$

$\mathbf{A} = \mathbf{J}_{\mathbf{\Phi n}}$ is the Jacobian of the transformation from $\mathbf{\Phi}$ to $\mathbf{n}$, and similarly $\mathbf{a} = \mathbf{J}_{\mathbf{f(\Phi)n}}$. Note that $\mathbf{A}$ and $\mathbf{a}$, both depend on $\mathbf{n}$ and therefore Eq. 4.1.5 is a system of nonlinear equations.

4.2 Characteristics of the Model Euler Equations

A curve $C : (x = X(\eta); t = T(\eta))$ in the $x - t$ plane, is a characteristic direction (velocity) of the system Eq. 4.1.5 at (x,t) or equivalently η if

$$|A_{ij} - \frac{\beta}{\alpha}a_{ij}| = 0 \qquad \text{where } \alpha = X'(\eta) \text{ and } \quad \beta = T'(\eta)\,. \tag{4.2.1}$$

Letting $\beta/\alpha = \omega$ be the new variable, Eq. 4.2.1 is a cubic equation in ω and can be solved for the three characteristic velocities $(\omega_o, \omega_+, \omega_-)$ at the point $\mathbf{n}$ corresponding to $\mathbf{\Phi} = (\rho, u, e)$. In the Boltzmann limit, which is being used, the density factors out and the characteristic speeds depend only on the specific energy e, and the flow velocity u. Physically, the three characteristic speeds correspond to the absolute speeds of propagation of a disturbance made in the discrete-velocity fluid in thermodynamic equilibrium at (ρ, u, e)‡. For reference, the above three characteristic velocities for the perfect gas are u, $u + a$ and $u - a$,

‡ If the full kinetic (Boltzmann) equations of the model are considered, there is a hierarchy of waves of different orders. In such a hierarchy, the lowest order waves correspond to the *hydrodynamic* modes. The characteristic speeds $((\omega_o, \omega_+, \omega_-)$ being discussed above are of the *lowest order* waves. The higher order waves correspond to kinetic modes. The first signals about the disturbance *are* carried by the kinetic modes — the very first ones corresponding to the *particle velocities*, which form the characteristics of the *highest* order waves and so on. These kinetic modes, however, carry very little information about the disturbance: the higher the order, the lesser its importance. The bulk of the information about the disturbance is carried by the hydrodynamic modes, and thus are of primary importance. To clarify this, consider the Boltzmann equations,

$$L_i n_i = \frac{1}{Kn}Q_i(n_j, n_j), \quad \text{where} \quad L_i = \frac{\partial}{\partial t} + \mathbf{c}_i\frac{\partial}{\partial \mathbf{x}}, \quad \text{and} \quad i,j = 1,\ldots,b.$$

Kn, the Knudsen number is a measure of non-equilibrium: if $Kn = \infty$, only the left-hand side is significant, and the equations represent free-molecular flow, and if $Kn = 0$, the streaming of the particles is unimportant and continuum flow is recovered. Next, consider a *small* disturbance $\epsilon\mathbf{n}'$ about a fixed thermodynamic equilibrium state $\mathbf{n}^0$:

$$\mathbf{n} = \mathbf{n}^0 + \epsilon\mathbf{n}'.$$

$$\mathbf{Q}(\mathbf{n},\mathbf{n}) = 2\epsilon\mathbf{Q}(\mathbf{n}^0,\mathbf{n}') + O(\epsilon^2) \quad \text{since} \quad \mathbf{Q}(\mathbf{n}^0,\mathbf{n}^0) = 0$$

where $a = \sqrt{\left(\frac{\partial p}{\partial \rho}\right)_s} = \sqrt{\gamma RT}$. Thanks to the Galilean non-invariance of discrete-velocity gases, the additivity property of $u \pm a$ is lost and the three characteristic velocities are more general functions of both u and e. It is interesting to note that, performing the same procedure with the velocity discretization corresponding to the FHP model, there are only two characteristic velocities, whereas compressible fluid dynamics demands three. The reason for this is absence of temperature as an independent variable in the FHP discretization, resulting from the allowance of only one particle speed[♯].

Then correct to $O(\epsilon)$, the evolution of the disturbance is

$$\frac{Kn}{2} L_i n_i' = Q_i(n_j^0, n_j'), \quad i,j = 1,\ldots,b.$$

Rewritten in a more convenient form, they appear as

$$P_{ij} n_j' = 0, \quad \text{where} \quad P_{ij} = \frac{Kn}{2} L_i - Q_i(n_j^0, .), \quad i,j = 1,\ldots,b.$$

This is a system of linear equations — the coefficients are either linear operators depending on the particle velocities, or constants depending on the base equilibrium about which the disturbance is imposed. Therefore, by algebraic elimination (Cramer's rule), the system can be collapsed into a single wave equation:

$$Det(\mathbf{P})\phi = 0,$$

where ϕ is any n_i or any linear combination of n_i, and $Det(\mathbf{P})$ is the determinant of $\mathbf{P}$. Since any velocity moment of n_i is a linear combination of n_i, the above equation holds for the hydrodynamic variables (ρ, e, u) too. The wave operator $Det(\mathbf{P})$ has the form, as it results from an application of Cramer's rule to the linear system,

$$Det(\mathbf{P})\phi = \sum_3^b Kn^{k-3} W_k \phi = 0,$$

where W_k is a hyperbolic wave operator of the k^{th} order. This represents an hierarchy of waves (Whitham 1959; Broadwell 1964a; Nadiga *et al.* 1989). The absence of wave operators of order 0, 1, and 2, *i.e.*, W_0, W_1, and W_2 is due to the structure in the collision operator Q(n,n) resulting from the conservation of mass, momentum and energy in each of the collisions. Characteristic speeds of W_b, the highest order waves, are the particle speeds, and the characteristic speeds of W_3, the lowest order waves, are the hydrodynamic characteristic velocities given by $(\omega_0, \omega_+, \omega_-)$. The relative importance of the different order waves is brought out by the exponent of Kn multiplying them. For continuum flow, with $Kn << 1$, Kn^2 is negligibly small and only W_3 is important. While the higher order waves decay exponentially fast, the effect of the higher order waves on the lowest order waves is to make them diffusive to $O(Kn)$, dispersive to $O(Kn^2)$, *etc.*, (Whitham 1974).

♯ $e_t = e + \frac{u^2}{2}$ is thus conserved.

4.2.1 Characteristic Speeds in the Nine-Velocity Model

The matrices **A** and **a** in Eq. 4.1.5 for the nine-velocity model with flow along particle direction 1 (see Fig. 1.2.3), with $\mathbf{n} = (n_0, n_1, n_5)$ are given below.

$$\mathbf{A} = \begin{pmatrix} 1 - \frac{2\sqrt{n_1 n_5}(n_1+n_5)}{{n_0}^2} & \frac{n_0\sqrt{n_1}+n_0\sqrt{n_5}+3n_1\sqrt{n_5}+{n_5}^{\frac{3}{2}}}{n_0\sqrt{n_1}} & \frac{n_0\sqrt{n_1}+{n_1}^{\frac{3}{2}}+n_0\sqrt{n_5}+3\sqrt{n_1}n_5}{n_0\sqrt{n_5}} \\ \frac{-2\sqrt{n_1 n_5}(n_1-n_5)}{{n_0}^2} & 1 + \frac{3\sqrt{n_1 n_5}}{n_0} - \frac{{n_5}^{\frac{3}{2}}}{n_0\sqrt{n_1}} & -1 + \frac{{n_1}^{\frac{3}{2}}}{n_0\sqrt{n_5}} - \frac{3\sqrt{n_1 n_5}}{n_0} \\ \frac{-2\sqrt{n_1 n_5}(n_1+n_5)}{{n_0}^2} & \frac{n_0\sqrt{n_1}+n_0\sqrt{n_5}+6n_1\sqrt{n_5}+2{n_5}^{\frac{3}{2}}}{2n_0\sqrt{n_1}} & \frac{n_0\sqrt{n_1}+2{n_1}^{\frac{3}{2}}+n_0\sqrt{n_5}+6\sqrt{n_1}n_5}{2n_0\sqrt{n_5}} \end{pmatrix} \tag{4.2.2}$$

$$\mathbf{a} = \begin{pmatrix} \frac{-2\sqrt{n_1 n_5}(n_1-n_5)}{{n_0}^2} & 1 + \frac{3\sqrt{n_1 n_5}}{n_0} - \frac{{n_5}^{\frac{3}{2}}}{n_0\sqrt{n_1}} & -1 + \frac{{n_1}^{\frac{3}{2}}}{n_0\sqrt{n_5}} - \frac{3\sqrt{n_1 n_5}}{n_0} \\ \frac{-2\sqrt{n_1 n_5}(n_1+n_5)}{{n_0}^2} & \frac{n_0\sqrt{n_1}+3n_1\sqrt{n_5}+{n_5}^{\frac{3}{2}}}{n_0\sqrt{n_1}} & \frac{{n_1}^{\frac{3}{2}}+n_0\sqrt{n_5}+3\sqrt{n_1}n_5}{n_0\sqrt{n_5}} \\ \frac{-2\sqrt{n_1 n_5}(n_1-n_5)}{{n_0}^2} & \frac{1}{2} + \frac{3\sqrt{n_1 n_5}}{n_0} - \frac{{n_5}^{\frac{3}{2}}}{n_0\sqrt{n_1}} & -\frac{1}{2} + \frac{{n_1}^{\frac{3}{2}}}{n_0\sqrt{n_5}} - \frac{3\sqrt{n_1 n_5}}{n_0} \end{pmatrix}$$

The above **A** and **a** matrices were used to write the characteristic polynomial, the left side of Eq. 4.2.1 explicitly using a symbolic manipulator. But with the coefficients of the polynomial being too bulky to be of any practical use, the characteristic speeds were computed as numerical solutions of the characteristic equation.

This is presented in Fig. 4.2.1 as a variation with e of the three characteristic speeds $(\omega_0, \omega_+, \omega_-)$ at a specified flow velocity; three different velocities are considered. ω_+ is the velocity of propagation of the upstream disturbance, ω_-, that of the downstream disturbance, and ω_0 is the third characteristic speed corresponding to the flow velocity u in a perfect gas. Fixing with the mean flow, it is seen that the characteristic velocities in the upstream and downstream directions are in general different (same when the mean flow is 0). Another interesting observation is the way ω_- behaves at low values of specific internal energy: at a given flow velocity u, ω_- seems to approach $\omega_- = 0$ with a zero slope. This is verified to be the case by calculating the above variation of ω_- with e for a whole range of values of u. From this it follows, that at no combinations of u, the flow velocity and e, the specific energy, do all the three characteristic velocities have the same sign. The implication

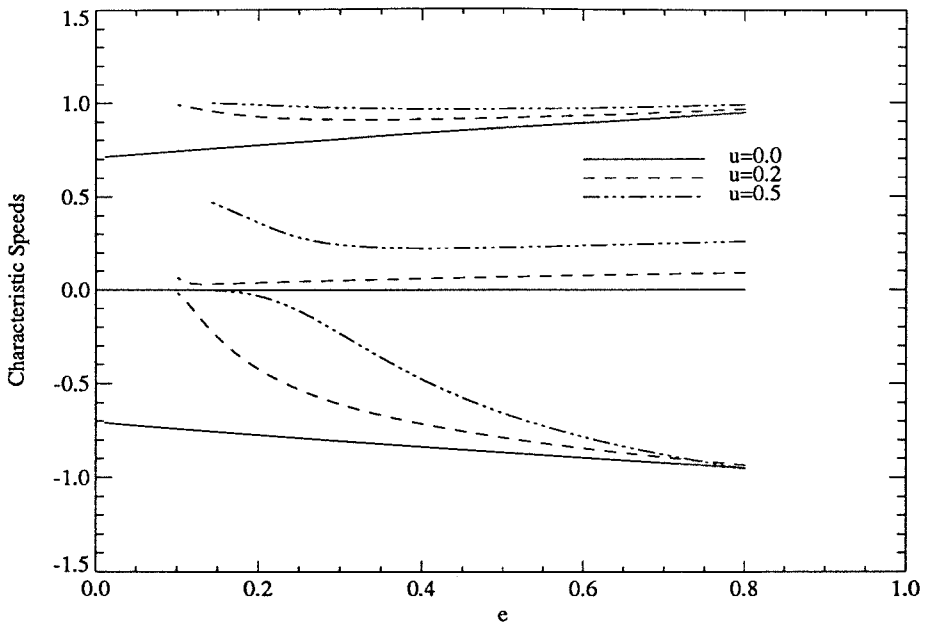

FIG. 4.2.1 The variation of the three characteristic speeds with specific energy at different flow velocities. The upper three curves correspond to ω_+, the fast characteristic speed in the flow direction; the lower three to ω_-, speeds of the backward running characteristic and the middle three to ω_0

of this is the *impossibility* of supersonic flow — the disturbances are never *all* swept downstream — in the slow moving particle direction. To investigate whether supersonic flow is possible in any direction at all in the nine-velocity model, we conjecture that it is sufficient to investigate the flow along one of the fast moving particle directions. To do this, the **A** and the **a** matrices need to be recalculated appropriately. For flow along particle direction 2 (see Fig. 1.2.3, with $\mathbf{n} = (n_0, n_2, n_6)$, the **A** and **a** matrices are given by

$$\mathbf{A} = \begin{pmatrix} \frac{\sqrt{n_0}+\sqrt{n_2}+\sqrt{n_6}}{\sqrt{n_0}} & \frac{\sqrt{n_0}+\sqrt{n_2}+\sqrt{n_6}}{\sqrt{n_2}} & \frac{\sqrt{n_0}+\sqrt{n_2}+\sqrt{n_6}}{\sqrt{n_6}} \\ \frac{\sqrt{2n_2}-\sqrt{2n_6}}{2\sqrt{n_0}} & \sqrt{2}\left(1+\frac{\sqrt{n_0}}{2\sqrt{n_2}}\right) & \sqrt{2}\left(-1-\frac{\sqrt{n_0}}{2\sqrt{n_6}}\right) \\ \frac{\sqrt{n_2}+\sqrt{n_6}}{2\sqrt{n_0}} & 1+\frac{\sqrt{n_0}}{2\sqrt{n_2}}+\frac{\sqrt{n_6}}{\sqrt{n_2}} & 1+\frac{\sqrt{n_0}}{2\sqrt{n_6}}+\frac{\sqrt{n_2}}{\sqrt{n_6}} \end{pmatrix}$$

(4.2.3)

$$\mathbf{a} = \begin{pmatrix} \frac{\sqrt{2n_2}-\sqrt{2n_6}}{2\sqrt{n_0}} & \sqrt{2}\left(1+\frac{\sqrt{n_0}}{2\sqrt{n_2}}\right) & \sqrt{2}\left(-1-\frac{\sqrt{n_0}}{2\sqrt{n_6}}\right) \\ \frac{\sqrt{n_2}+\sqrt{n_6}}{2\sqrt{n_0}} & 2+\frac{\sqrt{n_0}}{2\sqrt{n_2}} & 2+\frac{\sqrt{n_0}}{2\sqrt{n_6}} \\ \frac{\sqrt{n_2}-\sqrt{n_6}}{2\sqrt{2n_0}} & \sqrt{2}+\frac{\sqrt{n_0}}{2\sqrt{2n_2}} & -\sqrt{2}-\frac{\sqrt{n_0}}{2\sqrt{2n_6}} \end{pmatrix}$$

The full set of calculations is repeated with the above matrices and the variation of the three characteristic speeds with e at given values of flow velocities u, now along the diagonal is shown in Fig. 4.2.2. Similar calculations of the characteristic speeds at other possible combinations* of e and u reveal that the three characteristic velocities are never of the same sign. From the above calculations, it may be concluded(?) that it is *impossible* to establish a *supersonic* flow in the nine velocity model.

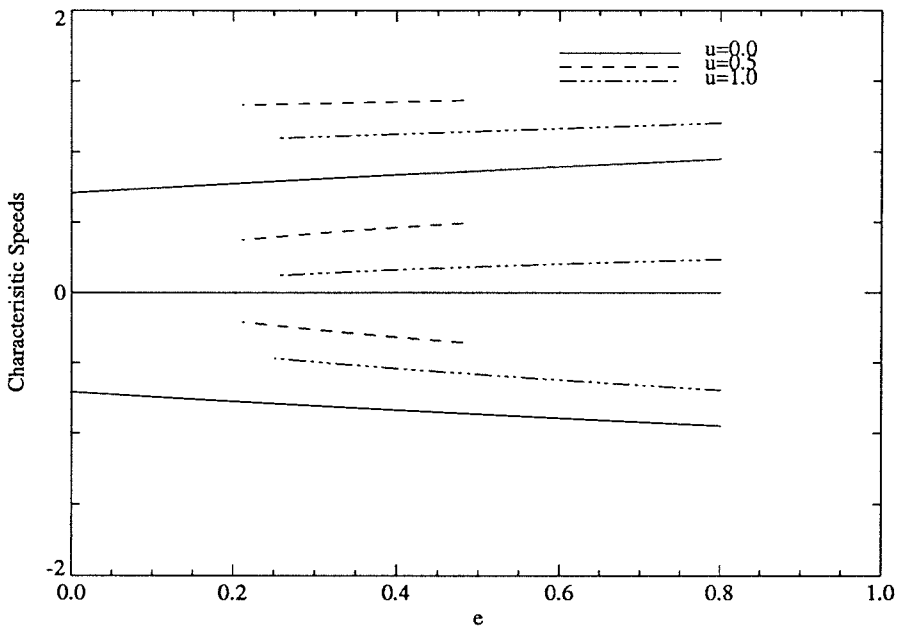

FIG. 4.2.2 A similar plot of the variation of the three characteristic speeds with the flow along a fast moving particle direction.

As a consequence of this,

- No stationary shock waves are possible in the nine-velocity model.
- No moving shock exists in the model which generates supersonic flow behind it.

---

* $e + \frac{u^2}{2} \leq 1.0$

4.3 Mach Number in Discrete-Velocity Gases

At this point, it is worthwhile to digress momentarily to look at the concept of Mach number in the context of discrete-velocity gases. In a continuum-velocity gas the characteristic velocities are u and $u \pm a$. Therefore, in the frame of the moving fluid, the disturbances propagate away symmetrically with speeds a in the upstream and downstream directions, and the Mach number is defined as the ratio of the flow velocity and a. Equivalently, a Galilean transformation of the system, into one in which the fluid is stationary leaves the thermodynamics invariant: a is the same in the two cases. There is, thus, a unique (isentropic) speed of sound to which the fluid velocities can be referred, and hence the Mach number. The problem with the discrete-velocity gas is the absence of such a symmetry: in the frame of the moving fluid, the upstream and downstream propagation speeds of a disturbance are not equal, and they depend on the fluid velocity itself. There isn't one unique speed of sound to which the flow velocities can be referred, and hence, the concept of a Mach number is not a natural one in the context of discrete-velocity gases. Having noted that, a *pseudo*-Mach number may be defined in two different ways:

- Considering the upstream propagation of disturbances,

$$M^{+} = \frac{u}{\omega_{+} - u}. \tag{4.3.1}$$

- Considering the downstream propagation of disturbances,

$$M^{-} = \frac{u}{u - \omega_{-}}. \tag{4.3.2}$$

The above two definitions reduce to $M = u/a$ for a perfect gas. While neither one of the above two definitions is sufficient on its own, the following shows that they could be used appropriately to get a qualitative picture.

- Considering a 1-D steady flow along a slow particle direction, $\omega_+ \leq 1.0$. Therefore, $M^+ > 1.0$ for $u > 0.5$, but it was shown in section 4.2.1 that the flow can never be supersonic. From the calculations in that section, it was also seen that $\omega_- \leq 0$. Using it in Eq. 4.3.2, $M^- \leq 1.0$ always, which reflects correctly that the flow can never go supersonic. So for steady flows, the Mach number is better defined by M^-.

- Consider a C_+ wave moving with a velocity U into an uniform region (ρ, u, e), where the characteristic velocities are (ω_0, ω_+, ω_-). The consideration to decide if the disturbance is supersonic or if it is subsonic with respect to the upstream is the relative magnitude of U and ω_+. Let $U > \omega_+$. Then, from its definition, $M^+ > 1$, and thus it correctly indicates that the disturbance is supersonic with respect to the upstream. So also for $U < \omega_-$. Therefore, for waves, the qualitatively correct definition of the wave Mach number is given by M^+.

As an aside, from above, it may be noted that the impossibility of setting up a supersonic flow in the nine velocity gas does not translate to being unable to have supersonic wave Mach numbers — a direct consequence of the Galilean non-invariance. Notions that shock waves cannot be studied with discrete velocity gases because they involve high Mach numbers is ill-founded because the Mach numbers involved are the shock Mach numbers and the flow velocities involved can still be small.

4.4 Riemann Invariants in Discrete-Velocity Gases

Along the characteristic directions in the $x - t$ plane, the partial differential equations, presently the Euler equations Eq. 4.1.5, become ordinary differential equations. In the case of perfect gases, these ordinary differential equations are integrable and they give rise to the Riemann invariants. In the general case of the characteristic velocities reducing the partial differential equations to odes, it would not be surprising if the odes are not integrable and this might very well be the case with discrete-velocity gases. Thus there may not be any *invariants* of the flow as such. The presence of invariants, if any, may in fact be used to a thermodynamic end, as in a perfect gas, where the invariant which propagates with the characteristic velocity u, may be used to define *entropy*, *i.e.*, the invariant identified to propagate with the fluid velocity would also satisfy the usual thermodynamic properties associated with entropy, Whitham (1974). Since such a Riemann invariant has not been identified in the nine-velocity gas, this approach to define entropy cannot be examined.

4.5 The Linear Wave Equation Limit

The first of a few unsteady one-dimensional equilibrium discrete-velocity gas flows examined is the limit in which a simple** linear wave behavior is recovered. The computation technique used in all of the example calculations is the flux-limited, second order, equilibrium flow technique discussed in the previous chapter. An initial hyperbolic secant disturbance is established on a periodic (0,1) domain, and its time evolution is studied. Throughout the computation, mass, momentum, and energy are all conserved to better than one part in a million. The disturbance is chosen to be so small that the nonlinearity is negligible.

** non-dispersive

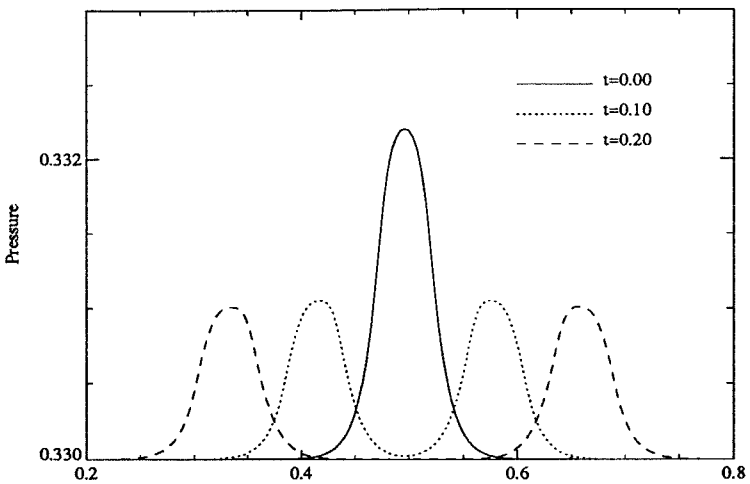

FIG. 4.5.1 Recovery of the linear wave equation: An initial pressure pulse splits into a C_+ and a C_- disturbance. The initial pulse is the linear superposition of the two pulses.

Fig. 4.5.1 shows the evolution of pressure with time. The behavior of the other disturbances, density, specific energy, and velocity is similar. The initial pressure disturbance is set up in a quiescent medium by a variation in the density. Because of the linearity, the initial disturbance can be thought of as a superposition of two waves, one corresponding to the C_+ family and the other to the C_- family, into which they split. The two waves thereafter propagate with little change in their form (essentially parallel characteristics). On reversing time, the two waves recombine to give the initial disturbance correct to the irreversible diffusion arising out of the viscosity† of the discretization‡ (the pressure profiles are shown in Fig. 4.5.2). This reconfirms the linear superposability of the solutions. Further, the high degree of *macro-reversibility*♯ of the flow could perhaps be interpreted as due to the primarily isentropic nature of the disturbance*.

† see previous chapter

‡ In fact part of the error is ascribable to imperfections in the initial data.

♯ Any classical process is micro-reversible.

* This is *non-trivial* considering the poor understanding of the thermodynamics of discrete-velocity gases.

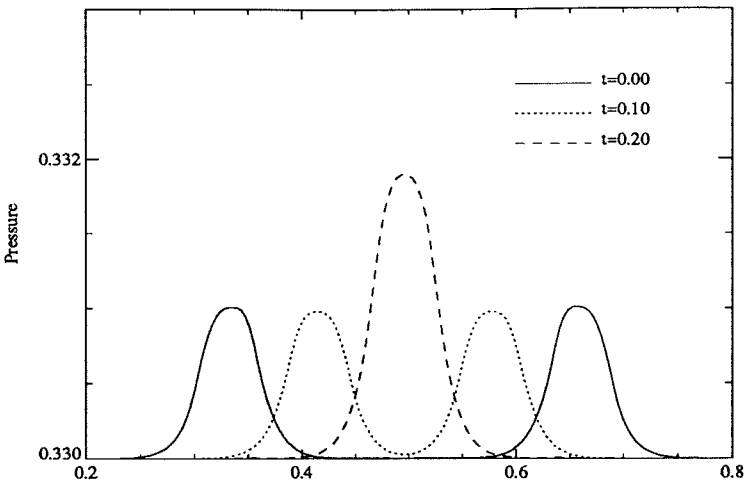

FIG. 4.5.2 Reversing time at t=0.4, the C_+ and the C_- waves recombine to reconstruct the original initial condition verifying linear superposition and isentropy of the disturbances

4.6 Nonlinearity of the Model Euler Equations

The nonlinearity of the model Euler equations is next tested by monitoring the steepness of an initially shallow compressive wave. The best setup for this is of course a *simple*** compression wave propagating into an uniform state. Not knowing the Riemann invariants in discrete-velocity gases prevents such an explicit setup. So, instead the time evolution of an initial hyperbolic tangent interface between an equilibrium upstream and an equilibrium downstream state, with the two equilibria satisfying the Rankine-Hugoniot jump conditions (see later) is studied. Dirichlet boundary conditions are prescribed at the inflow and outflow boundaries: the gradients of all the flow variables are prescribed to be zero. Fig. 4.6.1 compares the steepness of the pressure profiles. The profiles have been offset by the distance they have traveled to make the comparison. The steepening is evident.

The steepening of the front is clearly indicative of the nonlinearity: the speed of propagation of the disturbance ω_+ varies as the magnitude of the disturbance (say p)†.

** The usage of *simple* is in a gas-dynamic sense, wherein only one of the three families of characteristics are not parallel.

† *c.f* $d(u+a) = \frac{\Gamma}{\rho c} dp$ for a perfect gas.

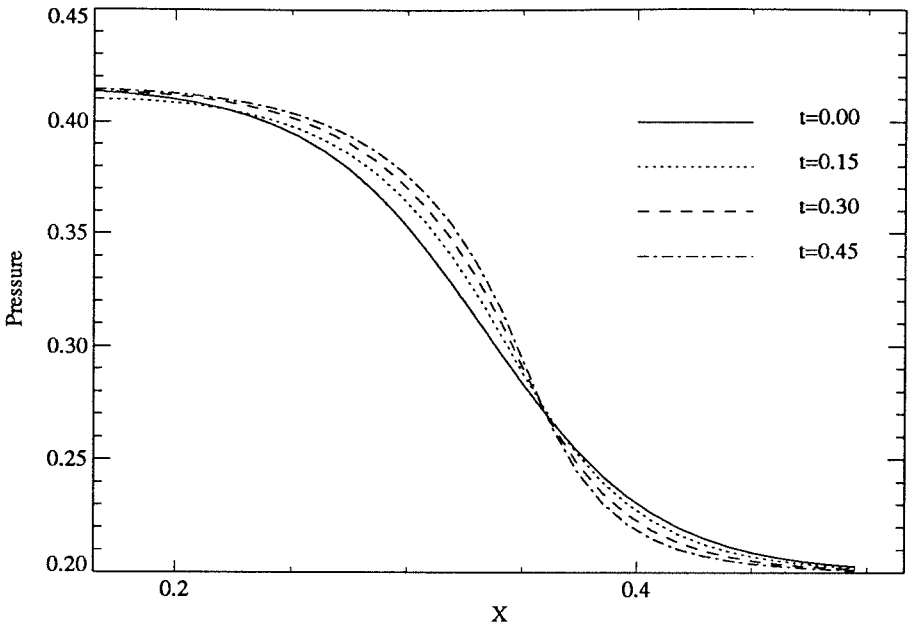

FIG. 4.6.1 Steepening of a compressive wave

Fig. 4.6.2 shows how an initially steep expansion front gets shallower with time. It should however be noted again that the situation in either of the above two cases is not *exactly* that of a simple wave because all that can be said for certain is that the variation spans across two uniform regions.

4.7 Jump Conditions

Viewed in terms of $\boldsymbol{\Phi}$, the model Euler equations Eq. 4.1.4 are three partial differential equations in the three hydrodynamic variables ρ, u and e[‡]. Consider an infinitesimally thin shock wave moving with a velocity U. While all discussion in this chapter assumes the frame of reference of the model, the frame in which the allowed particle velocities are those in Fig. 1.2.3, to write an expression for the jump across the shock, momentarily fix the frame of reference with the wave. Then $\partial/\partial t$ can be replaced by $-U\partial/\partial x$. Integrating the resulting equations from ahead of the shock to behind it, gives the shock jump conditions

‡ The equations are not written explicitly in terms of (ρ, u, e), because, as mentioned before, the flux of (ρ, u, e) are not expressible explicitly in terms of (ρ, u, e).

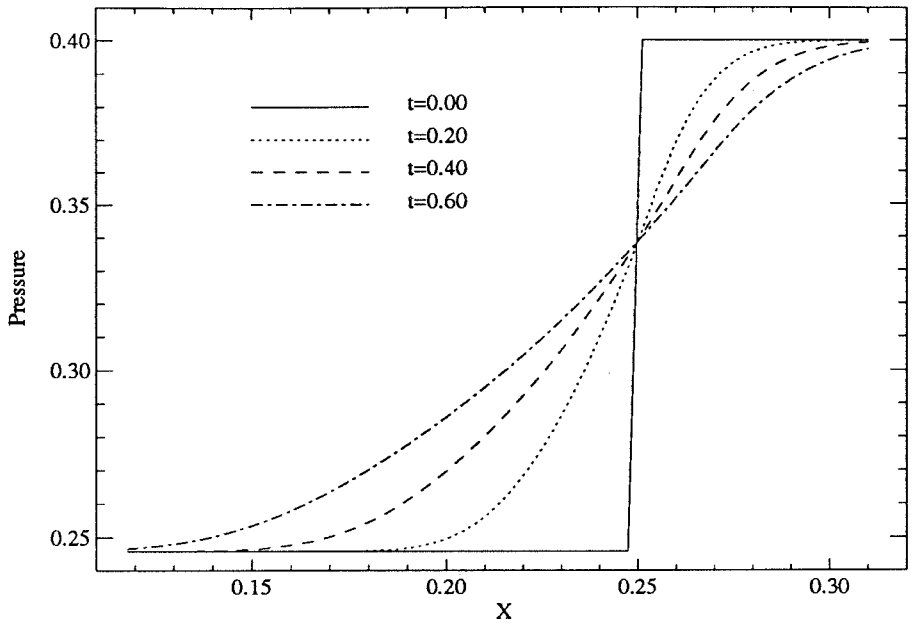

FIG. 4.6.2 An initially steep expansion wave becomes shallower with time (Whitham 1974)

$$[\![\mathbf{G(n)}]\!] = U[\![\mathbf{F(n)}]\!]. \tag{4.7.1}$$

Given the upstream density, specific energy, and flow velocity (ρ_u, e_u, u_u), the three algebraic equations can be solved to obtain the downstream state. Equivalently, given the upstream state and one of the quantities downstream, the shock velocity and the rest of the downstream quantities can be determined.

The computational setup used in studying shocks and other discontinuities is exactly like the one used for studying the steepening of compressive waves (flux-limited, second order near-equilibrium flow technique of chapter 3). The computations are all on the domain [0,1] with Dirichlet boundaries: zero gradients of all flow quantities at the inflow and outflow boundaries. The initial conditions in all the cases is a step discontinuity[♯], **J** between the upstream state and the downstream state:

$$\mathbf{J_0} : (\rho_u, e_u, u_u) \overset{U}{\longrightarrow} (\rho_d, e_d, u_d)\,, \tag{4.7.2}$$

♯ Note the robustness of the method in handling such steep data.

obtained as a solution of the algebraic system Eq. 4.7.1, unless stated otherwise. The subsequent time evolution of the discontinuity is studied.

1. The initial condition in Fig. 4.7.1*

$$\mathbf{J_0} : (1.000, 0.100, 0.000) \xrightarrow{U} (1.137, 0.152, 0.100) \tag{4.7.3}$$

has no explicit information about the direction of propagation of $\mathbf{J_0}$ or its speed. The jump $\mathbf{J_0}$ satisfies the jump conditions of the Euler equations Eq. 4.7.1 for U=0.828. Evolving the initial condition, the jump $\mathbf{J_0}$ is seen to be preserved with time and it propagates with a speed $U = 0.828$ to the right, exactly as obtained by the Euler equations. The entropy, defined using a Boltzmann-like H function, is seen to rise across the shock in this particular case. However, as will be seen in some of the next examples, the entropy so defined does not always behave as expected. The characteristic velocities upstream and downstream are $C_u = (\mathbf{0.742}, -0.742, 0.000)$ and $C_d = (\mathbf{0.881}, -0.554, 0.014)$, where they are expressed as $(\omega_+, \omega_-, \omega_0)$.

2. Time evolution of the initial jump

$$\mathbf{J_0} : (1.000, 0.400, 0.000) \xrightarrow{U} (0.791, 0.313, -0.200) \tag{4.7.4}$$

in Fig. 4.7.2 shows that the jump is stable in the sense that it does not break up into different jumps, but the jump is seen to disintegrate** in time. The jump conditions Eq. 4.7.1 arising from the Euler equations do not rule out such shocks (as in Eq. 4.7.4), therefore a possible external constraint has to be invoked. This is seen to be the kinematic *supersonic-subsonic* condition: the shock must travel faster than the speed of propagation of an infinitesimal disturbance *in the direction of shock propagation*† upstream of the shock and slower than the speed of propagation of

---

* All the quantities in the figure and everywhere else in this chapter are in their non-dimensionalized form: density corresponds to the average number of particles in a cell, velocities are non-dimensionalized by q, the unit speed of the model, and energies by q^2.

** The tendency towards reducing the slopes of all relevant quantities to zero.

† The emphasis on the direction is because of the lack of Galilean-invariance.

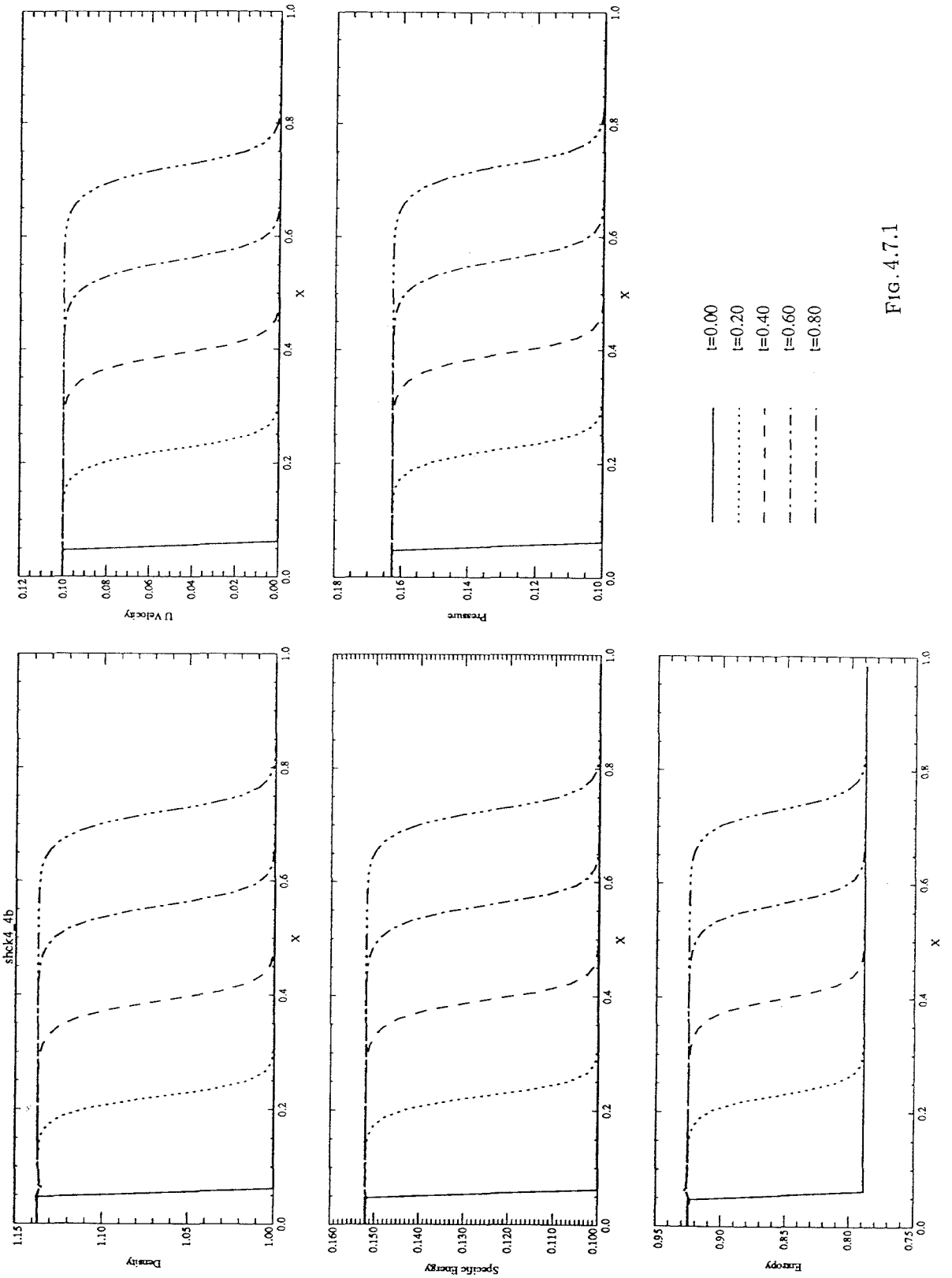
shck4_4b
Density
U Velocity
Pressure
Specific Energy
Entropy
X
t=0.00
t=0.20
t=0.40
t=0.60
t=0.80

FIG. 4.7.1

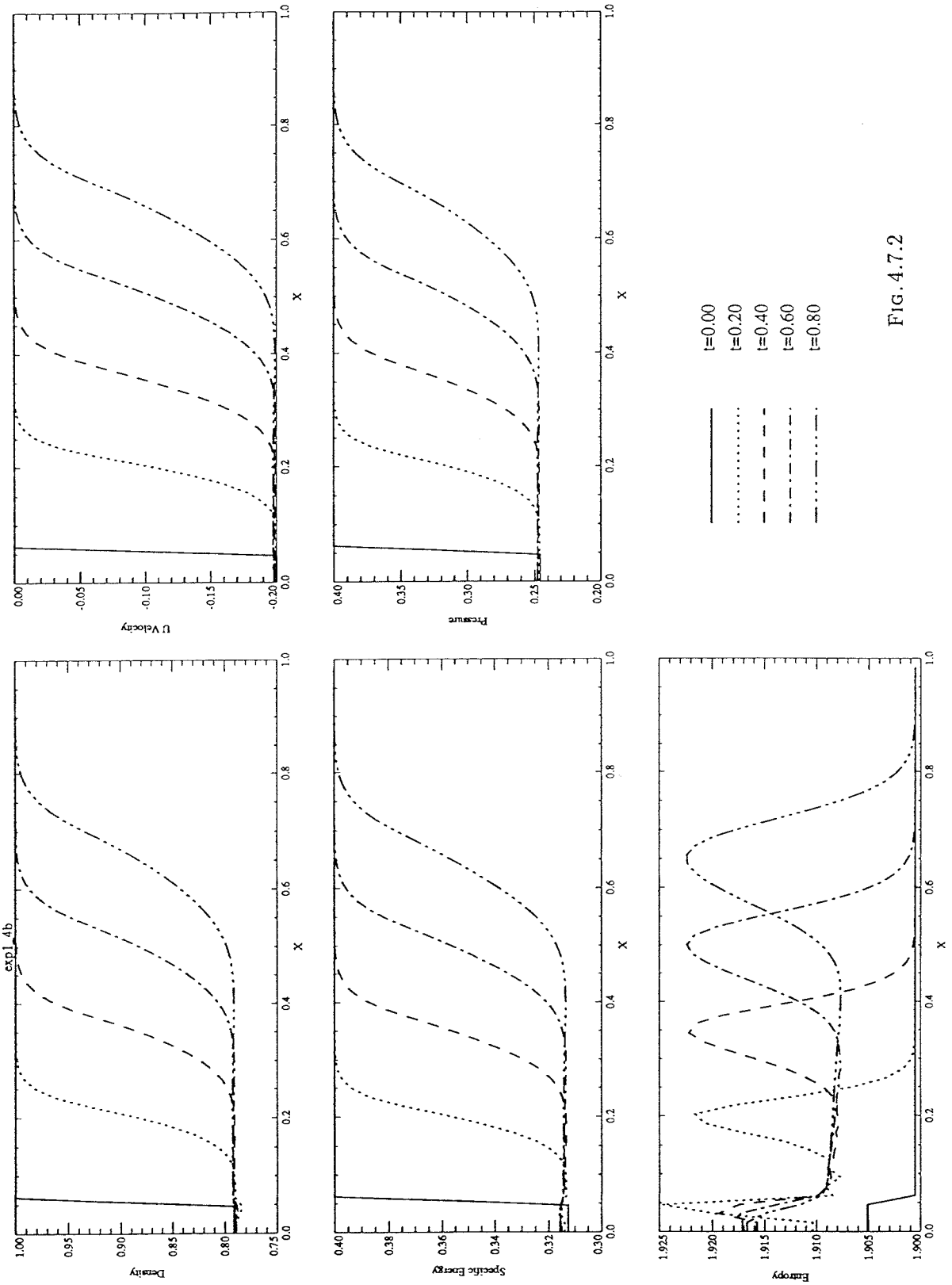
exp1_4b
Density
U Velocity
Pressure
Specific Energy
Entropy
x
t=0.00
t=0.20
t=0.40
t=0.60
t=0.80

FIG. 4.7.2

a disturbance in the same direction downstream of the shock. For example for a C_+ shock[‡], U should be such that $(C_+)_u \leq U \leq (C_+)_d$[♯]. Or in other words the effect of the passage of a shock at a point must be to increase the speed of propagation of a small disturbance in the direction concerned there, if the shock is to propagate stably. The disintegration of the jump $\mathbf{J_0}$ which satisfies the jump condition is explained as due to the violation of the above *supersonic-subsonic* condition. The characteristic velocities upstream and downstream are respectively $C_u = (\mathbf{0.837}, -0.837, 0.000)$ and $C_d = (\mathbf{0.626}, -0.910, -0.052)$, and the initial shock velocity $U = \mathbf{0.758}$.

$$(C_+)_u \not\leq U \not\leq (C_+)_d \tag{4.7.5}$$

The stable shock in case 1 is seen to satisfy the *supersonic-subsonic* condition.

3. This case is identical to case 1, except with a different initial jump, $\mathbf{J_0}$.

$$\mathbf{J_0} : (1.000, 0.400, 0.000) \overset{U}{\longrightarrow} (1.292, 0.455, 0.200) \tag{4.7.6}$$

$\mathbf{J_0}$ satisfies the jump conditions of the Euler equations Eq. 4.7.1 for U=0.885. Evolving the initial condition, the jump $\mathbf{J_0}$ is seen to be preserved with time and it propagates with a speed $U = 0.885$ to the right, exactly as obtained by the Euler equations. The difference between this case and case 1 is in the behavior of entropy — the entropy on the downstream side is lower than that of the upstream side. If the definition of entropy used is correct, the behavior of entropy in the present case is counter to what is expected from the second law of thermodynamics. To better understand the behavior of entropy, it is instructive to look at the corresponding behavior of entropy in the case of a perfect gas. Since some of the thermodynamic arguments can be made more generally than for a perfect gas, the assumption of

‡ A similar relation would hold for a C_- shock but with the absolute values of the speeds concerned.

♯ A C_0 family of shocks are also seen to be possible by replacing subscript + with subscript 0.

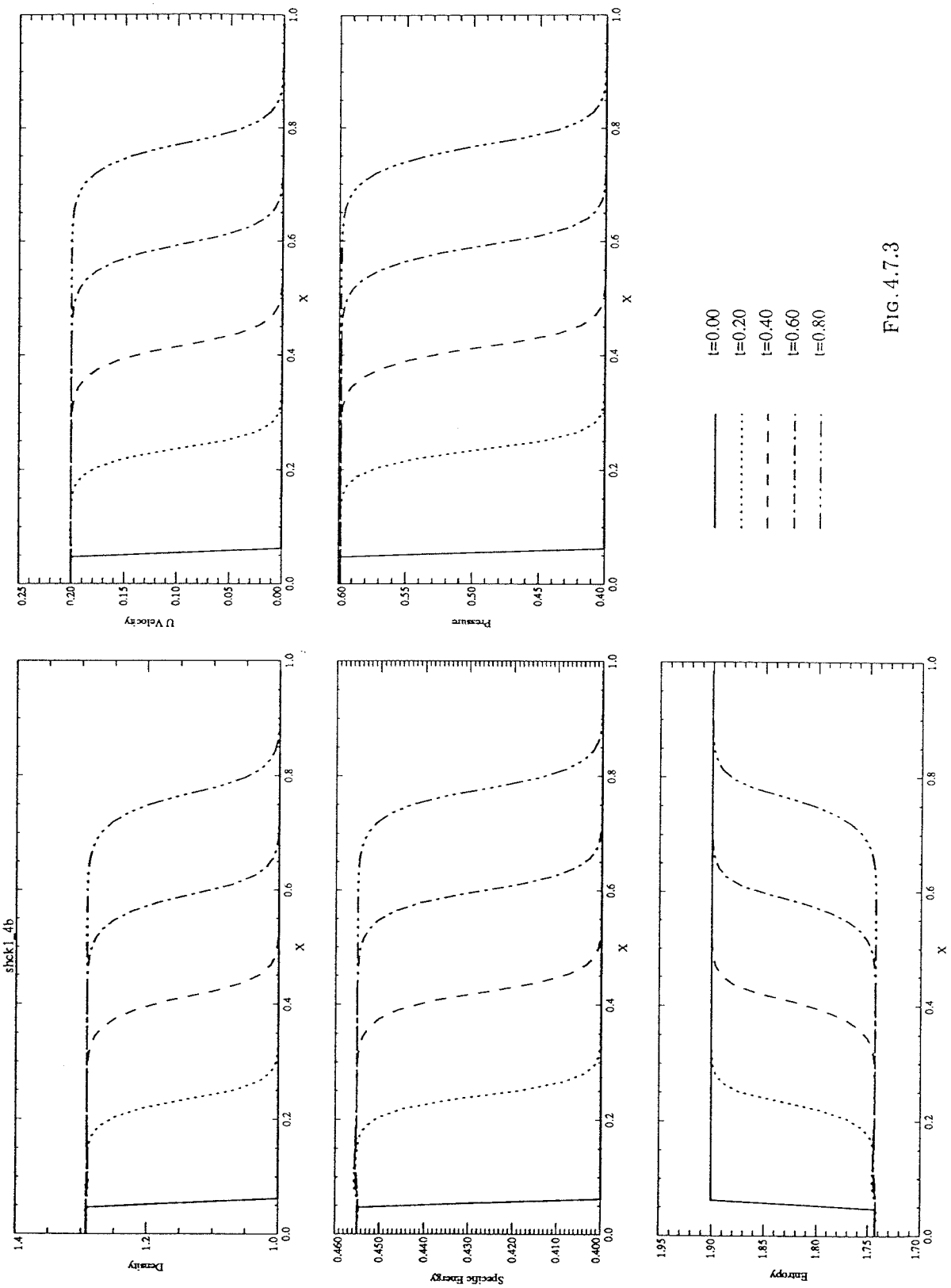
shck1_4b
Density
Specific Energy
Entropy
U Velocity
Pressure
X
t=0.00
t=0.20
t=0.40
t=0.60
t=0.80

FIG. 4.7.3

a perfect gas is introduced only as required. For a normal* fluid, the kinematic *supersonic-subsonic* requirement (equivalent to $([\![u+a]\!] > 0)$ can be related to the variation of thermodynamic quantities across the shock by the following equation.

$$d(u+a) = \frac{\Gamma}{\rho a} dp \tag{4.7.7}$$

where Γ is the fundamental derivative of gasdynamics $\frac{1}{a}\left[\frac{\partial \rho a}{\partial \rho}\right]_s$, ρa the acoustic impedance and a the speed of sound. Therefore, across a shock,

$$[\![u+a]\!] = \int_{p_u}^{p_d} \frac{\Gamma}{\rho a} dp \tag{4.7.8}$$

With $\Gamma > 0$ for a normal fluid, the supersonic-subsonic requirement can be satisfied only with $p_d > p_u$ or through a compressive shock. Next, the entropy jump across a shock should be related to the pressure jump. For a general fluid, the entropy jump across a shock is related to the dimensionless pressure jump across the shock by

$$\frac{T_u [\![s]\!]}{a_u^2} = \frac{1}{5}\Gamma_u \Pi^3 + O(\Pi^4) \qquad \text{where } \Pi = \frac{[\![p]\!]}{\rho_u a_u^2}, \tag{4.7.9}$$

as discussed in Thompson,1988. By the previous argument, Π is established to be greater than zero for a stable shock; for a normal fluid, $\Gamma_u > 0$, so that $[\![s]\!] > 0$ if $T_u > 0$, which is usually the case**. This result can be shown equivalently for a perfect gas as follows: consider the equilibrium states upstream and downstream of the compressive shock. Entropy being a state variable, the entropy jump is fully determined by the two equilibrium states.

$$[\![s]\!] \propto \log_e \left\{ \frac{p_u}{p_d} \left(\frac{e_d}{e_u} \right)^{\frac{\gamma}{\gamma-1}} \right\} \tag{4.7.10}$$

Since the model fluid being studied is two dimensional, γ, the ratio of specific heats, γ is 2. Further, using the ideal gas equation of state,

$$[\![s]\!] \propto \log_e \left\{ \frac{\rho_u}{\rho_d} \frac{e_d}{e_u} \right\}. \qquad \text{Thus} \quad [\![s]\!] > 0 \quad \text{only if} \quad \frac{e_d}{e_u} > \frac{\rho_d}{\rho_u}. \tag{4.7.11}$$

---

* As opposed to a retrograde fluid (Thompson 1988)

** The entropy usually increases with an increase in the specific energy at a constant specific volume. This is not true, *e.g.*, in systems whose phase space is finite.

Since this is always true for a compressive shock in a perfect gas, the entropy jump across a compressive shock in a perfect gas is always positive. From the molecular description of the lattice gas models being studied here, the fundamental derivative of gas dynamics for these models can be shown to be positive; we assume so here. Numerical evidence to substantiate the assumption is strong. Thus from Eq. 4.7.7, only compressive shocks are allowed in these models. A complication however in studying the variation of entropy with lattice gases is the third independent state variable, the macroscopic flow velocity u. Thus $s = s(\rho, e, u)$. But by confining to small macroscopic flow velocities u, to a first approximation, $s = s(\rho, e)$. In this approximation, the sign of the entropy jump across compressive shocks can be established by the inequality in Eq. 4.7.11. Unlike for a perfect gas, for a lattice gas, even for a compressive shock, there are only certain regimes when $\frac{e_d}{e_u} > \frac{\rho_d}{\rho_u}$. Thus there are regimes where the entropy jump across a compressive shock in a lattice gas can be negative. The similarities of the situation here to the case of shocks in superfluid helium, Moody & Sturtevant (1984), are to be looked into. The case shown in Fig. 4.7.3 corresponds to a choice of initial conditions in the nine-velocity gas which puts the shock in such a regime. Though it is certain to be the case, the above case of an entropy decreasing shock needs to be reproduced with lattice gas automata to rest all doubts.

4. If Eq. 4.7.9 should hold for lattice gases, then since a regime can be identified where the temperature is negative (Appendix 1), the entropy should decrease across a compressive shock if the initial condition was chosen to have a negative temperature upstream.

5. Finally consider an initial condition with two jumps,

$$\begin{aligned} \mathbf{J_1} : (1.000, 0.100, -0.900) &\xrightarrow{U_1} (2.615, 0.536, 0.000) \\ \mathbf{J_2} : (2.615, 0.536, 0.000) &\xrightarrow{U_2} (3.354, 0.572, 0.200) \end{aligned} \tag{4.7.12}$$

both satisfying the Rankine-Hugoniot jump conditions Eq. 4.7.1 for propagation velocities U_1 and U_2, both satisfying the supersonic-subsonic requirement for stable propagation. Fig. 4.7.4 shows the $x - t$ plot wherein the second shock catches up with the first and then on propagate as one.

4.7.1 The Shock Tube Problem

Finally, a simulation of the shock tube is considered, the gas in the tube is the nine-velocity gas. The initial condition corresponds to a high density, high pressure driver section and a low density, low pressure driven section, separated by a diaphragm which ruptures at $t = 0$. The initial jump is

$$\mathbf{J_0} : (1.000, 0.500, 0.000) \xrightarrow{U} (0.200, 0.200, 0.000) \tag{4.7.13}$$

The gas in the two regions are the same. The end walls are modeled by mirror image sites across the physical wall. This results in specular walls, which therefore act as no-flow (zero mass flux), adiabatic (zero total energy flux) boundaries. The time evolution of density and entropy are shown using a color coding on the $x - t$ plane in Figs. 4.7.5a and 4.7.5b. The pictures show that the qualitative nature of the the interaction of the various types of waves, the shock wave, the rarefaction fan, and the contact surface is captured rather realistically in the nine-velocity model.

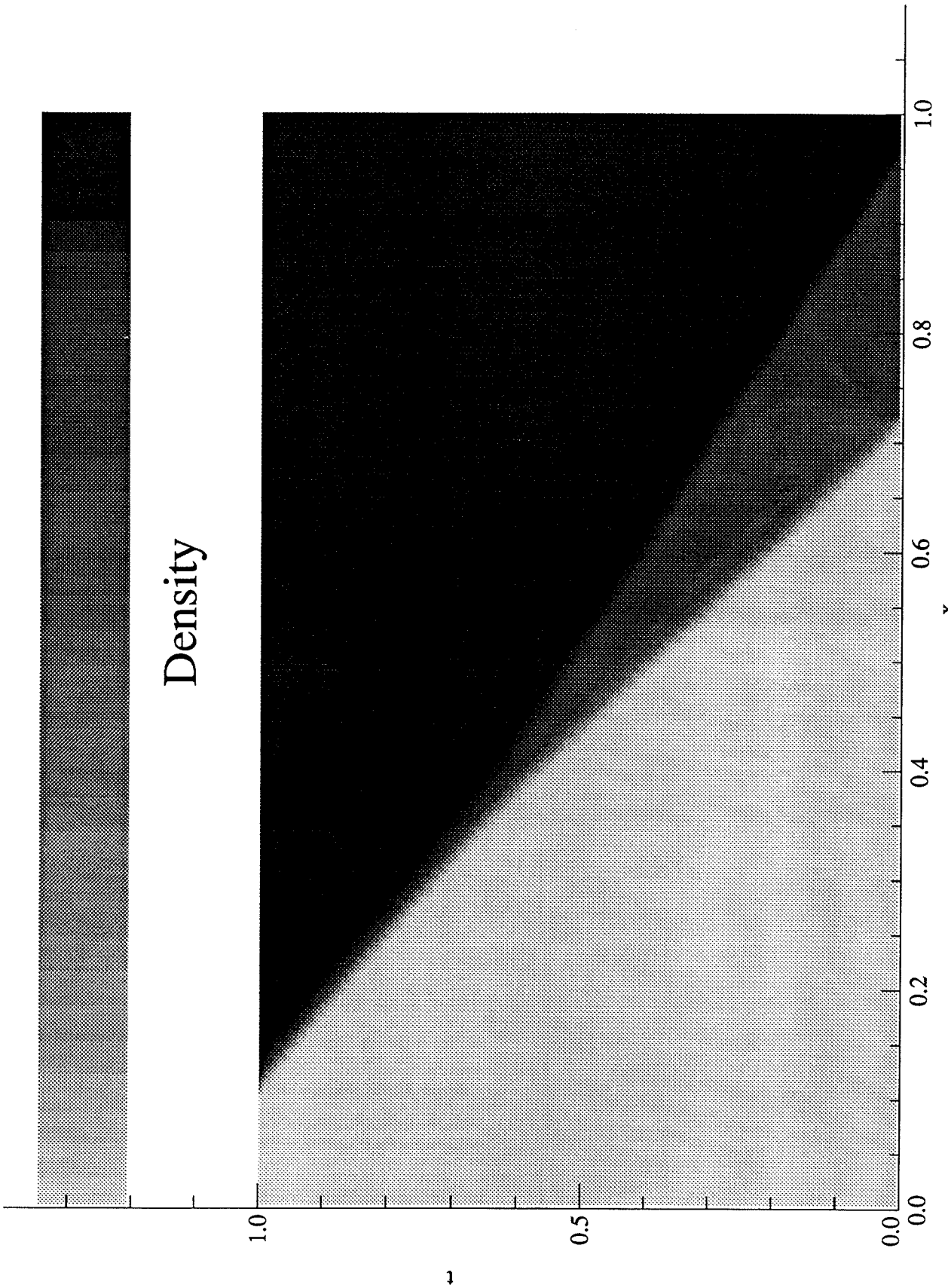

FIG. 4.7.4

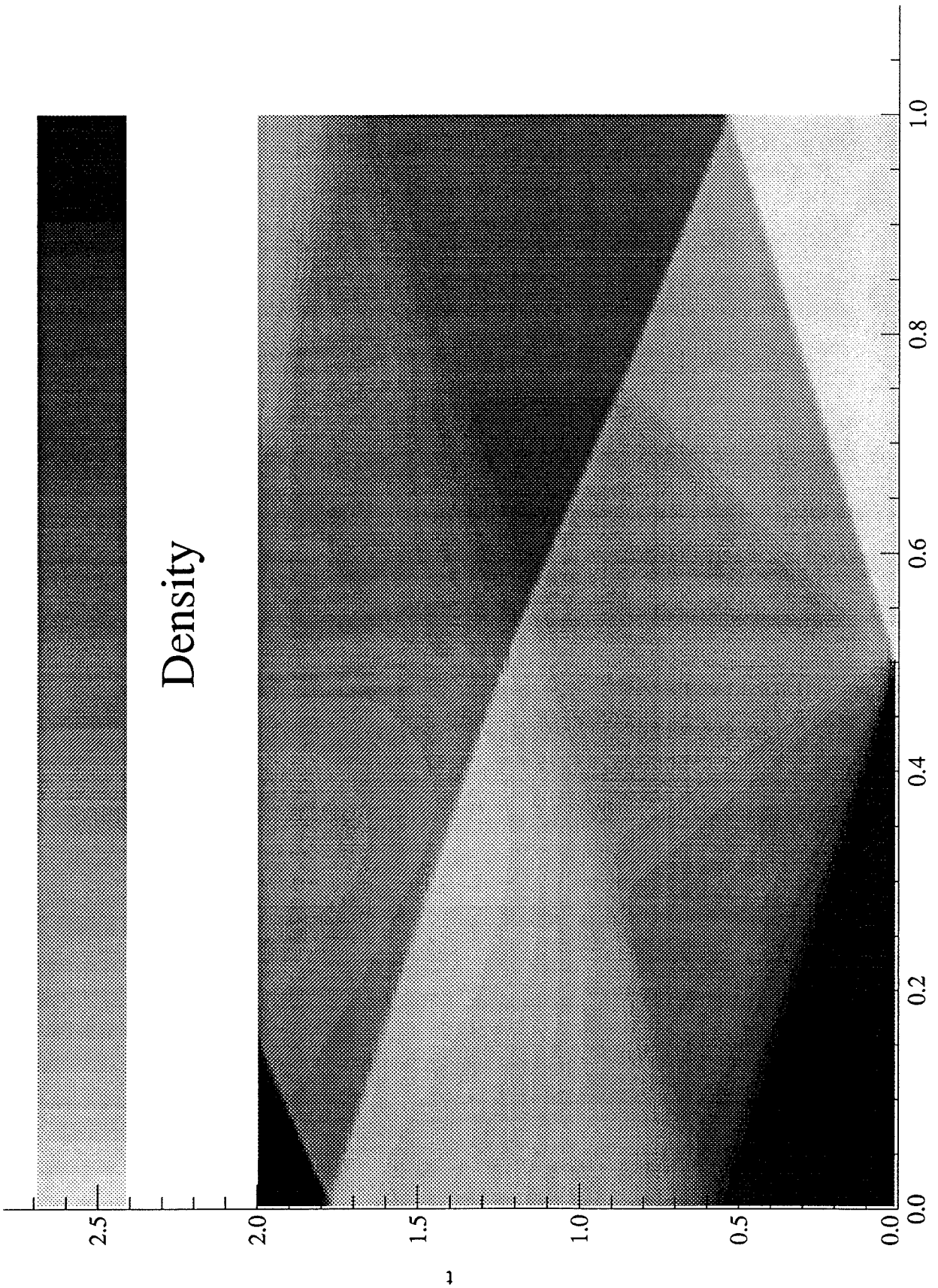

FIG. 4.7.5a

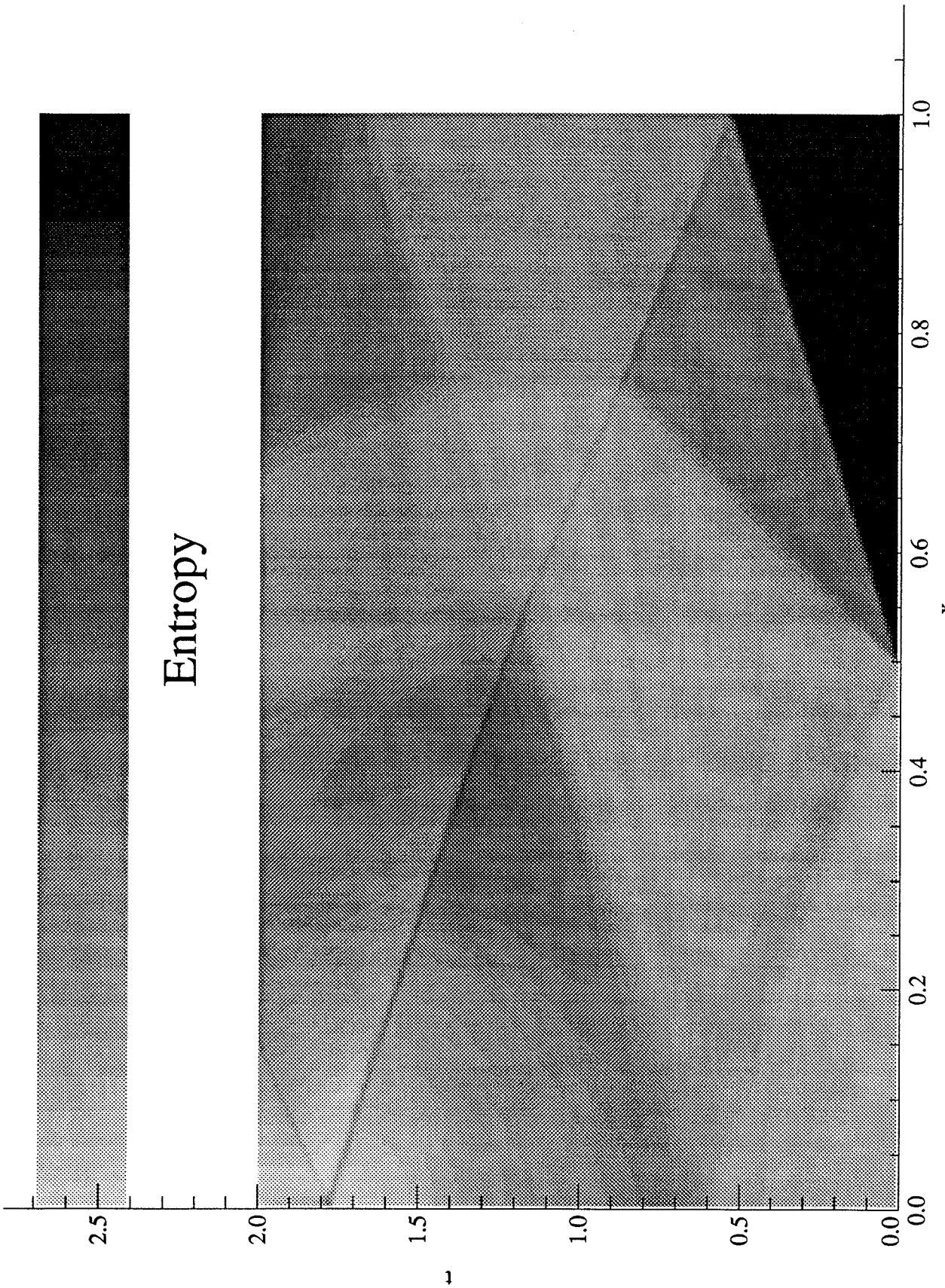

FIG. 4.7.5b

CHAPTER 5

Shock Structure In the Nine-Velocity Gas

5.1 Introduction

In Chapter 4, it was shown that the flow of the nine-velocity gas can never be supersonic. This was shown computationally by observing that no matter what the flow velocity and the specific energy, the three characteristic velocities of the model Euler equation were never of the same sign. This rules out the possibility of steady shock waves in the model. Unsteady shock waves however are no problem — they are rather natural and necessary: imagine the simple act of starting a piston at $t = 0$ and then pushing it continuously with a constant velocity to the right through a long frictionless channel of the discrete-velocity gas at rest. The information about the piston being pushed does not propagate with infinite speed; this is particularly clear in the present context of discrete-velocity gases where the fastest speed that can ever be reckoned is the speed of the fastest particle in that direction allowed in the model. Confining attention to the region right of the piston, on the $x - t$ plane, there is clearly a region of silence and a region of disturbance. The interface between these two regions is the shock wave. In this chapter, the structure of such an unsteady shock wave is discussed.

The possibility of such shock waves and their stability was discussed in chapter 4 under a discussion of the model Euler equations. Thus the jump conditions and the shock velocity are all obtained by an analysis of the Euler equations. Then letting the frame of reference translate with the shock velocity, the problem is steady, and this reduces the governing partial differential equations to ordinary differential equations. With *a priori* knowledge of

the jump conditions, the problem could be set up as a two point boundary value problem. However, setting the problem up as an initial value problem is more illustrative of the physics involved. This is motivated by Gilbarg and Paolucci's approach to the problem of the shock structure in the Navier-Stokes equations, as in Gilbarg & Paolucci (1953). Broadwell (1964b), took a similar approach in analyzing the *infinite* Mach number* shock in his six-velocity, single speed model in three dimensions, but had the luxury of reducing the number of dependent variables to one, and solving the differential equation exactly. Gilbarg and Paolucci easily reduced the number of dependent variables in the context of Navier-Stokes equations to two and thus the treatment of the problem was reduced to an analysis of the flow generated by two ordinary differential equations on the two-dimensional plane. That analysis yielded elegant results. Unfortunately, in the case of the nine-velocity gas, on maximal simplification, we could only reduce the number of dependent variables to three and this complicates the analysis, forcing us to treat the situation almost entirely computationally.

In the context of the nine-velocity model, a thermodynamic equilibrium state is defined by a point in the three dimensional phase space and the shock solution is a line in this 3-D space connecting two thermodynamic equilibria which satisfy the shock jump relations. Uniqueness of this solution curve is assumed. Considering the thermodynamics of the situation, this is almost certain to be so. Sec. 5.2 develops the ordinary differential equations governing the shock solution, starting from the Boltzmann equations and Sec. 5.3 analyses the equations for a particular initial value and tracks the solution curve for that case. Sec. 5.4 takes a gas dynamic view of the situation and some comments are made in the light of shock structures in an ideal gas, as given by the Navier-Stokes equations. Finally in Sec. 5.5, a comparison is made of the present solutions to that obtained from the equilibrium flow technique of chapter 3. Considering that the method was introduced primarily to study

---

* see Sec. 4.3.

Euler solutions**, the comparison shows that the method errs, *i.e.*, deviates from the Euler solutions in the *right* direction.

5.2 The Governing ODEs

The flow is assumed identically uni-directional — along the x-axis — so that $v = 0$ in the whole region of interest. With that simplification, from the form of the equilibrium distribution presented in chapter 2, it follows that

$$n_8 = n_2, \quad n_7 = n_3, \quad \text{and} \quad n_6 = n_4 \,. \tag{5.2.1}$$

The variables in the problem then are $(n_0, \ldots, n_5)$, varying with x and t, as given by the Boltzmann equations in Table 1, reproduced here symbolically as

$$L_i n_i = Q_i(n_j, n_j) \qquad i, j = 0, \ldots, 5 \,. \tag{5.2.2}$$

L_i is the linear streaming operator of particle type i, given by $L_i = \partial/\partial t + c_{ix}\partial/\partial x$ and Q_i is the non-linear collision operator. Since the operator L_i acts only on particle type n_i, n_i will be dropped when convenient, with no ambiguity. If however, the shock wave of interest is traveling with a velocity U, fixing the frame of reference with the shock wave, enables rewriting the time derivative in terms of the spatial derivative, so that, $L_i = (-U + c_{ix})d/dx$ These equations can be written in a more convenient form by noting that the six variables $(n_0, \ldots, n_5)$, satisfy three linear homogeneous equations, expressing the conservation of mass, momentum, and total energy†. The three linear equations are solved to express three of the $L_i s$ in terms of the other three.

$$\left.\begin{aligned} L_0 - 2L_2 - 2L_4 &= 0 \\ L_1 - L_5 + 2L_2 - 2L_4 &= 0 \\ L_1 + 3L_2 + L_3 + L_4 &= 0 \end{aligned}\right\} \quad \Rightarrow \quad \left\{\begin{aligned} L_0 &= 2L_2 + 2L_4 \\ L_1 &= -3L_2 - L_3 - L_4 \\ L_5 &= -L_2 - L_3 - 3L_4 \end{aligned}\right. \tag{5.2.3}$$

** in which limit shocks are discontinuities with no structure to them.

† The same formulation, as in Cornille (1991).

Integrating the equations on the right, n_0, n_1, and n_5 can be expressed in terms of $\mathbf{n} = (n_2, n_3, n_4)$ and their boundary values, either upstream or downstream:

$$\begin{aligned} n_0(x) &= n_0(\mathbf{n}(x), \mathbf{n}(-\infty)) \qquad & n_0(x) &= n_0(\mathbf{n}(x), \mathbf{n}(\infty)) \\ n_1(x) &= n_1(\mathbf{n}(x), \mathbf{n}(-\infty)) \quad \text{or} \quad & n_1(x) &= n_1(\mathbf{n}(x), \mathbf{n}(\infty)) \\ n_5(x) &= n_5(\mathbf{n}(x), \mathbf{n}(-\infty)) \qquad & n_5(x) &= n_5(\mathbf{n}(x), \mathbf{n}(\infty)) \end{aligned} \tag{5.2.4}$$

The variation of the three primary dependent variables represented by $\mathbf{n}$ is given by the three non-linear equations

$$\begin{aligned} L_2 &= \sqrt{2}A_1 - \sqrt{5}C \\ L_3 &= -(\sqrt{2}A_1 + \sqrt{2}A_2 + 2D) \\ L_4 &= \sqrt{2}A_2 + \sqrt{5}C \end{aligned} \tag{5.2.5}$$

where the collision terms A_1, A_2, C, and D are given by

$$\begin{aligned} A_1 &= n_1 n_3 - n_0 n_2 \\ A_2 &= n_3 n_5 - n_0 n_4 \\ C &= n_2 n_5 - n_1 n_4 \\ D &= n_3^2 - n_1 n_5 \end{aligned} \tag{5.2.6}$$

- Non-dimensionalization: Any of the equations Eq. 5.2.5 is dimensionally of the form

$$(q + \xi)\frac{dN_2}{dx} = qS\left\{\sqrt{2}(N_1 N_3 - N_0 N_2) + \cdots\right\} \tag{5.2.7}$$

where q is the unit of velocity in the model, and S is the collision cross-section, taken to be independent of the relative velocity of the collision. Dividing the above equation by $qn_{ref} = qn_d$, where n represents the particle density, subscript d downstream, Eq. 5.2.7 can be written in the non-dimensional form as

$$(1 + \frac{\xi}{q})\frac{dn_2}{d\eta} = \sqrt{2}(n_1 n_3 - n_0 n_2) + \cdots \tag{5.2.8}$$

where $n_i = N_i/n_{ref}$, $\eta = \alpha_d x/\lambda_d$, λ_d being the downstream mean-free-path given by $\lambda_d = \alpha_d/(n_d S)$, as obtained by standard kinetic theory calculations‡. The equations Eq. 5.2.5 *etc.* previously used are all of the non-dimensional form like Eq. 5.2.8

‡ using the exact velocity distribution of the downstream.

The structure of the shock is then contained in the variation of $\mathbf{n}$ with x, as given by Eq. 5.2.5. Rewriting those equations symbolically in a compact and convenient form,

$$\frac{d\mathbf{n}}{d\eta} = [\mathbf{A}_{-\infty} \text{ or } \mathbf{A}_{\infty}]\,\mathbf{n} + \mathbf{n}^T\mathbf{B}\mathbf{n} \tag{5.2.9}$$

where $\mathbf{A}$ is a 3x3 matrix depending on the initial values of $\mathbf{n}$ and $\mathbf{B}$ is a vector of three 3x3 matrices, *i.e.*, $\mathbf{B}=(B_2, B_3, B_4)$, where B_2 is a 3x3 matrix *etc.*All the $\mathbf{B}$ matrices are determined by only the collisions in the model, and thus are independent of the particular shock, unlike the $\mathbf{A}$ matrix.

$$B_2 = \begin{pmatrix} -4\sqrt{2} - 2\sqrt{5} & -2\sqrt{2} - \frac{2\sqrt{5}}{3} & \frac{4\sqrt{2}}{3} \\ -2\sqrt{2} - \frac{2\sqrt{5}}{3} & -\frac{2\sqrt{2}}{9} & \frac{2\sqrt{2}}{9} - \frac{2\sqrt{5}}{9} \\ \frac{4\sqrt{2}}{3} & \frac{2\sqrt{2}}{9} - \frac{2\sqrt{5}}{9} & \frac{2\sqrt{5}}{9} \end{pmatrix}$$

$$B_3 = 2\begin{pmatrix} -6\sqrt{2} - 18 & -8 & 20 + 4\sqrt{2} \\ -8 & -\frac{2\sqrt{2}}{3} - \frac{8}{3} & \frac{8\sqrt{2}}{3} + \frac{4}{3} \\ 20 + 4\sqrt{2} & \frac{8\sqrt{2}}{3} + \frac{4}{3} & -2\sqrt{2} - 2 \end{pmatrix} \tag{5.2.10}$$

$$B_4 = 2\begin{pmatrix} -3\sqrt{5} & -3\sqrt{2} - \sqrt{5} & 6\sqrt{2} \\ -3\sqrt{2} - \sqrt{5} & -\sqrt{2} & 3\sqrt{2} - \frac{\sqrt{5}}{3} \\ 6\sqrt{2} & 3\sqrt{2} - \frac{\sqrt{5}}{3} & -2\sqrt{2} + \frac{\sqrt{5}}{3} \end{pmatrix}$$

Linearization about the upstream equilibrium given by $\mathbf{n}_{-\infty}$ leads to

$$\mathbf{n} = \mathbf{n}_{-\infty} + \eta \quad \Rightarrow \quad \frac{d\eta}{dx} = \mathbf{A}_{-\infty}\eta \tag{5.2.11}$$

A similar linearization about the downstream equilibrium state gives the matrix $\mathbf{A}_{\infty}$.

5.3 A Strong Shock

The case considered here corresponds to the case of a collimated beam of particles, type 1, see Fig. 1.2.3, encountering a wall. To satisfy the geometrical boundary condition of no flow through the wall, a shock wave emanates from the wall and propagates into the incoming particle stream, bringing the flow to a halt behind it. Cornille, 1991 attempts to *construct* solutions to the above problem. The physics involved in that attempt is, however, far from clear, *e.g.*, the behavior of the collision cross-sections of the particles is not defined *a priori* and the collision cross-sections are left as parameters. After the *solutions* have been constructed, the parameter space is searched for positive regions to select the solutions of interest. In light of the above, no attempt will be made to compare the solutions obtained here to those of Cornille.

The jump across the shock above is given by

$$\mathbf{J} : (1.000, 0.000, 1.000) \overset{-0.5}{\longrightarrow} (3.000, 0.500, 0.000) \tag{5.3.1}$$

as obtained from the Euler equations[♯]. From the same arguments as used in classical kinetic theory, using the distribution function downstream, η in Eq. 5.2.9 is calculated to be $0.709x/\lambda_d$. For this case, (n_0, n_1, n_5) is given in terms of $\mathbf{n}= (n_2, n_3, n_4)$ by

$$\begin{aligned} n_0 &= 6n_2 - 2n_4 \\ n_1 &= 1 - 3n_2 - \frac{n_3}{3} + \frac{n_4}{3} \\ n_5 &= 3n_2 + n_3 - 3n_4 \end{aligned} \tag{5.3.2}$$

In terms of $\mathbf{n}$, the upstream equilibrium state is given by (0,0,0) and the downstream equilibrium state is $(\frac{3}{16}, \frac{3}{8}, \frac{3}{16})$. The $\mathbf{A}_{-\infty}$ and $\mathbf{A}_{\infty}$ are then

$$\mathbf{A}_{-\infty} = \begin{pmatrix} 0 & \frac{2\sqrt{2}}{3} & \frac{2\sqrt{5}}{3} \\ 12 & 2(2-\sqrt{2}) & -12 \\ 0 & 0 & 2\sqrt{5} \end{pmatrix} \qquad \mathbf{A}_{\infty} = \begin{pmatrix} -\sqrt{5}-2\sqrt{2} & \frac{\sqrt{2}-\sqrt{5}}{6} & \frac{2\sqrt{5}+\sqrt{2}}{3} \\ 6\sqrt{2} & -2(1+\sqrt{2}) & 2(\sqrt{2}-2) \\ -3\sqrt{5} & -\frac{\sqrt{5}-3\sqrt{2}}{2} & 2\sqrt{5}+3\sqrt{2} \end{pmatrix} \tag{5.3.3}$$

♯ Note that the particle number densities are normalized with respect the upstream value.

The linear stability of the upstream and the downstream equilibria are fully defined by the **A** matrices above. The eigenvalues of $\mathbf{A}_{-\infty}$ are found to be (4.472, 4.000, -2.828) and the eigenvalues of $\mathbf{A}_{\infty}$ (7.644, -6.214, -2.608). Since the upstream and downstream equilibria are both hyperbolic*, the linear stability analysis is sufficient locally, *i.e.*, the stability type is not changed by the nonlinearity. Therefore, it is clear that while the upstream equilibrium has a two dimensional unstable manifold** and a stable direction, the downstream equilibrium has a two dimensional stable manifold† and an unstable direction.

5.3.1 The Shock Profile

The stability nature of the upstream and the downstream equilibria in the present case is a rather unfortunate situation because the flow in the phase space near the upstream is such that most of the flow is directed away from the upstream equilibrium and the flow near the downstream is such that the downstream equilibrium can be reached from anywhere on the two-dimensional stable manifold there. In effect, it is neither possible to isolate a direction upstream, along which the shock solution leaves the upstream equilibrium nor a direction downstream along which the shock solution marches to the downstream state. The shock solution is the intersection of the upstream two-dimensional unstable manifold and the downstream two-dimensional stable manifold. We assume that the intersection of the two 2-D manifolds is transverse because non-transverse intersection is rather degenerate and the thermodynamics strongly suggest a unique solution curve.

In searching for the shock curve connecting the upstream and the downstream states numerically, it is advantageous to start from the downstream state, given the relative magnitudes of the eigenvalues at the downstream and the upstream: starting near the upstream

---

* non-zero real part of all the eigenvalues

** the 2-D surface obtained by evolving the space spanned by the two eigenvectors corresponding to the two unstable eigenvalues forward to ∞ under the full non-linear equations.

† similarly obtained by evolving back to $-\infty$ the stable eigenspace under the full nonlinear vector field.

and marching forward, the eigendirection at the target corresponding to the eigenvalue with the largest magnitude is unstable and therefore the search trajectory is very likely to be led away from the target in that direction. If on the other hand, the search started near the downstream equilibrium and proceeded backwards searching for the upstream, the direction associated with the eigenvalue having the largest magnitude is stable and so the chances of the search trajectory reaching the upstream is much better.

By a rather brute force technique, the phase space was searched‡ to obtain the solution curve. The search trajectory was started on the two-dimensional stable manifold of the downstream equilibrium, close to it and evolved backwards under the equation

$$\frac{d\mathbf{n}}{dx} = \mathbf{A}_\infty \mathbf{n} + \mathbf{n}^T \mathbf{B} \mathbf{n} \tag{5.3.4}$$

Departure of the search trajectory from the region of interest terminated that search and a new initial point was picked♯ to restart the search. The iterative search procedure terminated when the search trajectory arrived in a pre-defined neighborhood of the upstream equilibrium. Fig. 5.3.1 shows the shock profile obtained by the above procedure for the shock given by Eq. 5.3.1

5.4 An *ad hoc* Comparison with N-S Profiles

A Navier-Stokes shock profile solver is implemented on the lines of Gilbarg and Paolucci. While the reader is referred to Gilbarg & Paolucci (1953) for the details, the main idea is this: in the shock fixed coordinates, using continuity, density is eliminated and the conservation equations are cast in the form of two odes. The upstream and downstream are then two equilibrium solutions of the odes, with the upstream an unstable node and the downstream a saddle point. With that configuration of equilibria, by picking an initial point

‡ by using knowledge of the solution, the search space was largely constrained.

♯ Decreasingly small arcs of a circle of radius δ were scanned in increasingly fine steps, much like a binary search.

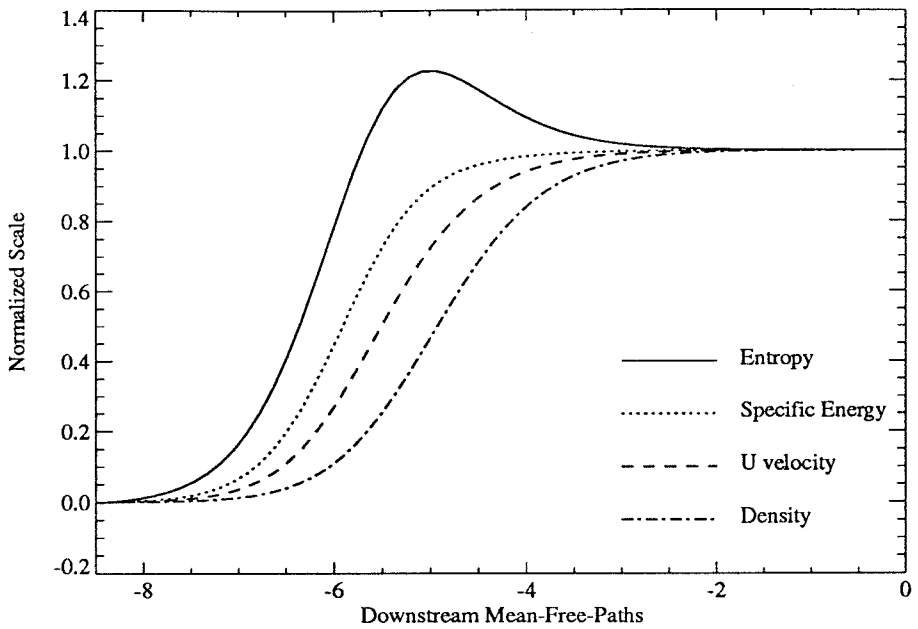

FIG. 5.3.1 The exact normalized profiles of density, velocity, specific energy and entropy across the jump $(1.000, 0.000, 1.000)$–$(3.000, 0.500, 0.000)$ in the nine-velocity gas.

close to the downstream and in the direction given by the eigenvector corresponding to the stable eigenvalue there, evolution of that initial point backwards takes it arbitrarily close to the upstream equilibrium, thus giving the shock profile. In Fig. 5.4.1, the entropy and density profiles previously obtained for the nine-velocity gas are compared to those obtained from the Navier-Stokes equation. For the Navier-Stokes profile, a monatomic hard-sphere molecular model is used giving a power law dependence of viscosity on temperature with an exponent of 0.5 and the molecules move in two spatial dimensions giving a specific heat ratio of 2. The Mach number of the shock was chosen to be 4.0 to roughly match the percentage overshoot of entropy in Fig. 5.3.1. In doing the comparison, the x-axis* of the Navier-Stokes profile was scaled so that the profiles were roughly of the same thickness. The plot shows that the detailed qualitative features of the shock profile in the nine-velocity gas is similar to that in the perfect gas, as described by the Navier-Stokes equations.

* no relative scaling of the y-axes

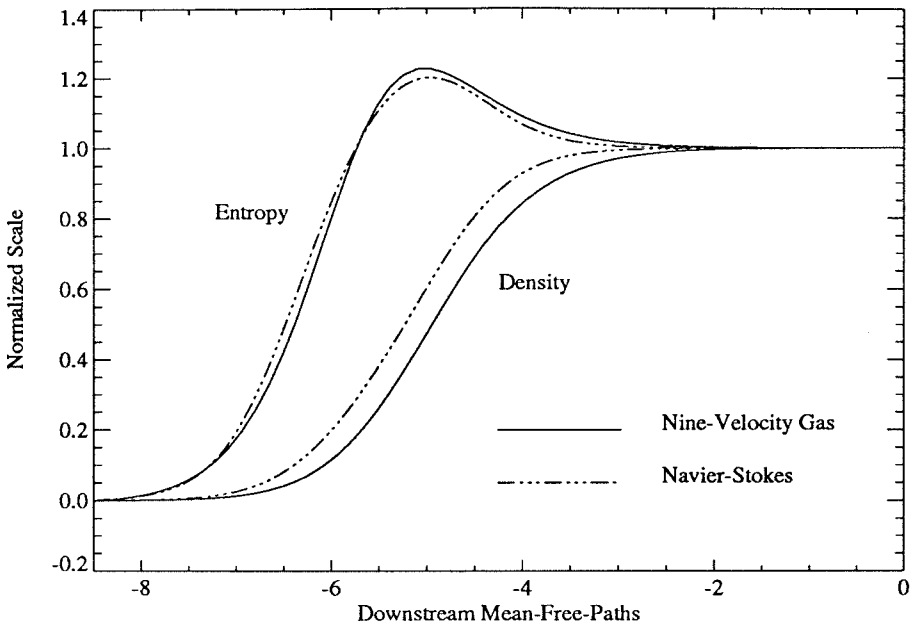

FIG. 5.4.1 A comparison of the entropy and density profiles across a shock using the nine-velocity model for the conditions previously discussed and the Navier-Stokes profile for a 4.0 Mach number 2-D, monatomic, hard sphere gas.

5.5 The Shock Captured by the Near-Equilibrium Flow Technique

The shock jump for which the exact profile was obtained, as previously discussed in this chapter was studied using the near-equilibrium flow techniques of chapter 3. Clearly, if the method was exact, the shock would have to no structure to it, and it would be captured as a perfect discontinuity. However, as discussed in chapter 3, the method is inaccurate and the reader is referred to chapter 3 for a discussion of the inaccuracies and their interpretation in terms of viscosity. Here, it is shown that the inaccuracy of the method, while inevitable, is not entirely undesirable; the *error*, defined as the deviation from the exact solution of the model Euler equations is not arbitrary but is in the physically right direction. In other words the deviations of the solutions obtained by the near-equilibrium flow technique from the exact solutions of the model Euler equations is in some sense like the deviations of of a Navier-Stokes solution with a small viscosity from the Euler solutions. Fig. 5.5.1 compares the shock representation in the flux-limited, second order, equilibrium flow technique to the

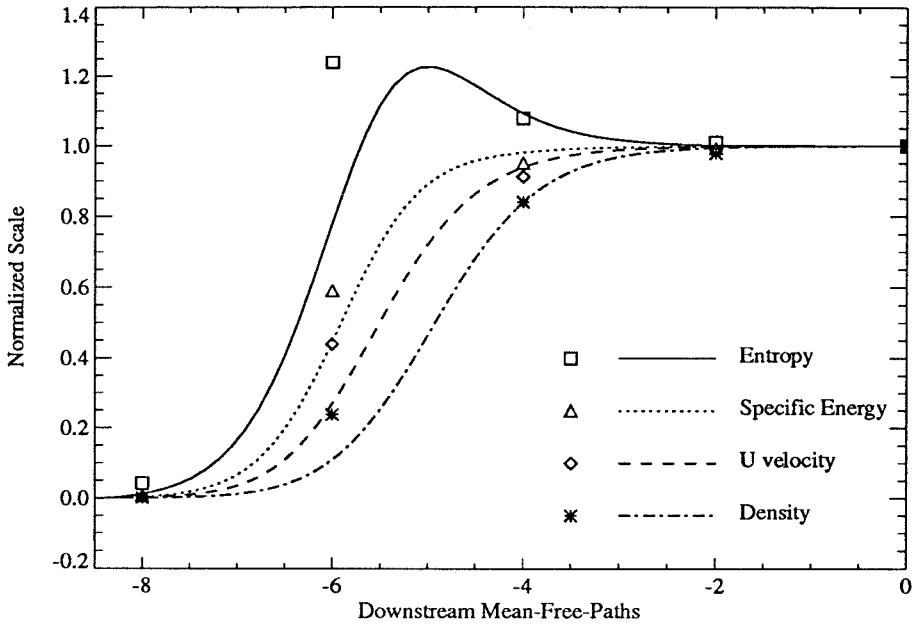

FIG. 5.5.1 A comparison of the exact profiles shown in Fig. 5.3.1 with those obtained due to inaccuracies of the equilibrium flow technique of chapter 3. The lines are the exact profiles and the symbols are from the equilibrium flow solver.

exact profile, again with a scaling of the x-axis to match the shock-thickness. A few points worth noting about the representation in the equilibrium flow technique is

1. The qualitative comparison to the exact solution is superb:
   - The overshoot in entropy is captured very well; the overshoot is quantitatively correct.
   - The relative positions of the entropy, specific energy, velocity and density profiles is correct.

2. The shock is spanned by just four computational points! In this context, it may be noted that with the solution scheme *via* odes discussed in this chapter, it is possible to fine-step through the profile with no considerations of the mean-free-path since this method is not kinetic in nature.

3. The comparison is in fact better than shown in Fig. 5.5.1, because the correct scaling

to use for the equilibrium flow technique is the *local mean free path*, as opposed to the downstream value used in the plot. This is because, as discussed in chapter 3, the grid spacing is a measure of the *local mean free path* in the method and there is a rather large variation of the mean free path from the upstream to the downstream.

CHAPTER 6

2-D Adiabatic Channel Flow

The viscous and compressible but laminar flow of a perfect gas through an adiabatic channel is not a fully understood problem. Its incompressible counterpart constitutes the Hagen-Poiseulle flow and is an exact solution of the Navier-Stokes equations. In this chapter, some approaches to the compressible case are examined. They fall into two categories: one using the nine-velocity lattice gas, described in Sec. 6.1 and the other starting with the Navier-Stokes equations and using the formulation of Broadwell (1952), described in Sec. 6.2.

6.1 The Lattice Gas Approach

There have been few instances of a full simulation of the problem of laminar compressible viscous channel flow. One of the problems is the imposition of the downstream boundary conditions. In this section, a simulation of the channel flow using the nine-velocity model* is described. The lattice gas method being a particle method, the imposition of the boundary conditions is simpler.

* Most of the description would be the same for any other model.

6.1.1 The Lattice Gas Computational Setup

Considering the simplicity of the problem, the picture in mind for the setup is a rectangular region of the nine-velocity lattice gas described in Sec. 1.2.2. The interaction of this system with the external surroundings is only through the perimeter of the rectangular region, considering the absence of external body forces. With flow along the longer dimension, the interactions along the shorter sides constitute the inflow-outflow boundary conditions and the interactions along the longer dimensions describe what happens on the channel walls.

The simulation of the wall boundary condition is simple. As was described in Sec. 1.2.2, the evolution of the lattice is a sequence of move and collide procedures. The wall is easily represented by modifying the collision processes at the lattice sites representing the wall. To examine the nature of collisions at a wall, consider a row of lattice sites representing a wall. Particles coming into this row of lattice sites can do so only because they have a component of velocity directed to the wall. Thus for example, in the nine-velocity model, only particle types 2, 3 and 4 (refer to Fig. 1.2.3) can arrive at the upper (north) wall of a channel. By defining how these particles are reflected back into the channel, the wall will be fully defined.

- The reflection can be defined to be specular: only the component of velocity perpendicular to the wall is reversed. In this case, the accommodation coefficient of the wall is zero, *i.e.*, flow properties parallel to the wall are unaffected by the wall. The flow velocity at the wall can be non-zero.
- The reflection can be defined to be bounce-back: The velocity of the particle impinging the wall is reversed. The accommodation coefficient in this case is two. This is a rather severe case of a wall wherein the particles bouncing off the wall do not do so in a random direction, but remember their incoming velocities and negate it on reflection.

A realistic wall** has an accommodation coefficient of unity and this can be easily achieved by uniformly but randomly choosing between the two types of reflection. This corresponds to a diffuse wall. Further, in both the specular and bounce-back reflection of particles at the wall, the particle-speeds are preserved and this ensures adiabaticity of the wall.

The inflow boundary condition is implemented through a reservoir. By reservoir is meant a body of fluid, used in the channel flow computation, but which is unaffected by the flow in the channel. The reservoir in the present case of a lattice gas flow is a small and independent, constantly updated region, periodic in the flow direction, located upstream of the actual channel and in a steady state. A particular lattice column of the reservoir† is assumed to be located immediately upstream of the channel entrance, so that particles at this lattice column directed downstream are introduced at the channel entrance the following time step. The particles at the channel entrance directed towards the reservoir are discarded at each time step.

The conditions in the reservoir can be manipulated independently to the required values. In the computations presented here, the upstream reservoir uses a mobius-strip like boundary condition for the walls parallel to the flow, and a periodic boundary condition in the flow direction, as introduced by Kadanoff *et al.* (1989). The flow in the upstream reservoir is sustained by imposing a body forcing, the level of which is adjusted to obtain the required flow rate. This generates a velocity profile which is parabolic for low forcing levels. Using this upstream boundary condition, the length of the channel that the flow takes to relax to the correct velocity profile from that at the inlet (due to the inflow from the upstream reservoir) is reduced‡.

** Physically, the bounce-back reflection is more unrealistic than the specular one in the following way: A perfectly flat wall will do the job of specular reflection where as to achieve bounce-back, a wall has to monitor the incoming particles and appropriately change contour. The consequence is perfect no-slip at the wall, an unphysical condition.

† since the reservoir is periodic in the flow direction.

‡ As compared to the length, required for the flow to adjust if the velocity profile across the channel at the inlet is

The outflow boundary condition is essentially an imposition of a downstream pressure[♯]. This is done at the last column of lattice sites representing the channel. That column is modeled as porous wall with the porosity depending inversely on the downstream pressure to be simulated. For a given pressure, the porosity of the wall at any time is uniform across the wall, but changes location at each time step to preclude the formation of any upstream patterns.

Fig. 6.1.1 is a schematic of the computational setup on a message passing multi computer. Considering the large aspect ratio of the domain (L/D of the channel), the multi-computer is configured as a linear array of processors along the flow direction. The computational domain is equally partitioned along the flow direction and the partitions assigned to the nodes (one computer of the multi-computer). There are no regions of overlap among the various nodes and the internode communication is limited to moving particles either leaving or entering the domain of the node appropriately. All the computations presented here were done with the Intel iPSC/860 GAMMA parallel machine, which consists of 64 nodes of iPSC/860 wired in a hypercube architecture. The communications in the present case were handled under a Reactive Kernel environment (Seitz *et al.* 1988). The sustained lattice site update rate for these computations, with the present implementation, was about a million sites a second.

The specification of the problem consists of prescribing the conditions in the upstream reservoir, the downstream pressure and an initial configuration for the channel. The lattice gas update procedure is then repeated till the flow in the channel attains a steady state, after which the flow is averaged over a sufficient number of time steps to obtain smooth data. Whether steady state has been achieved is determined by comparing profiles at different times and by examining the profile of a few quantities down the channel.

---

uniform.

♯ A variety of other outflow boundary conditions were studied too, omitted here for brevity.

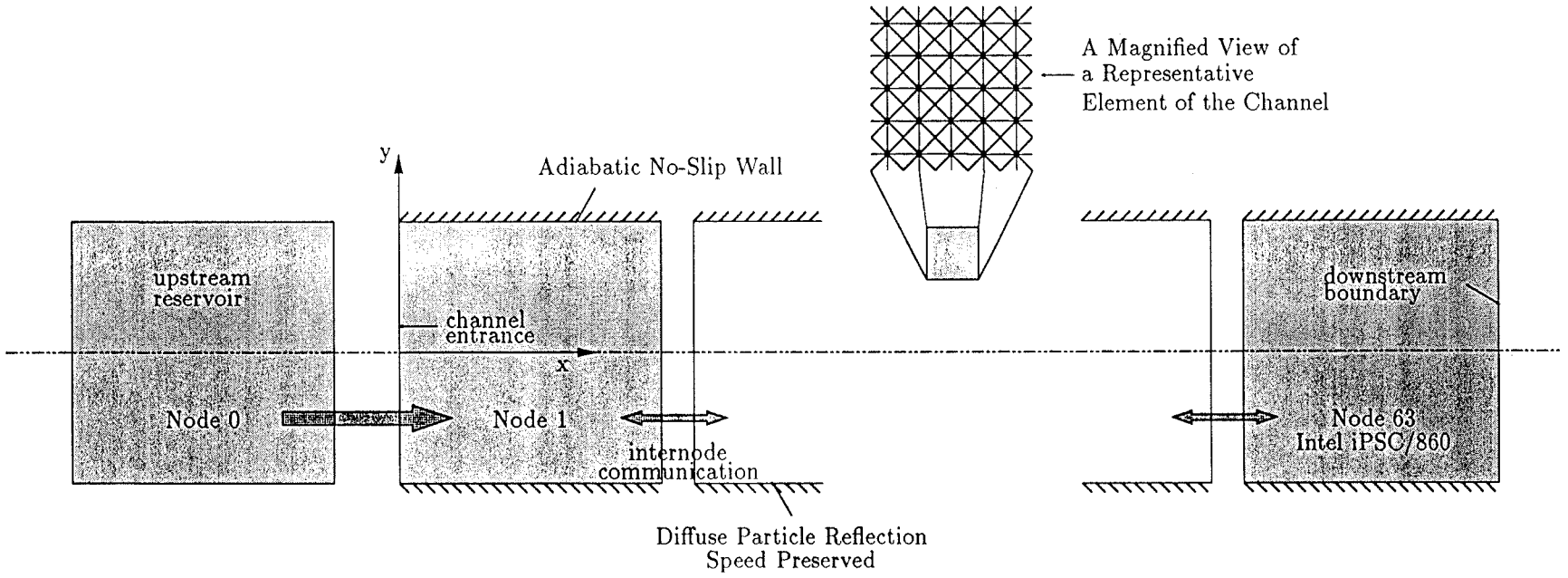
A Magnified View of
a Representative
Element of the Channel
y
Adiabatic No-Slip Wall
upstream
reservoir
channel
entrance
x
downstream
boundary
Node 0
Node 1
internode
communication
Node 63
Intel iPSC/860
Diffuse Particle Reflection
Speed Preserved

FIG. 6.1.1

6.1.2 The Simulations

The following is a description of a typical simulation using the lattice gas computation setup discussed above. The channel had a width of 256 lattice sites and a length to width ratio just less than 128. At an inlet density of about 2.5 particles per lattice site, the inlet Knudsen number is about 0.01. The conditions in the upstream reservoir were such that the centerline velocity at the inlet to the channel was about $0.127q$. At an inlet specific energy of $0.3q^2$, this corresponds to an equivalent inlet Mach number of 0.15*. As discussed in the chapter on Euler equations, the actual Mach number relates the given speed to the speed of propagation of a small disturbance at the given conditions. The equivalent Mach number however has no such significance for the lattice gas, it is simply defined as $\sqrt{\rho u^2/2p}$, in analogy to its definition for a perfect gas. The equivalent Mach number has been used for reasons of non-dimensionalization, as they are done for the Navier-Stokes equations in Eq. 6.2.2.

The downstream boundary condition is set to vacuum. The spatial averaging process to arrive at the macroscopic quantities is performed over a cell 512 lattice sites along the flow direction and 4 lattice sites across the channel. The procedure is run for about $16L$ time steps, corresponding to about 512,000 updates of each of the 4,000,000** lattice sites. The system has reached a steady state by this time and the updating procedure is continued for an additional period while data is accumulated to enhance smoothness of the final results. The results are presented as three dimensional plots of the concerned quantity against the length and width of the channel. All the quantities are normalized by the corresponding inlet quantities† : the velocity by the inlet centerline velocity, and the pressure and density by the width-averaged inlet values. The average across the width of the channel is projected

---

* The corresponding Mach number, M^-, as defined in Eq. 4.3.2 is 0.147.

** Since computation is done only for one half of the domain.

† except in Fig. 6.1.2b, where the u-velocity is normalized with respect to the local centerline u-velocity, and in Fig. 6.1.2g, where the v-velocity is normalized by q, the unit speed of the model.

onto the $y = 1.5$ plane and the inlet and outlet profiles are projected onto the $x = 1.5L/D$ plane. Fig. 6.1.2a,...,f shows the variation of the various quantities in the channel. The v-velocity is essentially zero, except near the exit, where the profile was as shown in Fig. 6.1.2g

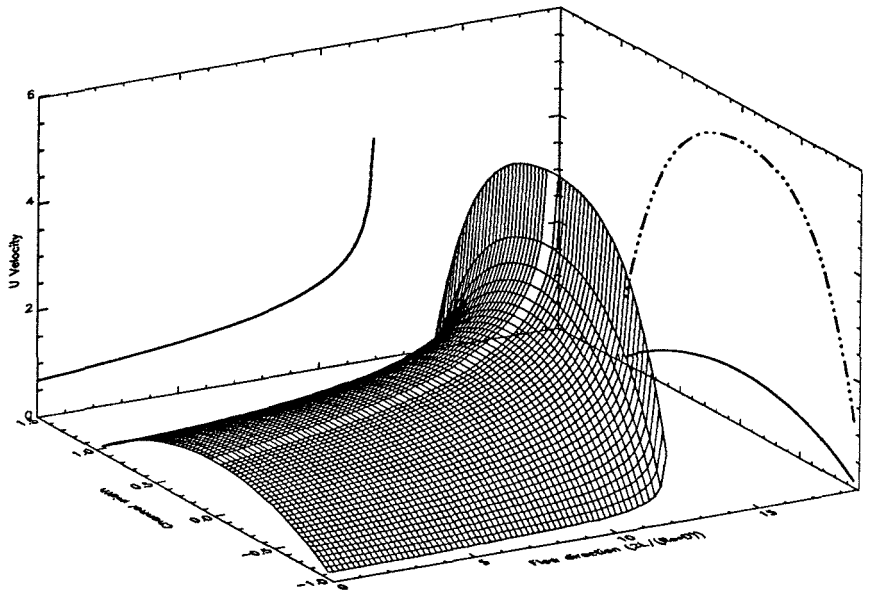

FIG. 6.1.2a The u-velocity across the channel and along the flow direction. It has been normalized by the centerline inlet velocity. The width-averaged u-velocity is projected on to the y=1.5 plane. The inlet and the exit velocity profiles across the channel are projected on to the x=18 plane.

Noteworthy features of this computation are

- The small acceleration of the flow at low velocities, picking up strongly at higher velocities (Fig. 6.1.2a). The last 50% of the increase in velocity is over about 12 widths of the channel (the full channel is 128 times the width).
- The flattening of the shape of the velocity profile across the channel, far downstream (Fig. 6.1.2b).
- The flatness of the pressure across the channel up to relatively high flow velocities (Fig. 6.1.2d).

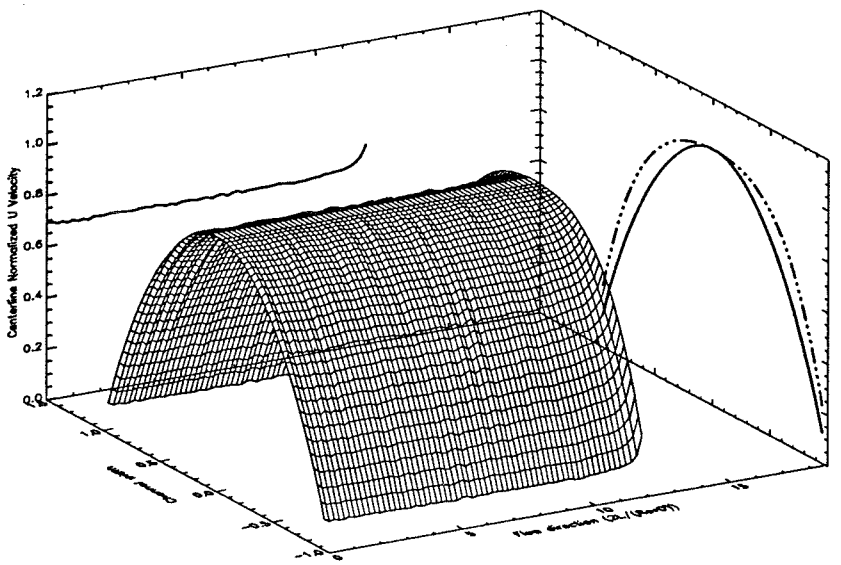

FIG. 6.1.2b The normalization is now with the local centerline velocity. This is done to show the evolution of the shape of the velocity profile down the channel, discounting the acceleration of the flow.

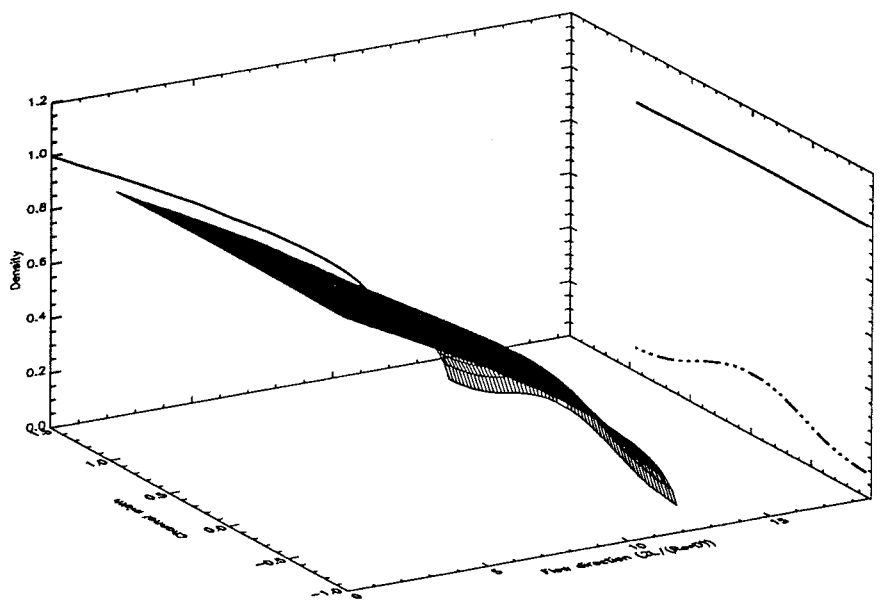

FIG. 6.1.2c A plot of density across and along the channel. Note the flatness across the channel at low velocities and the increasingly steep fall-off towards the exit of the channel.

- The linearity of the width-averaged pressure fall-off down the channel at low veloc-

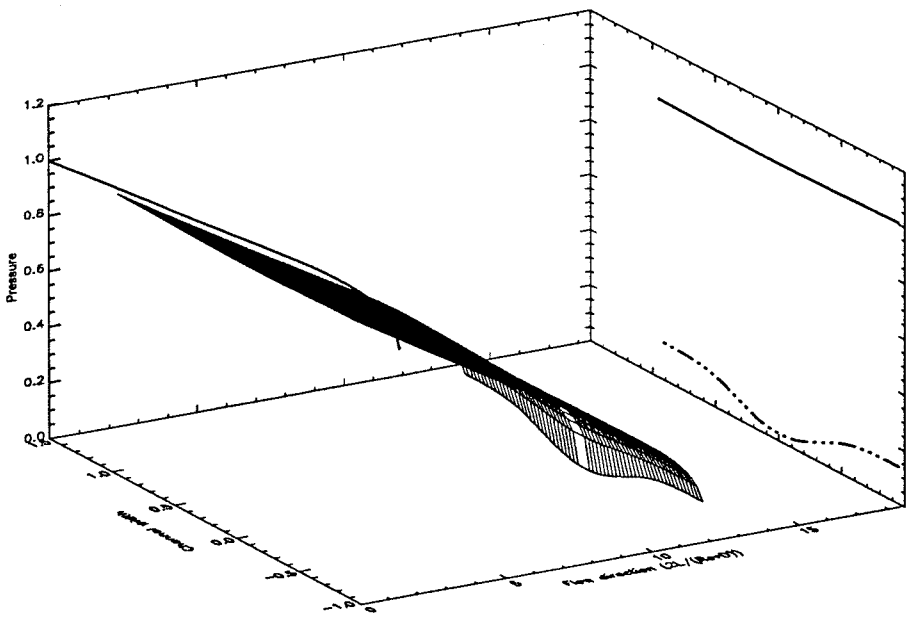

FIG. 6.1.2d The definition of pressure used is the one in Eq. 2.4.30, correct only to $O(u^2)$. The similarity to the density variations in Fig. 6.1.2c for the better part of the channel strongly suggests an isothermal behavior of the flow.

ities becoming increasingly non-linear at higher velocities (Fig. 6.1.2d).

- The close similarity of the width-averaged density and pressure profiles at low velocities (Fig. 6.1.2d & Fig. 6.1.2d).

- The confinement of the viscous effects to near the walls, as evidenced in Fig. 6.1.2e and Fig. 6.1.2f. The rise in entropy of the central core is mainly due to the falling density (See definition of entropy in Eq. B.0.4.

Fig. 6.1.3 shows the velocity along and across the channel, when the inlet velocity is higher, corresponding to an inlet centerline Mach number of 0.4. The minimum in the velocity profile downstream is rather unexpected and is an artifact of the model. Further discussion of the computation is deferred till some of the integral solutions of the Navier-Stokes equation for the problem are discussed.

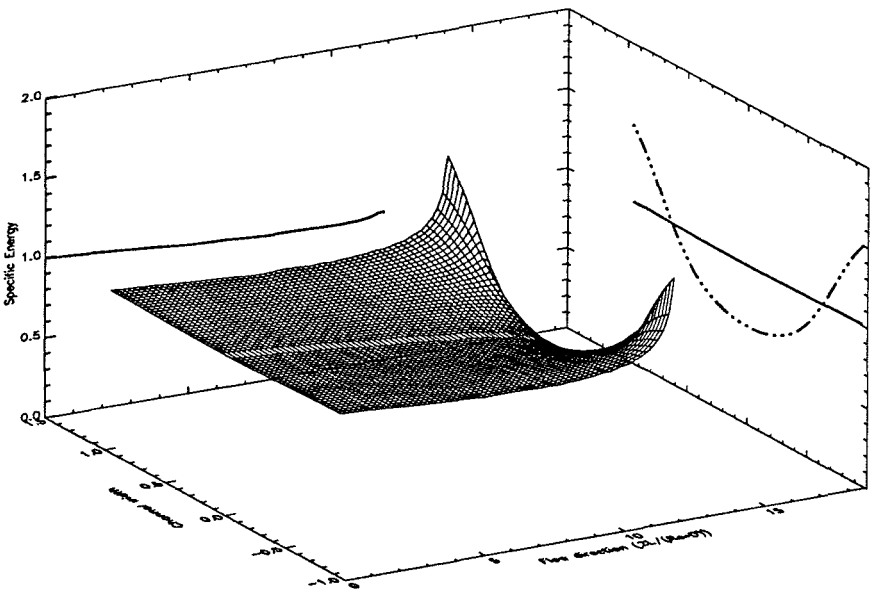

FIG. 6.1.2e The variation of specific energy in the channel shows that the flow is isothermal for most part of channel and that the heating is mostly near the walls. Note the width-averaged specific energy falling along the flow-direction, much like a Fanno flow.

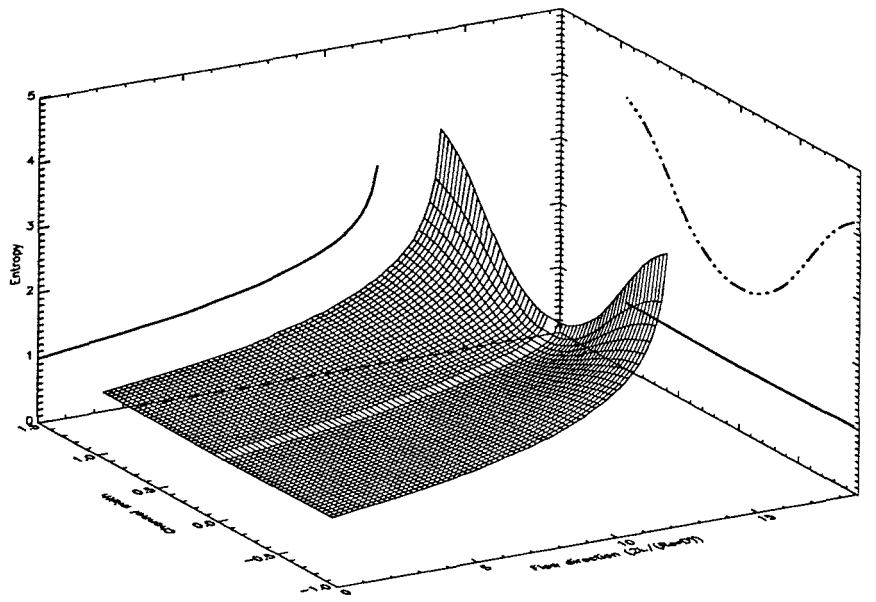

FIG. 6.1.2f The $n \log n$ based entropy variation, shows that most dissipation is in the wall region.

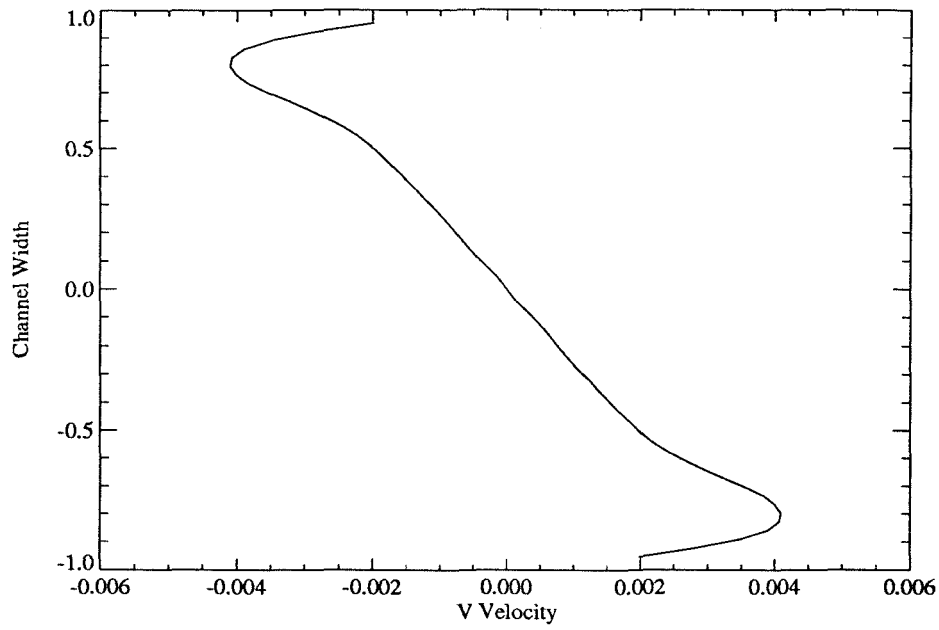

FIG. 6.1.2g The actual v-velocity near the exit of the channel. The v-velocity is almost zero elsewhere in the channel.

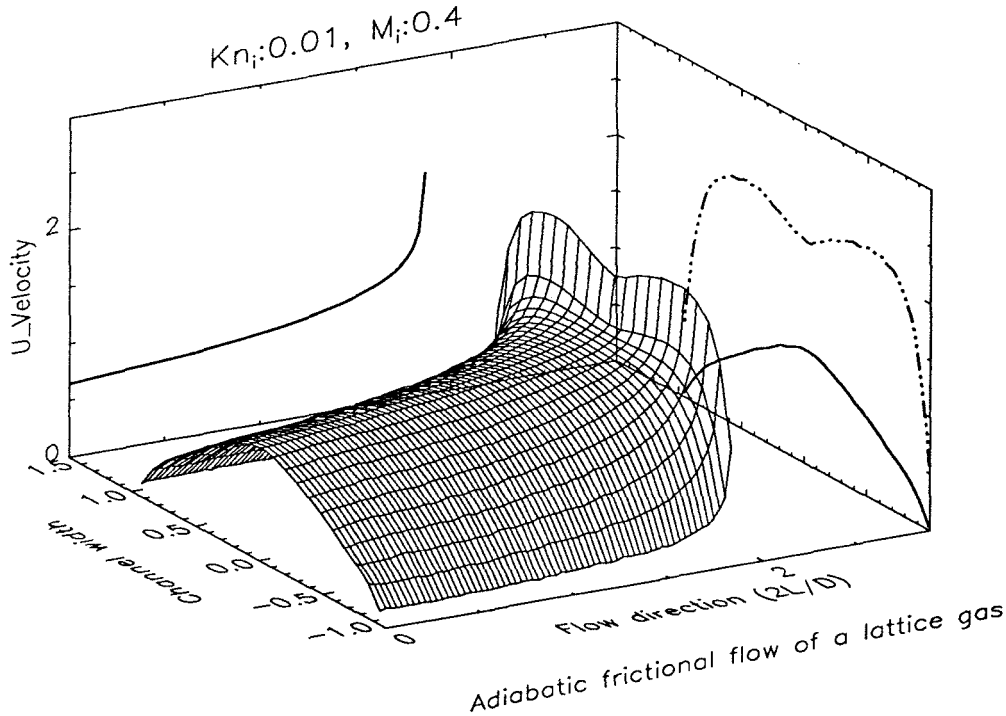

FIG. 6.1.3 When the flow velocities become close to the maximum allowed speed in the model, a minimum appears in the velocity profile at the center of the channel. This minimum is purely an artifact of the model.

6.2 Integral Solutions of the Navier-Stokes Equations

As stated earlier, the following formulation is due to Broadwell (1952). The numerical solutions of the resulting nonlinear ordinary differential equations are presented in Sec. 6.2.3, Sec. 6.2.4, and Sec. 6.3. In analyzing the results, some simple extensions of the original formulation are considered.

A steady, compressible, and laminar flow of a perfect gas between parallel straight walls which are adiabatic is considered. Under these conditions, it is reasonable to make a boundary-layer like approximation wherein

$$p = p(x); \qquad \frac{\partial^2 u}{\partial x^2} \ll \frac{\partial^2 u}{\partial y^2} \tag{6.2.1}$$

Under these assumptions, the mass, momentum and energy equations can be written in the non-dimensional form as

$$\begin{aligned} \frac{\partial \rho u}{\partial x} + \frac{\partial \rho v}{\partial y} &= 0 \\ \rho u \frac{\partial u}{\partial x} + \rho v \frac{\partial u}{\partial y} &= -\frac{1}{\gamma M_i^2}\frac{dp}{dx} + \frac{1}{Re_i}\left(\frac{\partial^2 u}{\partial y^2}\right) \\ \rho u \frac{\partial H}{\partial x} + \rho v \frac{\partial H}{\partial y} &= \frac{1}{Re_i}\frac{\partial}{\partial y}\left(\frac{1}{Pr}\frac{\partial H}{\partial y}\right) + \frac{1}{Re_i}\frac{\partial}{\partial y}\left(\left(1 - \frac{1}{Pr}\right) u \frac{\partial u}{\partial y}\right) \end{aligned} \tag{6.2.2}$$

Where the non-dimensionalizing quantities are the half-width of the channel $d/2$; the centerline inlet velocity u_i=$u(x$=$0,y$=$0)$; the width-averaged inlet density $\rho_i = \frac{1}{2}\int_{-1}^{1} \rho(x$=$0, y)dy$; and the inlet pressure p_i=$p(x$=$0)$. M_i is the centerline inlet Mach number and Re_i the inlet Reynold's number based on the half-width of the channel, the inlet centerline velocity and the width-averaged inlet density.

In using the above approximation, the mathematical nature of the governing partial differential equations — the Navier-Stokes equations — have been modified from being elliptic to now being parabolic. This was effectively a consequence of making diffusion in the problem significant only in one coordinate direction, the transverse direction. With this change, it is possible to look at the original boundary value problem as an initial

value problem in the flow direction, Numerically of course, this amounts to an enormous simplification of being able to march down the channel. A further simplification is to integrate Eq. 6.2.2 along the y-direction, so that the result is a set of nonlinear ordinary differential equations along the flow direction. But to be able to integrate over the width of the channel, we have to assume away part of the problem by prescribing the y-dependence of the velocity profile. This is done here by letting the velocity profile across the channel be a linear combination of few admissible functions. By admissible, is meant functions which in the present context satisfy the no-slip boundary condition at the walls and which are symmetric about y=0, the centerline of the channel. The admissible functions considered here are simply $(1-y^2)$, corresponding to the incompressible parabolic profile and $(1-y^4)$ & $(1-y^6)$ to allow for a flattening of the parabolic profile.

Since we are dealing with a perfect gas, the Prandtl number is of the order of unity, and further the effects of a variation in the Prandtl number are rather small. So, the Prandtl number is assumed to be unity in all future calculations. With $Pr = 1$, the energy equation admits constant H, $H = H_0$ as a particular solution. At this point, two distinctions are made, the low Mach number case and the general case.

6.2.1 The Low Mach Number Case

The energy equation can be rewritten as

$$\frac{T_0}{T} = 1 + \frac{\gamma+1}{2}M^2 \tag{6.2.3}$$

So that for $M \ll 1$, $T \approx T_0$, leading to the isothermal approximation‡. In this limit, the equation of state of a perfect gas becomes $p = \rho$. Eq. 6.2.2 now becomes

$$\frac{\partial pu}{\partial x} + p\frac{\partial v}{\partial y} = 0$$

‡ Using this approximation, of course, adiabaticity is violated to order u^2.

$$p\left(u\frac{\partial u}{\partial x}+v\frac{\partial u}{\partial y}\right)=-\frac{1}{\gamma M_i^2}\frac{dp}{dx}+\frac{1}{Re_i}\frac{\partial^2 u}{\partial y^2} \tag{6.2.4}$$

with $p(0)=1$, $u(0,y)$ prescribed and $u(x,\pm 1)=v(x,\pm 1)=0$. Integrating Eq. 6.2.4 and considering the symmetry about $y=0$,

$$p\int_0^1 u dy = c$$

$$\frac{d}{dz}\left(p\int_0^1 u^2 dy\right)=-\frac{1}{\gamma M_i^2}\frac{dp}{dz}+\left.\frac{\partial u}{\partial y}\right|_{y=1} \tag{6.2.5}$$

Here the flow direction has been rescaled with the inlet Reynolds number: $z=x/Re_i$ These are two integro-differential equations in the two variables p and u and not much progress can be made without further assumptions. Assuming $u(x,y)$ to be of the form

$$u(z,y)=\beta(z)(1-y^2)+\sigma(z)(1-y^4) \tag{6.2.6}$$

the integral equations reduce to

$$p(\beta+\frac{6}{5}\sigma)=c$$

$$\frac{8}{15}\frac{d}{dz}\left[p(\beta^2+\frac{16}{7}\beta\sigma+\frac{4}{3}\sigma^2\right]=-\frac{1}{\gamma M_i^2}\frac{dp}{dz}-2(\beta+2\sigma) \tag{6.2.7}$$

which now constitutes two equations in three variables, β, σ and p. To obtain a third equation, we can choose to satisfy Eq. 6.2.4 exactly at some points in the flow. This can be done only at the walls or on the centerline, considering that $v=0$ only at these locations.

We first consider the case where Eq. 6.2.4 are satisfied exactly on the walls:

$$\frac{dp}{dz}=\gamma M_i^2\left.\frac{\partial^2 u}{\partial y^2}\right|_{y=1} \qquad \text{giving} \qquad \frac{dp}{dz}=-2\gamma M_i^2(\beta+6\sigma) \tag{6.2.8}$$

The constant in the first of Eq. 6.2.7 depends on the entry conditions at the channel. To leave the entry conditions implicit in the formulation, the derivative of that equation is considered to form a set of three first order ordinary differential equations. This is cast in a form more convenient for numerical solution as

$$\frac{d\phi}{dz}=\mathbf{f}(\phi;M_i) \qquad \text{where} \qquad \phi=(p,\beta,\sigma) \tag{6.2.9}$$

In this form, it is a set of three autonomous nonlinear odes with the inlet Mach number as a parameter. The equations themselves are far too long and messy to be written explicitly and there is nothing new to be learnt from them.

If the differential equations Eq. 6.2.4 are instead satisfied exactly on the centerline of the channel,

$$p\left(u\frac{\partial u}{\partial z}\right)_{y=0} = -\frac{1}{\gamma M_i^2}\frac{dp}{dz} + \left.\frac{\partial^2 u}{\partial y^2}\right|_{y=0}$$

$$\text{giving} \qquad \frac{dp}{dz} = -\gamma M_i^2\left(2\beta + p(\beta+\sigma)\frac{d(\beta+\sigma)}{dz}\right) \tag{6.2.10}$$

and the Eq. 6.2.9 are appropriately modified.

On exactly the same lines, if $u(z,y)$ is assumed of the form

$$u(z,y) = \beta(z)(1-y^2) + \sigma(z)(1-y^4) + \delta(z)(1-y^6) \tag{6.2.11}$$

the requirement of two more equations[♯] forces us to satisfy Eq. 6.2.2 exactly at both the walls and the centerline. Eq. 6.2.9 would now be modified into a set of four autonomous equations.

6.2.2 The General or Non-Isothermal Case

Any of the above isothermal approximations would hold only in the limit $M \ll 1$. But there is no reason to suspect that the inequalities indicated in Eq. 6.2.1 would not hold when the Mach number is substantially greater than zero*. Therefore to look at higher M, we can retain the approximations in Eq. 6.2.1 but do better than an isothermal approximation. The energy equation $H = H_0$, can be written in the non-dimensional form in terms of temperature as $T = n - mu^2$, where $m = \frac{\gamma-1}{2}M_i^2$ and $n = 1+m$. This would combine with

---

♯ ?? are two equations in four variables — β, σ, δ, p.

* Removal of the approximations made in Eq. 6.2.1 would require full solution of the Navier-Stokes equations, greatly complicating the task.

the equation of state of a perfect gas to give $\rho(x,y) = \frac{p(x)}{n-mu^2(x,y)}$. The integral of Eq. 6.2.2 can then be written as

$$\int_0^1 \rho u dy = p\int_0^1 \frac{u}{n-mu^2}dy = c$$

$$\frac{d}{dz}\int_0^1 \rho u^2 dy = \frac{d}{dz}\left(p\int_0^1 \frac{u^2}{n-mu^2}dy\right) = -\frac{1}{N}\frac{dp}{dz} + \left.\frac{\partial u}{\partial y}\right|_{y=1} \tag{6.2.12}$$

Using the previous approximations for the velocity profiles does not permit an analytical evaluation of the integral on the left-hand-sides of the above equations. This is overcome by a change of independent variables from y to η, the transformation at a given z location given by

$$\eta = \int_0^y \rho(z,y)dy \tag{6.2.13}$$

$\eta(y=1)$ corresponds to the wall. Call it g to represent the wall in the new coordinates as

$$\eta = g(z) = \int_0^1 \rho(z,y)dy \tag{6.2.14}$$

The integral equations in the new coordinates are

$$\int_0^{g(z)} u d\eta = c$$

$$\frac{d}{dz}\int_0^{g(z)} u^2 d\eta = -\frac{1}{N}\frac{dp}{dz} + \frac{p}{n}\left.\frac{\partial u}{\partial \eta}\right|_{\eta=g(z)}$$

$$p = \int_0^{g(z)} (n-mu^2)d\eta \tag{6.2.15}$$

Where the last equation in the above set results from the transformation of the independent coordinate from y to η. Proceeding as in the previous section, we assume

$$u\left(z, \frac{\eta}{g(z)}\right) = \beta(z)\left(1-\left(\frac{\eta}{g}\right)^2\right) + \sigma(z)\left(1-\left(\frac{\eta}{g}\right)^4\right) \tag{6.2.16}$$

The extra equation again comes from satisfying the differential equations exactly either at the wall $\eta = g(z)$ or on the centerline $\eta = 0$. If the equations are satisfied exactly at the wall $\eta = g(z)$

$$\frac{dp}{dz} = \gamma M_i^2 \frac{p^2}{n^2}\left.\frac{\partial^2 u}{\partial \eta^2}\right|_{\eta=g(z)} \tag{6.2.17}$$

Or if the equations are satisfied exactly on the centerline of the channel $\eta = 0$

$$\left(\rho u \frac{\partial u}{\partial z}\right)_{\eta=0} = -\frac{1}{\gamma M_i^2}\frac{dp}{dz} + \left(\rho \frac{\partial}{\partial \eta}\rho \frac{\partial u}{\partial \eta}\right)_{\eta=0} \tag{6.2.18}$$

Again if the velocity representation was a sixth order polynomial as in Eq, the differential form of the momentum equations would have to be satisfied exactly both at the wall $\eta = g(z)$ and on the centerline $\eta = 0$ to get the requisite number of equations. The appendix lists the equations for the various cases. Numerical results from some of the schemes are presented. The different schemes of approximations considered: the isothermal and the non-isothermal cases, the fourth and the sixth order polynomial velocity profile representations, satisfying the momentum equations exactly on the centerline of the channel versus satisfying it on the walls, *etc.*are numbered as follows for convenience.

- Isothermal approximations
  - Fourth order velocity polynomial, satisfying the momentum equation exactly on the wall: **scheme 1a**
  - Fourth order velocity polynomial, satisfying the momentum equation exactly on the centerline: **scheme 1b**
  - Sixth order velocity polynomial, satisfying the momentum equation exactly both on the wall and on the centerline: **scheme 1c**

- The Non-Isothermal cases
  - Only **scheme 2a** corresponding to the fourth order velocity profile, satisfying the momentum equation exactly on the wall is considered.

6.2.3 Relaxation of the Velocity Profile

The ordinary differential equations developed in the previous section describe to a certain approximation the evolution of a laminar, compressible, and viscous flow down a channel. Presently, the velocity profile at the entry to the pipe is set to a rather unphysical shape — the profile has a minimum on the centerline — and the evolution of this profile under the above approximation is examined. The inlet Mach number is set to 0.1.

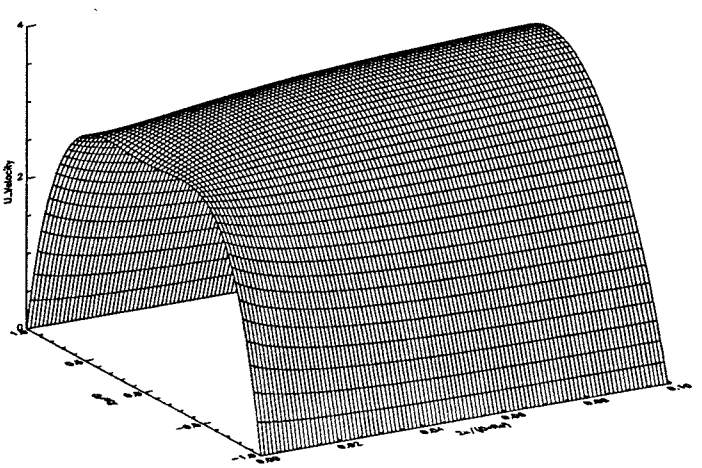

FIG. 6.2.1 The relaxation of a velocity profile with a minimum on the centerline at the inlet to the channel to a preferred shape, which in this case is nearly parabolic. The inlet Mach number is 0.1

Fig. 6.2.1 shows that the profile relaxes in a very short length of the pipe to a nearly parabolic profile. Fig. 6.2.2 shows the same in terms of the shape parameters β and σ. A non-zero σ corresponds to a deviation from the parabolic profile.

Scheme 1a was used here (isothermal approximation with a fourth order velocity profile representation). The relaxation in the other schemes to the preferred shape of the velocity profile at low Mach numbers is similar.

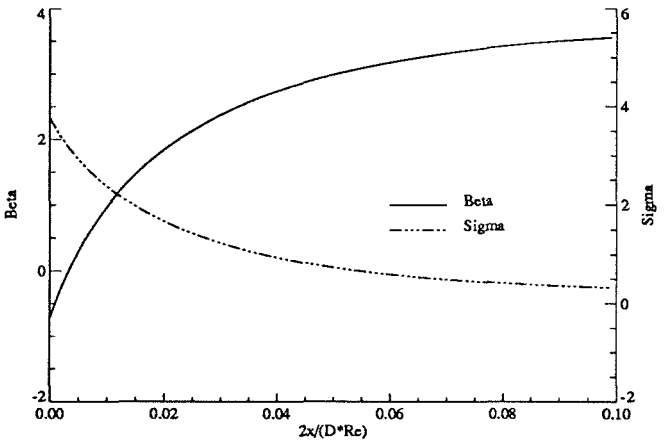

FIG. 6.2.2 The relaxation is shown here in terms of β and σ. $\sigma = 0$ corresponds to a parabolic profile

6.2.4 The Width-Averaged Quantities

In this section, the variation of the width-averaged quantities down the channel using the above-mentioned schemes are compared. Before presenting the numerical results, considering that these schemes are integral in nature, one can expect that there are going to be significant differences in these comparisons only between the isothermal and non-isothermal cases. The explanation is that the specific nature of the variation across the channel is essentially integrated out of the formulation.

Fig. 6.2.3 shows the variation of pressure down the channel for four different schemes: **schemes 1a, 1b, 1c, 2a.**

Some of the features as revealed in these plots are

1. In all the approximation schemes, the pressure drop at low Mach numbers is linear, becoming increasingly non-linear at higher Mach numbers.

2. The pressure profile down the channel for the three different isothermal schemes are virtually identical. Thus the order of the velocity profile and whether the momentum equation is satisfied exactly on the centerline or on the wall does not

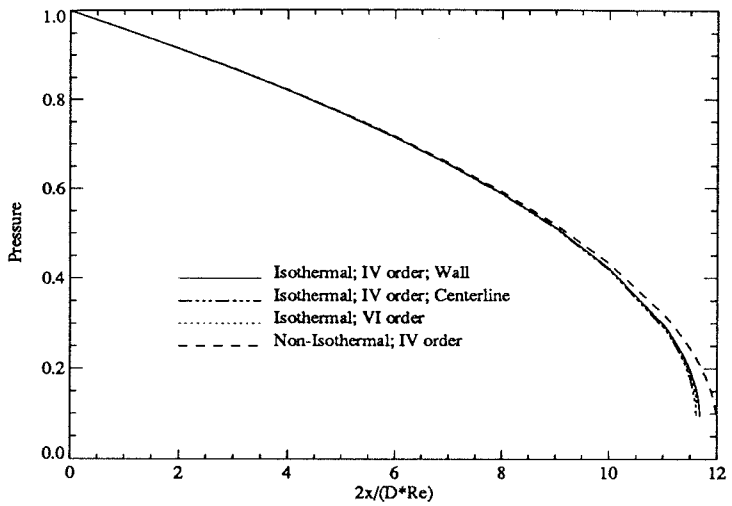

FIG. 6.2.3 The variation of pressure along the length of the channel

seem to affect the pressure variation.

3. The deviation of the isothermal approximation from the non-isothermal case is only in the high-subsonic regime and even there, the deviation is small.

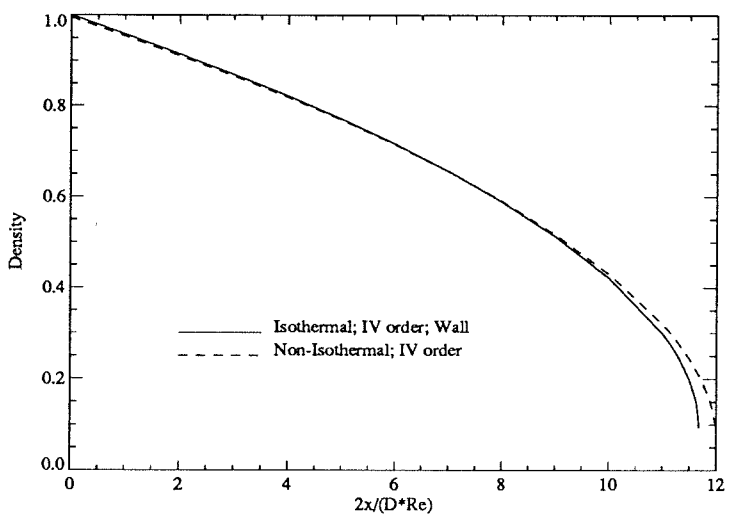

FIG. 6.2.4 The width-averaged density along the length of the channel

Fig. 6.2.4 is the corresponding picture of the density variation down the channel. Since in the isothermal approximation $p = \rho$, only **scheme 1a** and **scheme 2a** are compared. The

two curves are remarkably close, with departures again confined to the high-subsonic region. The interesting feature of these plots however is the relative slopes of the pressure and density curves in the low Mach number region. As seen in Fig. 6.2.3 and Fig. 6.2.4, the slopes are the same. This is in contrast to what one might have expected — an incompressible Poiseulle like flow. The explanation for this is as follows: Poiseulle flow, corresponding to incompressible flow in a channel, is a singular limit off the present problem, the compressible channel flow. The singular limit is attained at $M = 0$. In that limit, the pressure gradient is *external, imposed* — the velocity profile has the pressure gradient as a free parameter

$$u \propto -\frac{dp}{dz}(1 - y^2) \tag{6.2.19}$$

This is unlike in the compressible case, however small the Mach number, where the pressure gradient is part of the solution. Just as singular limits are thought of as the loss of a solution when the parameter takes on the limiting value, in the present case, the singular incompressible limit can be thought of as the loss of thermodynamics-as-a- degree-of-freedom from the compressible solutions on letting the Mach number be zero identically. This explains why the pressure gradient appears as a free parameter in the Poiseulle flow and as part of the solution in the compressible flow. In the compressible flow, even at $M = \epsilon$, the flow is driven by viscous dissipation which causes the density to fall and this results in a lower pressure according to the equation of state $p = \rho T$. It is important to note that while heating due to viscous dissipation is only a second order effect, the variation of density due to viscous dissipation is of first order.

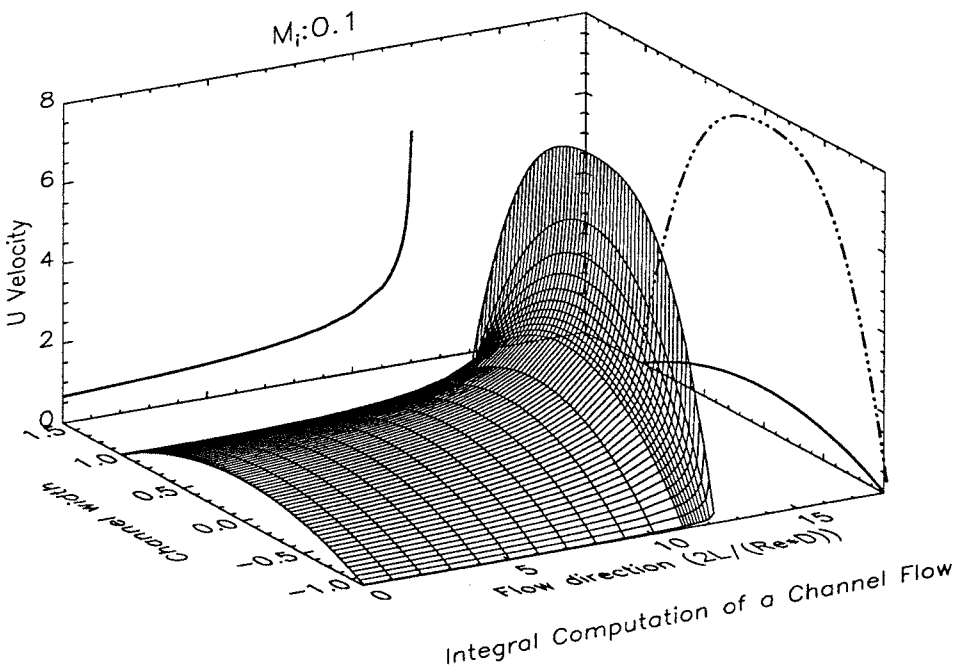

FIG. 6.3.1a The u-velocity across the channel and along the flow direction. It has been normalized by the centerline inlet velocity. The width-averaged u-velocity is projected on to the y=1.5 plane. The inlet and the exit velocity profiles across the channel are projected on to the x=18 plane.

6.3 Comparison of the Integral Solution to the Lattice Gas Simulation

Scheme 2a is used to obtain the integral solution of the problem, the simulation of which using the nine-velocity model, was presented in 6.1. In the present context, the problem is defined by fixing the inlet Mach number M_i at 0.15 and setting the specific heat ratio of the gas, γ, equal to 2. Fig. 6.3.1a,...,d presents the variation of the velocity, density, and pressure in the channel.

The qualitative comparisons of the flow — Fig. 6.1.2a,...,d and Fig. 6.3.1a,...,d — are good. The width-averaged pressure and u-velocities for the two cases are compared in Fig. 6.3.2

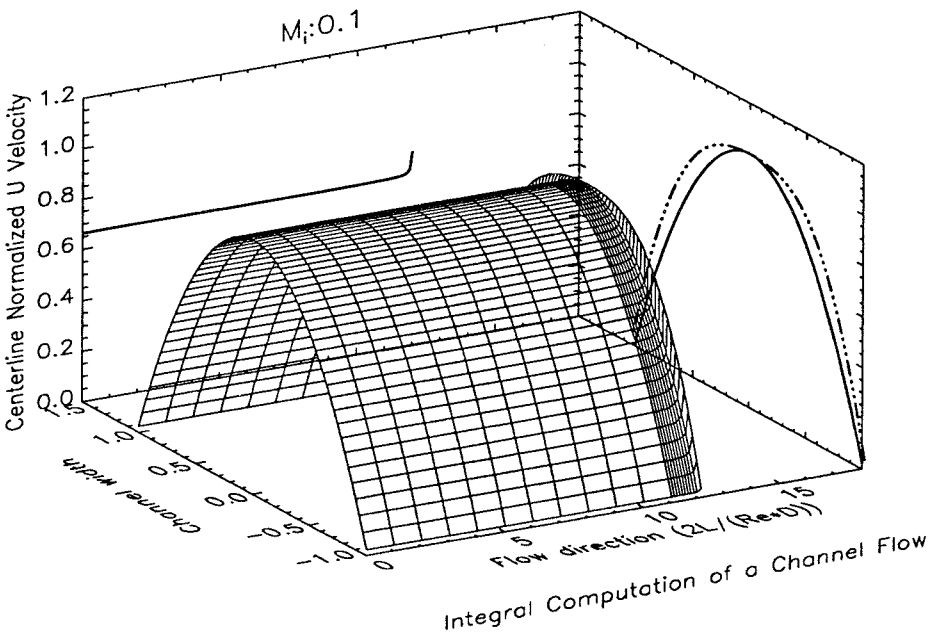

FIG. 6.3.1b The normalization is now with the local centerline velocity. This is done to show the evolution of the shape of the velocity profile down the channel, discounting the acceleration of the flow.

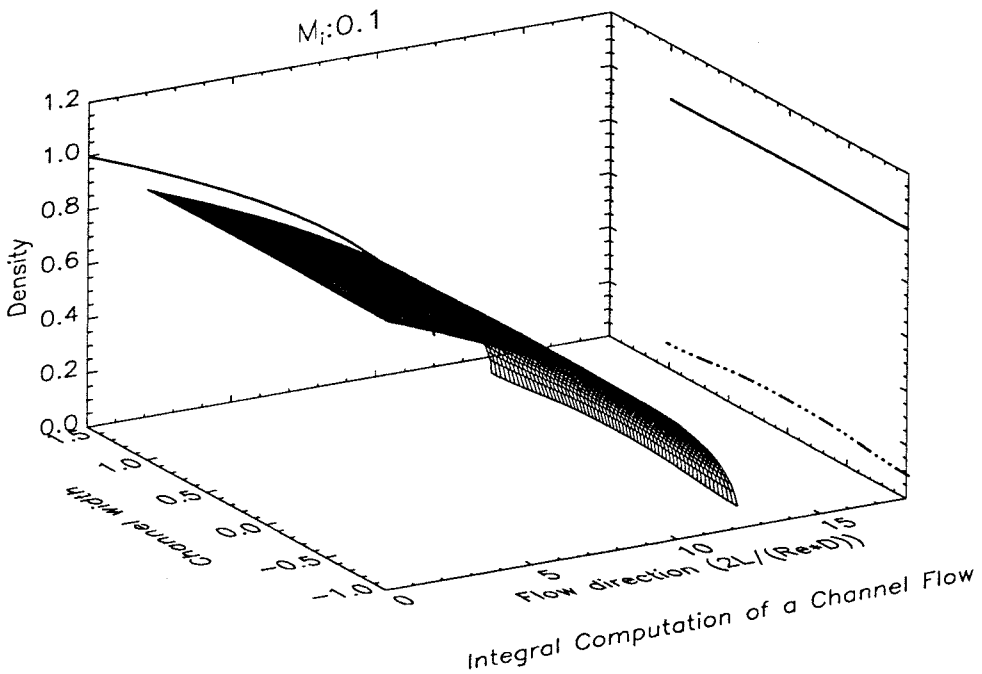

FIG. 6.3.1c A plot of density across and along the channel. Note the increasingly faster fall-off of the density towards the exit of the channel. The variations across the channel are small and confined to the regions close to the exit.

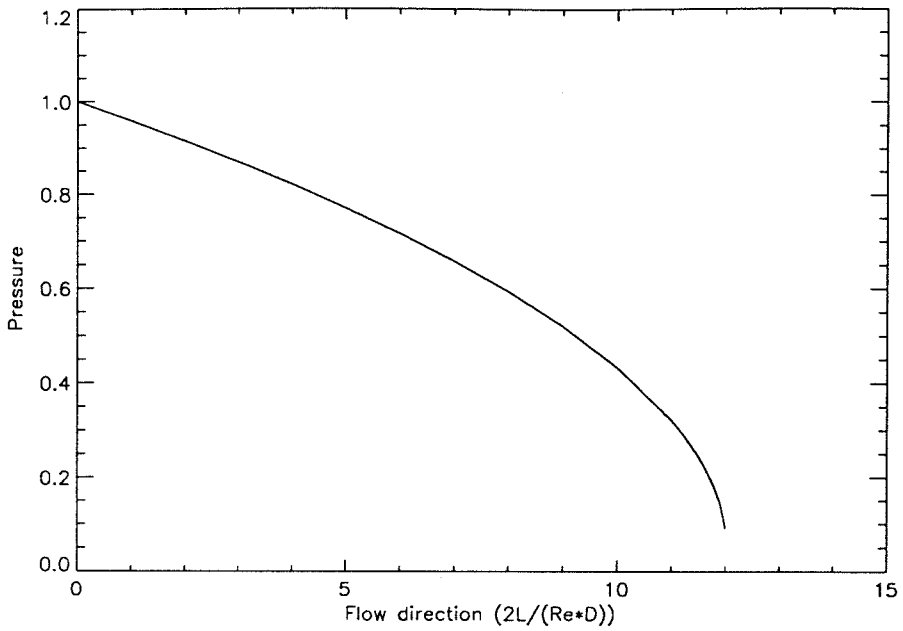

FIG. 6.3.1d The pressure does not vary with the cross-section in this approximation. The isothermal behavior discussed earlier is apparent by comparing the pressure variation here to the width-averaged density variation in Fig. 6.3.1c

6.3.1 The Spurious Minimum in the Velocity Profile

The approximations that have been made in the course of arriving at these schemes essentially limit their range of applicability. We have made three major assumptions:

1. The boundary-layer like assumption of Eq. 6.2.1 is most like to fail at high Mach numbers, mainly because of $\frac{\partial^2 u}{\partial x^2}$ becoming comparable to $\frac{\partial^2 u}{\partial y^2}$. The variation of pressure across the channel is also likely to become significant close to the sonic station, since a curvature of the streamlines is essential there. But this is expected to occur further downstream than when $\frac{\partial^2 u}{\partial x^2}$ becomes comparable to $\frac{\partial^2 u}{\partial y^2}$. Besides the assumption, $p = p(x)$, does not by itself proscribe a curvature of the streamlines.

2. The isothermal approximation is likely to breakdown earlier than the above because of significant heating caused by viscous effects which drive the flow.

3. Finally, the order of the polynomial used to represent the velocity profile may lack

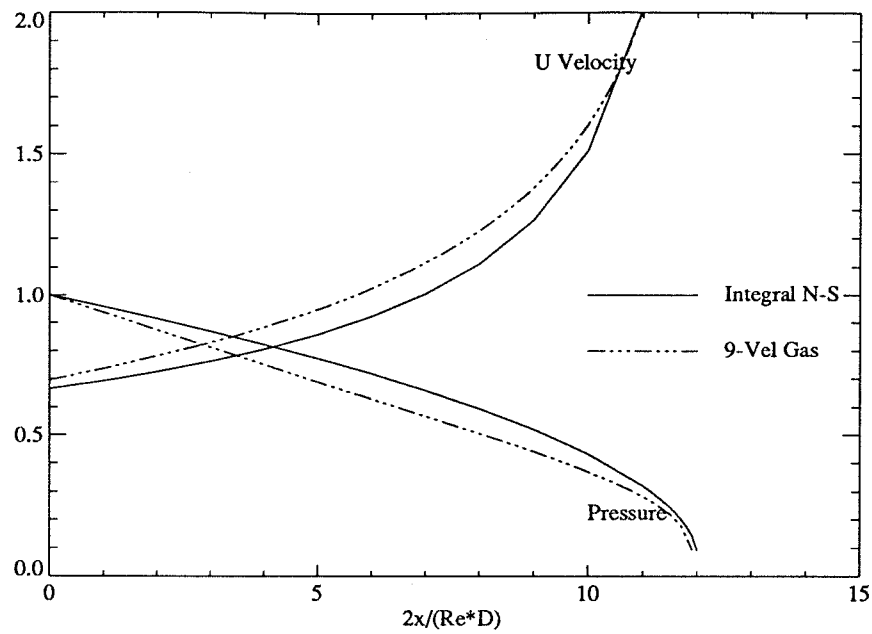

FIG. 6.3.2 The width averaged variation of quantities in the integral formulation are expected to be good approximations to the exact values. The qualitative agreement of the nine-velocity gas simulations indicates that the phenomenology in the two cases is much the same.

sufficient flexibility and give rise to rather unphysical shapes of the velocity profile.

If the integral solution computation** in 6.3 is continued further down the channel, a minimum develops in the velocity profile†. This minimum in the velocity profile, even though at a relatively high Mach number, does not seem physical. To see if the minimum in the velocity profile is only an artifact of the representation used for the velocity profile, the calculation is repeated‡ with a sixth order polynomial for the velocity (**Scheme 1c**). The computations now reveal two minima in the velocity profile, thus confirming the fact that the minimum (or minima, as the case may be) is only a consequence of the insufficiency of the velocity profile representation used. That is to say, the profiles across the channel,

** the scheme used is the non-isothermal, fourth order velocity representation, with the momentum equations satisfied exactly at the walls.

† Repeating the calculation with the isothermal approximation, gives essentially identical results.

‡ Only the isothermal approximation is used. The non-isothermal approximation is expected to give very similar results, from what has been discussed above.

as obtained from these schemes, become unphysical beyond a certain Mach number. After a number of runs, it is seen that while **schemes 1a** and **2a**, which satisfy the momentum equation exactly on the walls, develop a minimum in the velocity-profile on the centerline, **scheme 1b** which satisfies the momentum equation exactly on the centerline does not do so. This, however, is of little interest since these approximate schemes are unlikely to be applicable this far down the channel.

6.4 Discussion

The qualitative comparison of the lattice gas to the integral solutions of the Navier-Stokes equations are good, when the flow Mach numbers below about 0.6. The lattice gas method shows a minimum in the velocity profile, when the flow speeds approach the maximum speed allowed in the model. Also the integral methods, both the isothermal and non-isothermal approximations, with a IV order velocity profile representation, developed a minimum in the velocity profile at Mach numbers close to 1. But the minimum in the lattice gas method and the minimum in the integral computation are unrelated, and are only artifacts of the model used or of the order of the velocity representation used.

The Fig. 6.4.1 shows an ad-hoc comparison of the two dimensional channel flow process on the pressure-specific volume plane. Again the definition of pressure used for the lattice gas is the one in Eq. 2.4.30, correct only to $O(u^2)$. The over-riding factor, however, is the density contribution to pressure. While the comparison may initially seem surprisingly good, a moments reflection shows that it mainly because of the isothermal nature of the flow.

In this context, it should be pointed out that a number of investigators (*e.g.*, Kadanoff *et al.* 1989) have asserted their verification of the incompressible Poiseulle flow, in the context of lattice gas simulations. As is clear from the present chapter, the claims are at best a

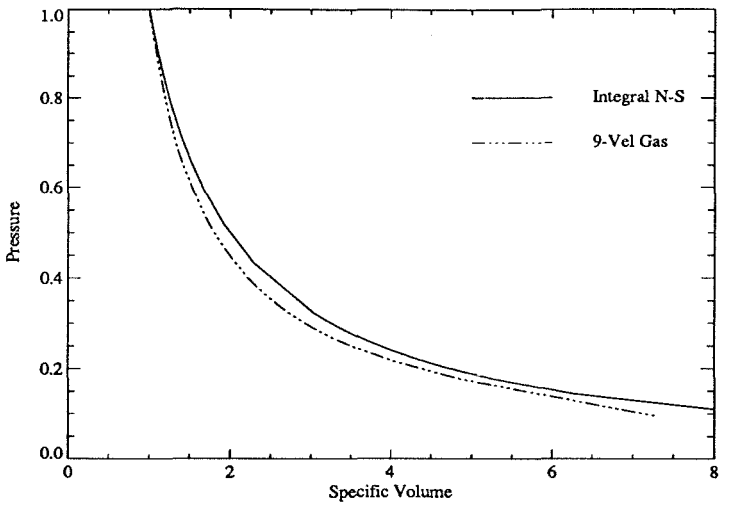

FIG. 6.4.1 An *ad-hoc* comparison of the two schemes for the adiabatic channel flow on the $p - v$ plane.

sloppy usage of the term *incompressible*, because the flow is clearly compressible — it is *isothermal* upto relatively high Mach numbers.

Finally, the breakdown of the both the methods at Mach numbers higher than about 0.6, make the study incomplete, since the flow field in the vicinity of the sonic region is expected to be of considerable interest. While the use of a discrete-velocity model with more number of velocities, say 25, may allow studying the flow field near the sonic region better, a definitive study of the problem would involve either the solution of the full compressible Navier-Stokes equations or a use of the Direct Simulation Monte-Carlo technique (Goldstein 1992).

References

Bird, G. A. 1976 Molecular Gasdynamics, Clarendon, Oxford, UK

Broadwell, J.E. 1952 On Compressible Laminar Flow in Ducts, Ph.D Thesis, University of Michigan

Broadwell, J.E. 1964a Study of Rarefied Shear Flow by the Discrete Velocity Method, *J. Fluid Mech.* **19**, 401

Broadwell, J.E. 1964b Shock Structure in a Simple Discrete Velocity Gas, *Phys. Fluids* **7**, 1243

Caflisch, R. E. 1979 Navier-Stokes and Boltzmann Shock Profiles for a Model of Gas Dynamics, *Comm. Pure App. Math.* **32**, 521

Cercignani, C. 1988 The Boltzmann Equation and Its Applications (Springer, Berlin)

Chen, S., Lee, M., Zhao, K. H., & Doolen, G. D. 1989 A Lattice Gas Model with Temperature, *Physica D* **37**, 42

Cornille, H. 1991 Temperature Overshoots for Multispeed Discrete Boltzmann Models, *Phys. Lett. A* **154**, 339

d'Humières, D. & Lallemand, P., 1989 *Private communication.*

d'Humières, D. & Lallemand, P., 1986 2-D and 3-D hydrodynamics on lattice gases, *Helv. Phys. Acta* **59**, 1231

Doolen, G., ed. 1989 Lattice Gas Methods for PDE's (Addison-Wesley, Reading, MA).

Doolen, G., ed. 1991 Lattice Gas Methods for PDE's Theory, Applications and Hardware *Physica D* **47**

Frisch, U., Hasslacher, B., & Pomeau, Y. 1986 Lattice-gas automata for the Navier-Stokes equation, *Phys. Rev. Lett.* **56**, 1505

Gatignol, R. 1975 Théorie Cinétique des Gaz à Répartition Discrète de Vitesses Lecture Notes in Physics (Springer-Verlag, Berlin) **36**

Gilbarg, D., & Paolucci, D. 1953 The Structure of Shock Waves in the Continuum Theory of Fluids, *J. Rat. Mech. Anal.* **2**, 617

Goldstein, D., 1992 *Private communication.*

Hardy, J. & Pomeau, Y. 1972 Thermodynamics and Hydrodynamics for a Modeled Fluid *J. Math. Phys.* **13**, 1042

Hardy, J., de Pazzis, O., & Pomeau, Y. 1976 Molecular Dynamics of a Classical Lattice Gas: Transport Properties and Time Correlation Functions, *Phys. Rev. A* **13**, 1949

Inamuro, T., & Sturtevant, B. 1990 Numerical Study of Discrete-Velocity Gases, *Phys. Fluids A* **2**, 2196

Kadanoff, L., McNamara, G., & Zanetti, G. 1989 From Automata to Fluid Flow: Comparisons of Simulation and Theory, *Phys. Rev. A* **40**, 4527

Lax, P.D. 1986 On Dispersive Difference Schemes, *Physica D* **18**, 250

Macrossan, M. N. 1989 The Equilibrium Flux Method for the Calculation of Flows with Non-Equilibrium Chemical Reactions, *J. Comp. Phys.* **80**, 204

Maxwell, J.C. 1890 Scientific Papers II, Cambridge University Press, Cambridge.

McNamara, G. R., & Zanetti, G. 1988 Use of the Boltzmann Equation to Simulate Lattice-Gas Automata, *Phys. Rev. Lett.* **61**, 2332

Moody, D.M., & Sturtevant, B. 1984 Shock Waves in Superfluid Helium *Phys. Fluids* **27**, 1125

Nadiga, B.T., Broadwell, J.E. & Sturtevant, B. 1989 A Study of a Multispeed Cellular Automaton, Rarefied Gas Dynamics: Theoretical and Computational Techniques, Vol **118** of Progress in Astronautics and Aeronautics ISBN 0-930403-55-X, 155.

Press, W.H, Flannery, B.P., Teukolsky, S.A., & Vetterling, W.T. 1988 Numerical Recipes in C (Cambridge University Press) ISBN 0-521-35465-X, 91

Pullin, D. I. 1980 Direct Simulation Methods for Compressible Inviscid Ideal-Gas Flow, *J. Comp. Phys.* **34**, 231

Rothman, D. H., 1989 Negative-viscosity lattice gases, *J. Stat. Phys.* **56**, 1119

Seitz, C.L., Seizovic, J., & Su, Wen-King 1988 The C Programmers's Abbreviated Guide to Multicomputer Programming **Caltech-CS-TR-88-1**

Succi, S., Benzi, R., & Higuera, F. 1991 The Lattice Boltzmann Equation: A New Tool for Computational Fluid Dynamics, *Physica D* **47**, 219

Van Leer, B. 1979 Towards the Ultimate Conservative Difference Scheme. V, *J. Comp. Phys.* **32**, 101

von Neumann, J., 1949 The general and logical theory of automata, in *J. von Neumann, Collected works 5, 1949* edited by A. H. Taub, 288.

Whitham, G.B., 1959 Some comments on wave propagation and shock wave structure with application to magnetohydrodynamics. *Comm. Pure Appl. Math.* **12**, 113

Whitham, G.B., 1974 Linear and Nonlinear Waves Wiley-Interscience, ISBN 0-471-94090-9

Wolfram, S. 1986 Cellular Automaton Fluids 1: Basic Theory, *J. Stat. Phys.* **45**, 471

Yee, H. C. 1989 A Class of High-Resolution Explicit and Implicit Shock-Capturing Methods NASA-TM **101088**

Zanetti, G. 1989 Hydrodynamics of Lattice-Gas Automata, *Phys. Rev. A* **40**, 1539

APPENDIX A

Entropy and Temperature

Employing the method of most probable distributions, we consider a function Ω which measures the probability of occurance of a particular state identified by the velocity distribution and spatial distribution of particles, for a given macrostate. The function Ω would then depend on ρ, e, and also on u, in view of the Galilean non-invariance of discrete-velocity-gases. The particles in the model as defined above, do not have an interaction potential and hence the gas is ideal. Consider a set of N particles taking on the allowed discrete velocities in the model populating V lattice sites in the physical space to be the system. The system is then fully described macroscopically by prescribing its specific internal energy, e, and the velocity, $\mathbf{u}$. The N particles can be distributed in the velocity space (over the allowed b discrete velocities) and the physical space (over the V lattice sites) in various different ways. Considering any one such configuration, the function Ω measures the multiplicity of equivalent micro-configurations possible because of the indistinguishibility of particles with the same velocity. Looking first at the distribution of the particles in the physical space alone, it is clear that the state which has the highest multiplicity is one in which the N particles are uniformly distributed over the V lattice sites.

$$\chi_{phy} = \frac{N!}{\prod_{j=1}^{V} N_j!} \tag{A.0.1}$$

where N_j is the number of particles in lattice site j and it is maximized when the N_j, $j = 1, \ldots, V$ are all equal. Then looking at the distribution of the particles in the velocity space, proceeding on similar lines but noting the additional constraints of the specified energy and velocity,

$$\chi_{vel} = \frac{N!}{\prod_{i=1}^{b} N_i!} \tag{A.0.2}$$

where the N_i is the number of particles with velocity $\mathbf{c_i}$ and the N_i satisfy

$$\frac{\sum_1^b \mathbf{c_i} N_i}{\sum_1^b N_i} = \mathbf{u}$$

$$\frac{\sum_1^b |\mathbf{c_i}'|^2 N_i}{\sum_1^b N_i} = e \tag{A.0.3}$$

The maximization of $ln(\chi_{vel})$ is achieved as noted in the section on equilibrium state when the N_i is the discrete-Maxwell-Boltzmann distribution. Then using Stirling's formula, the specific entropy can be written in terms of other specific quantities as

$$s = -\frac{1}{\rho} \sum_0^b n_i ln(n_i) \tag{A.0.4}$$

where n_i is the equilibrium discrete Maxwell-Boltzmann distribution which depends on e and u.

To better understand the nature of entropy, we consider the flow of the nine-velocity gas in the direction of one of the slow moving particles.

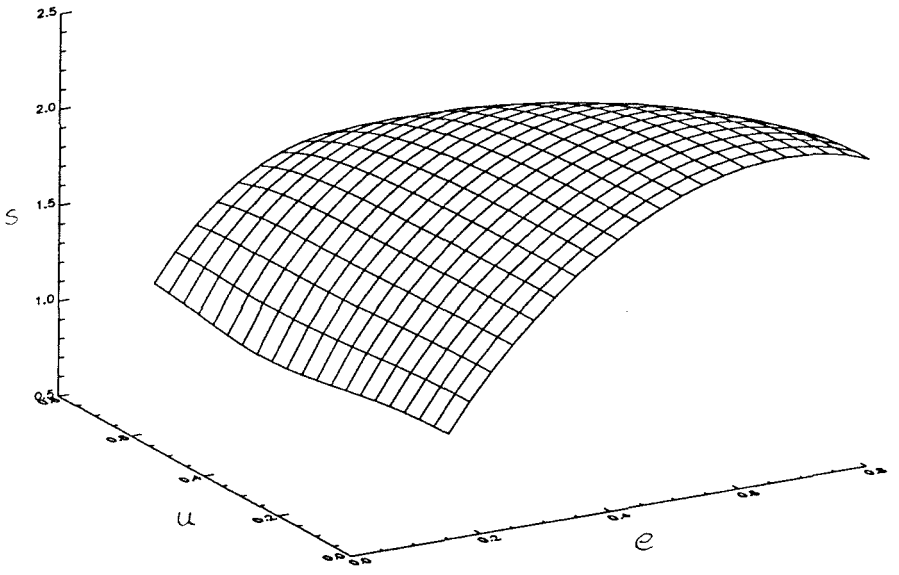

FIG. A.1 Variation of specific entropy with specific internal energy and velocity at constant density.

Two points noteworthy of the above plot are: At a constant flow velocity, the entropy is **not** a monotonic function of e, unlike in an ideal gas. At a constant e, the entropy depends on the flow velocity and decreases with increasing u, again much unlike an ideal gas. Finally, it is expected that though the surface of s in the e-u plane is convex, in any spontaneous process, the entropy will only increase, *i.e.* there will not be a crossover from one side to another in Fig. In a given process, the entropy may decrease as viewed in the e-u plane, but there is the additional dependence of s on ρ.

The definition 1.1.1 for the specific internal energy, e, has been used at times previously for temperature, because of the resemblance to the kinetic definition of temperature of ideal gases. The problem in the context of discrete velocity gases is that the velocity set is finite and therefore such a definition of temperature is, in general, incompatible with the thermodynamic definition. The thermodynamic definition of temperature is given by Thus from Fig Eq. 3.2.5 it is clear that the temperature in the nine-velocity gas and discrete-velocity gases in general can be negative. The situation here is very similar to other cases where the phase space is finite as for example in the case of spin systems.

APPENDIX B

ODEs from the Integral Formulation of the Adiabatic Channel Flow

The resulting ordinary differential equations for both the isothermal and the non-isothermal cases are given here for a sixth order velocity profile

B.1 Isothermal Case

The integrated continuity and momentum equations are

$$p(\frac{2\beta}{3}+\frac{4\sigma}{5}+\frac{6\delta}{7}) = C$$

$$\frac{d}{dz}p\left(\frac{8\beta^2}{15}+\frac{32\sigma^2}{45}+\frac{72\delta^2}{91}+\frac{128\beta\sigma}{105}+\frac{576\sigma\delta}{385}+\frac{80\delta\beta}{63}\right) = -\frac{1}{\gamma M_i^2}\frac{dp}{dz}-2\beta-4\sigma-6\sigma \tag{B.1.1}$$

Satisfying the momentum equation on the wall gives

$$\frac{dp}{dz} = -2\gamma M_i^2(\beta+6\sigma+15\delta) \tag{B.1.2}$$

Satisfying the momentum equation, instead, on the centerline of the channel gives

$$\frac{dp}{dz} = -\gamma M_i^2\left\{2\beta+\frac{1}{2}p\frac{d}{dz}(\beta+\sigma+\delta)^2\right\} \tag{B.1.3}$$

The equations for the fourth order velocity representation is got by setting $\delta = 0$. When using the fourth order velocity representation, a further choice is to be made about where the momentum equation is to be exactly satisfied — at the wall or on the centerline, corresponding to whether Eq. B.1.2 or Eq. B.1.3 is to be used.

B.2 Non-Isothermal Case

The integrated continuity and momenturm equations are

$$g(\frac{2\beta}{3}+\frac{4\sigma}{5}+\frac{6\delta}{7})=C$$

$$\frac{d}{dz}g\left(\frac{8\beta^2}{15}+\frac{32\sigma^2}{45}+\frac{72\delta^2}{91}+\frac{128\beta\sigma}{105}+\frac{576\sigma\delta}{385}+\frac{80\delta\beta}{63}\right)= -\frac{1}{\gamma M_i^2}\frac{dp}{dz}-\frac{2p}{gn}(\beta+2\sigma+3\sigma) \tag{B.2.1}$$

The other condition resulting from the transformation, which introduces g as a variable is

$$p=g\left\{n-m\left(\frac{8\beta^2}{15}+\frac{32\sigma^2}{45}+\frac{72\delta^2}{91}+\frac{128\beta\sigma}{105}+\frac{576\sigma\delta}{385}+\frac{80\delta\beta}{63}\right)\right\} \tag{B.2.2}$$

Satisfying the momentum equation on the wall gives

$$\frac{dp}{dz}=-2\gamma M_i^2\frac{p^2}{g^2n^2}(\beta+6\sigma+15\delta) \tag{B.2.3}$$

Doing the same on the centerline of the channel gives

$$\frac{p}{2(n-m(\beta+\sigma+\delta)^2)}\frac{d}{dz}(\beta+\sigma+\delta)^2=-\frac{1}{\gamma M_i^2}\frac{dp}{dz}-\frac{2\beta p^2}{(n-m(\beta+\sigma+\delta)^2)^2g^2} \tag{B.2.4}$$

Again the equations for the fourth order velocity representation are recovered by setting $\delta = 0$. Also, when using the fourth order velocity representation, a choice is to be made between satisfying the momentum equation on the wall, Eq. B.2.3, or on the centerline, Eq. B.2.4.